# CAAP Annual Report

**Date of Report**: 10*/02/2024*

**Prepared for**: *U.S. DOT Pipeline and Hazardous Materials Safety Administration*

**Annual Period:** **From** *(09, 28, 2023)* **to** *(09, 27, 2024)*

**Contract Number**: *693JK32250009CAAP*

**Project Title**: *All-in-One Multifunctional Cured-In-Place Structural Liner for Rehabilitating of Aging Cast Iron Pipelines*

**Prepared by**: Ying Huang

**Contact Info.:** *701-231-7651，ying.huang@ndsu.edu*

# Table of Contents

## Section A: Business and Activities

### (a) Contract Activities

- Contract Modifications: N/A.
- Educational Activities:

o Student and postdoc mentoring:

1. Postdoc Research Fellow:

   Xingyu Wang, Civil, Construction, and Environmental Engineering, North Dakota State University, 09/27/2023-present

2. Ph. D. Students:

   Tofatun Jannat, Department of Civil, Construction, and Environmental Engineering, North Dakota State University, Advisor: Ying Huang, 10/01/2022-present

   Gul Badin, Department of Civil, Construction, and Environmental Engineering, North Dakota State University, Advisor: Ying Huang, 10/01/2023-present

   Austin Knight, Ph. D. Student, Department of Mechanical Engineering, Advisor: Long Jiang, 01/01/2023-current

   Zahoor Hussain, Ph. D. Student, Department of Civil, Construction, and Environmental Engineering, Advisor: Zhibin Lin, 01/01/2023-current

   Yasir Mahmood, Ph. D. Student, Department of Civil, Construction, and Environmental Engineering, Advisor: Ying Huang, 01/01/2023-current

   Junyi Duan, Ph.D. Student, School of Construction Management Technology, Purdue University, Advisor: Chengcheng Tao, 10/01/2022-current

   Yizhou Lin, Ph.D. Student, School of Construction Management Technology, Purdue University, Advisor: Chengcheng Tao, 8/15/2023-current

   Huaixiao Yan, Ph.D. Student, School of Construction Management Technology, Purdue University, Advisor: Chengcheng Tao, 1/6/2024-current

   Madeleine C. Oliver, Hao Yuan, The University of Oklahoma, Advisor: Liangliang Huang, 10/01/2022-current

3. Masters Students:

   Muhammad Imran Khan, Department of Civil, Construction, and Environmental

Engineering, North Dakota State University, Advisor: Ying Huang, 01/01/2023-present

4. Undergraduate Students:

   Kathryn S. Quenette, Undergraduate Student, Department of Civil, Construction, and Environmental Engineering, Advisor: Ying Huang, 01/01/2023-current

   Benjamin Verwey, Undergraduate Student, Department of Mechanical Engineering, Advisor: Ying Huang, 01/01/2023-current

- Student internship:

- Educational activities:

(1) The PI, Dr. Y. Huang hosted a four-day Summer Kids STEM camp from July 22-25 2024 (Figure A-1). In this camp, 12 middle students attended the camp and had hands-on experiences related to pipelines.

Figure A-1 2024 NDSU Summer STEM Camp

(2) The Co-PI, Dr. C. Tao worked with Purdue K-12 Science Outreach programs on K-12 Superheroes of Science education videos related to sustainable and resilient infrastructure. Undergraduate students Gracyn Wyman, Andraya Fuller, Joy Gao and Ph.D. student Junyi Duan, Xiaoyue Zhang at Purdue University worked as volunteers in filming the videos (Figure A-2).

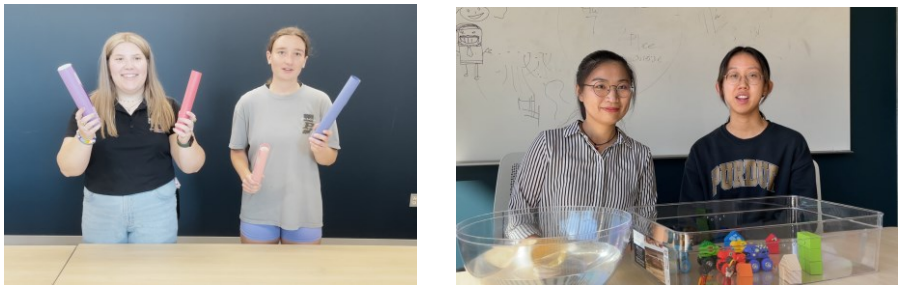

Figure A-2 2024 Purdue University Outreach Activity

(3) The Co-PI, Dr. L. Huang gave a short course “Principles and Hands-on

Tutorials of Molecular Simulation" at the Center for Space and Earth Science, Los Alamos National Laboratory, from September 25-29, 2023.

- Career employed:

Leonard Chia, 08/15/2023 employed by Intertek PSI.

- Others:

  - Dissemination of Project Outcomes:

(1) Duan, J., Tao, C., & Huang, Y. (2024). Computational Analysis of Repair and Rehabilitation of Aging Underground Cast-Iron Pipelines with Cure-In-Place-Pipe Liner. *Engineering Mechanics Institute Conference and Probabilistic Mechanics & Reliability Conference (EMI/PMC2024)*, Chicago, IL, May 28-31, 2024.

(2) Lin, Y., Duan, J., Tao, C., & Huang, Y. (2024). Effect of Fiber Configuration on Mechanical Behavior of Fiber-Epoxy Composites through Computational Analysis. *Engineering Mechanics Institute Conference and Probabilistic Mechanics & Reliability Conference (EMI/PMC2024)*, Chicago, IL, May 28-31, 2024.

(3) Duan, J., Tao, C., & Huang, Y. (2024). Pipeline integrity analysis through data-driven approaches. *ASCE Construction Institute (CI) and Construction Research Congress (CRC) Joint Conference 2024*, Des Moines, IA, March 20-23, 2024.

(4) Duan, J., Tao, C., & Huang, Y. (2024). Finite element analysis of structural lining materials for pipeline rehabilitation. *ASCE Construction Institute (CI) and Construction Research Congress (CRC) Joint Conference 2024*, Des Moines, IA, March 20-23, 2024.

(5) Zhang, X., Duan, J., Tao, C., & Huang, Y. (2023). Risk assessment models for pipeline infrastructure failure. *ASCE Infrastructure Innovation & Adaptation for a Sustainable & Resilient World (INSPIRE) Conference*, pp. 404-410, Arlington, VA, Nov 16-18, 2023.

(6) Duan, J., Tao, C., & Huang, Y. (2023). Computational modeling of cured-in-place structural liner for aged pipeline rehabilitation. *ASCE Infrastructure Innovation & Adaptation for a Sustainable & Resilient World (INSPIRE) Conference*, pp. 267-273, Arlington, VA, Nov 16-18, 2023.

(7) Huang, Y., Jiang, L., Lin, Z., Tao, C., Huang, L., Wang, X., Knight, A., Duan, J., & Lin, Y. (2023). All-in-One Multifunctional Cured-In-Place Structural Liner for Rehabilitating of Aging Cast Iron Pipelines, Pipeline Safety Research and Development Forum 2023, *Pipeline and Hazardous Materials Safety Administration (PHMSA)*, U.S. Department of Transportation, Arlington, VA, October 31-November 1, 2023.

(8) Zhang, X., Tao, C., & Huang, Y. (2023). Machine learning-based risk model for

pipeline integrity management. *ASCE International Conference on Computing in Civil Engineering*, Corvallis, pp. 689-696, Oregon, June 25-28, 2023.

(9) Duan, J., Tao, C., & Huang, Y. (2023). Numerical analysis of cured-in-place pipe structural liner for underground pipeline rehabilitation. *ASCE International Conference on Computing in Civil Engineering*, pp. 772-780, Corvallis, Oregon, June 25-28, 2023.

- Citations of The Publications:

1. Wang, X., Koirala, S., Xu, L., Li, Q., Lin, Z., Qi, X., ... & Wang, D. (2024). Insights in emerging Ti3C2Tx MXene-enriched polymeric coatings for metallic surface protection: Advancements in microstructure, anti-aging, and electrochemical performance. *Progress in Organic Coatings*, *194*, 108606.

2. Wang, X., Koirala, S., Xu, L., Li, Q., Wang, D., Qi, X., ... & Lin, Z. (2024). Advancements in emerging MXene-integrated nanocomposite coatings: Unraveling defect-free microstructure for superior tribological, mechanical, and anti-aging features. *Progress in Organic Coatings*, *188*, 108206.

3. D. Zhang, Y. Huang, W. Xia, L. Xu, and X. Wang, "Dispersion characteristics and mechanical properties of epoxy nanocomposites reinforced with carboxymethyl cellulose functionalized nanodiamond, carbon nanotube, and graphene", 45(1), 398-412, (2024).

4. Z. Hussain, Z. Lin, H. Pan, Y. Huang, F. Tang, and L. Jiang, "Synergizing empirical and AI methods to examine nano-silica's microscale contribution to epoxy coating corrosion resistance", Ceramics International, September 16, 2024.

5. L. Xu, S. Shi, F. Yan, and Y. Huang, "Corrosion Monitoring and Assessment of Steel under Impact Loads Using Discrete and Distributed Fiber Optic Sensors", Optics and Laser Technology, Vol. 174, 110553, 2024.

6. Y. Mohmood, J. Chen, N. Yodo, and Y. Huang, "Optimizing Natural Gas Pipeline Risk Assessment using Hybrid Fuzzy Bayesian Networks and Expert Elicitation for Effective Decision-Making Strategies," Gas Science and Engineering, 125, 205283, (2024).

7. Y. Mahmood, N. Yodo, Y. Huang, and E. Khan, "Enhancing Risk Assessment in Natural Gas Pipelines: A Fuzzy-Aggregation Approach Supported by Expert Elicitation", Practice Periodicals on Structural Design and Construction, 29(4), 1557, (2024).

8. Chang, Q., Huang, L., McKenzie, K., Carere, C., Stott, M., Nicol, A., & Dempsey, D. (2024). Influence of hydrogen sulfide on gas-water interface in underground hydrogen storage: A molecular dynamics study. Journal of Energy Storage, 97, 112766.

9. Oliver, M. C., Zheng, R., Huang, L., & Mehana, M. (2024). Molecular simulations of

hydrogen diffusion in underground porous media: Implications for storage under varying pressure, confinement, and surface chemistry conditions. International Journal of Hydrogen Energy, 65, 540-547.

10. Chang, Q., Dempsey, D., Zhang, L., Zhao, Y., & Huang, L. (2024). Molecular dynamics insights into gas-water interfacial tension: Optimizing hydrogen storage in subsurface conditions. International Journal of Hydrogen Energy, 64, 896-905.

11. Xu, L, Wang, X., Lin, Y., Tao, C., Huang, Y., & Zhang, D.* (2024) Experimental and Numerical Investigations of Carbon-Based Nanoparticle Reinforcement on Microstructure and Mechanical Properties of Modified Polymeric Coatings. *Chinese Journal of Polymer Science* [Under review]

12. Wang, X., Duan, J., Yang X., Xu, L., Khan, M., Tao, C., & Huang, Y.* (2024) A Digital Twin Integrated Smart-liner for Visualization Monitoring of Oil and Gas Pipeline Infrastructure. *Applied Energy* [Under review]

- Others: N/A.

**(b) Financial Summary**

- Federal Cost Activities:

o PI/Co-PIs/students involvement:

The PIs and student involvements and other expenditures of the project are detailed in Table B-1 below. The table is a summary of all the expected expenditure from September 30th 2023 to September 30th 2024. A total expenditure of Year (Yr) 2 is expected to around $299,741.43. The annual financial report till June 30th 2024 is also submitted in the reporting website and will be updated when the next financial report is available (around Oct 15th 2024). The actual final financial report may have a slight difference with the table below due to the gap between the report and the availability of next financial report.

Table B-1 Summary of Yr 2 spending

| *Institution* | *Category* | Amount ($) | Amount ($) | Subtotal ($) |
|---|---|---|---|---|
| *North Dakota State University* | *Personnel* | Salary ($) | Benefit ($) | |
| | *PI: Y Huang* | 0.00 | 0.00 | 0.00 |
| | *Co-PI: Z. Lin* | 11225.05 | 2324.41 | 13549.46 |
| | *Co-PI: L. Jiang* | 12457.32 | 2572.45 | 15029.77 |
| | *Postdoc: X. Wang* | 31496.97 | 21218.62 | 52715.59 |
| | *Graduate Students* | | | |
| | Tofatun Jannat | 8581.80 | 2.08 | 8583.88 |
| | Zahoor Hussain | 17600.00 | 8.50 | 17608.5 |
| | Gul Badin | 550.01 | 0.75 | 550.76 |
| | Austin Knight | 11049.97 | 356.43 | 11406.4 |

| | | | | |
|---|---|---|---|---|
| | Muhammad Khan | 11299.08 | 5.85 | 11304.93 |
| | Undergraduate Student | | | |
| | Kathryn S. Quenette | 195.00 | 0.00 | 195.00 |
| | Benjamin Verwey | 5014.50 | 254.11 | 5268.61 |
| | *Materials* | 13036.57 | 0.00 | 13036.57 |
| | *Operation fee* | 8353.00 | 0.00 | 8353.00 |
| | *Travel* | 2239.15 | 0.00 | 2239.15 |
| | *Consultant: RagulaTech* | 10574.28 | 0.00 | 10574.28 |
| | *Total Direct* | | | **170415.90** |
| | *Indirect* | | | 76687.20 |
| | *Subtotal* | | | **247103.10** |
| *Purdue University* | Co-PI: C. Tao | *8677.02* | *2603.11* | 11280.13 |
| | *Graduate Students* | *21487.47* | *0.00* | *21487.47* |
| | *Materials* | *0.00* | *0.00* | *0* |
| | *Travel* | *3661* | | *0* |
| | *Indirect* | | | *19870.73* |
| | *Subtotal* | | | ***52638.33*** |
| *University of Oklahoma* | Co-PI: L. Huang | *0.00* | *0.00* | *0.00* |
| | *Ph. D. Students* | *0.00* | *0.00* | *0.00* |
| | *Materials and Travel* | *0.00* | *0.00* | *0.00* |
| | *Indirect* | *0.00* | *0.00* | *0.00* |
| *Total* | | | | ***299741.43*** |

- Cost Share Activities:

o Cost share contribution:

Table B-2 below details the cost share in NDSU and Purdue during Yr 2 of the project. A total of $58,164.84 was provided as match fund in Yr 2. The actual final financial report may have a slight difference with the table below due to the gap between the report and the availability of next financial report.

Table B-2 Summary of Yr 2 cost share

| *Institution* | *Category* | *Amount ($)* |
|---|---|---|
| *North Dakota State University* | Graduate Tuition | |
| | Tofatun Jannat | 7614.65 |
| | Austin Knight | 7614.65 |
| | Zahoor Hussain | 7614.65 |
| | Muhammad Imran Khan | 7614.65 |
| | Indirect | 13706.37 |
| | Subtotal | 44165.01 |
| *Purdue University* | Faculty salary, and graduate salary and tuition from Purdue Office of Research - Executive | 13999.83 |

| | | |
|---|---|---|
| | Vice President for Research and Partnerships | |
| | Travel | 0 |
| | Subtotal | 13999.83 |
| *Total* | | 58164.84 |

## (c) Project Schedule Update

- Project Schedule:

According to the project schedule planned in the proposal, as shown in Table C-1 below, we are on schedule (X in the table indicates the portion of that task has been completed).

Table C-1 Project schedule and Yr 2 accomplishments

| Tasks (Milestones, Completion Date) | Year 1 | | | | Year 2 | | | | Year 3 | | | |
|---|---|---|---|---|---|---|---|---|---|---|---|---|
| | Q1 | Q2 | Q3 | Q4 | Q1 | Q2 | Q3 | Q4 | Q1 | Q2 | Q3 | Q4 |
| Task 1 (Milestone 1) (M.1: 01/10/2023) | X | | | | | | | | | | | |
| Task 2 (Milestone 2) (M.2: 10/10/2024) | X | X | X | X | X | X | X | X | | | | |
| Task 3 (Milestone 3) (M.3: 01/10/2025) | X | X | X | X | X | X | X | X | | | | |
| Task 4 (Milestone 4) (M.4: 04/10/2025) | | X | X | X | X | X | X | X | | | | |
| Task 5 (Milestone 5) (M.5: 07/10/2025) | | | X | X | X | X | X | X | | | | |
| Task 6 (Milestone 6) (M.6: 09/30/2025) | X | X | X | X | X | X | X | X | | | | |

- Corrective Actions: N/A

## (d) Status Update of the 8th Quarter Technical Activities

**CAAP Quarterly Report #8**

**[10/02/2024]**

*Project Name: "All-in-One Multifunctional Cured-In-Place Structural Liner for Rehabilitating of Aging Cast Iron Pipelines"*

*Contract Number: 693JK32250009CAAP*

*Prime University: North Dakota State University*

*Prepared By: [Ying Huang, ying.huang@ndsu.edu, 701-231-7651]*

*Reporting Period: [06/28/2024 – 09/27/2024]*

**Project Activities for Reporting Period:**

In the 7th quarterly report, Tasks 2.1, 2.2, 3.1, 3.3, 3.4, 4.1, 4.2, and 5.1 were carried out as proposed. In this quarter (Quarter 8), the research team has continued to make consistent progress on selected tasks, including Task 3.2. Summaries of the key activities completed during the 8th reporting period are provided below.

**Task 2.1** Preparation of Vitrimer Epoxy Resins, Characterization, and Optimization of the Processing and Curing Conditions (90%): In the last report, an excellent UV curing rate was found for the developed self-healing resin (formulation of DFMA: RDMA). The research team (Dr. Long Jiang and Austin Knight, Ph. D. student from NDSU) investigated self-healing polymers with various formulations, specifically targeting the glass transition temperature. The key findings are presented below:

(1) DMA Dilatometry of Self-Healing Formulations: To determine the important transition temperatures of the formulations developed last quarter and to confirm the new formulations had lower glass transition temperatures ($T_g$s), dilatometry tests were done using a TA Q800 DMA. Formulations containing the difunctional acrylate (DFA) and reactive diluent acrylate (RDA) had lower observed transition temperatures than their methacrylate alternatives (difunctional methacrylate (DFMA) and reactive diluent methacrylate (RDMA) (Figure D-1). To increase the visibility of the $T_v$ and increase the self-healing properties of the polymer, a catalyst will be added in future work. Dynamic dual cantilever tests will also be done using the DMA to confirm that the lower transition temperature is the $T_g$.

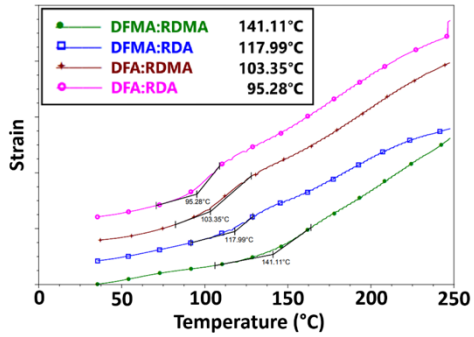


Figure D-1. Dilatometry results from the various self-healing polymer formulations.

*Note: Formulations containing the DFA and RDA had lower transition temperatures than DFMA and RDMA. This is expected because of the lack of methyl substitute in the acrylates resulting in a more flexible polymer backbone. The self-healing transition temperature, the topology freezing temperature ($T_v$), is visible as an increase in the strain rate above the $T_g$ in the formulations with lower $T_g$s but is not very pronounced.*

**Task 2.2** Investigating Self-healing and Mechanical Properties of Vitrimer Epoxy Resins (70%): The research team (Dr. L. Jiang, Dr. Y. Huang, and Austin Knight, Ph. D. student from NDSU) continued investigating self-healing polymers reinforced with nanodiamonds, focusing on their welding properties (Results combined in Task 3.2) and corrosion resistance. The key findings are presented below:

(1) Corrosion Resistance of Self-Healing Polymer with 0.5% ND: Self-healing polymer samples, both with and without 0.5% nanodiamond, were exposed to 500 hours in the B117 salt spray chamber. No evidence of corrosion was observed in any of the samples (Figure D-2 (c)). The EIS results aligned well with the visual observations (Figure D-2 (a)(b)); however, the 0.5% ND specimens demonstrated superior performance, with higher Zmod values compared to the neat polymer.

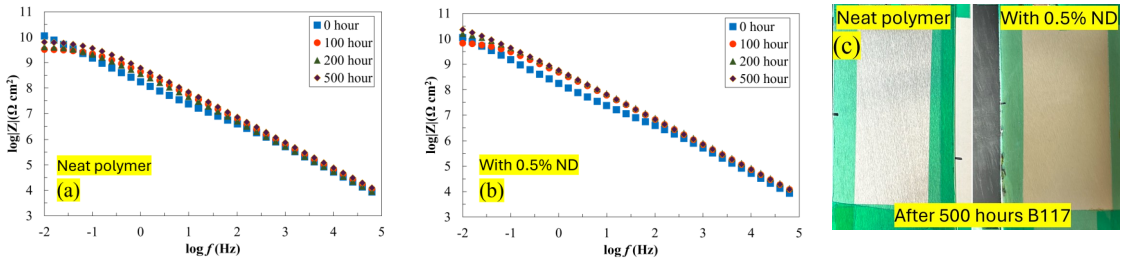


Figure D-2. (a)(b) EIS curves of self-healing polymer and 0.5% ND specimen after salt spray, and (c) a picture of a typical specimen.

**Task 3.1** High Mechanical Performance (85%) and **Task 3.2** Enhanced bonding performance (60%): During this reporting period, the research team (Dr. Ying Huang, Dr. Xingyu Wang, and Muhammad Imran Khan, Master student from NDSU) continued experimental study on nanoparticle reinforcement on the developed self-healing polymer (DFMA: RDMA). The key findings are provided below:

(1) Abrasion resistance of Self-Healing Polymer with 0.5% ND: Similar to other properties, the abrasion resistance was enhanced by the addition of 0.5% nanodiamonds (ND), as evidenced by the reduced mass loss after the abrasion test, as shown in Table D-1. Additionally, the surface roughness after abrasion was also reduced with the addition of ND, aligning well with the improved abrasion resistance results.

Table D-1. Abrasion resistance of self-healing polymer with 0.5% N

| Sample | Mass Loss (g) | Roughness after Abrasion (μm) |
|---|---|---|
| Neat self-healing polymer | 0.0245 | 1.258 |
| With 0.5% ND | 0.0207 | 1.183 |

(2) Long-Term Flexural Creep of Self-Healing Polymer with 0.5% ND: A long-term flexural creep test was started for the self-healing polymer with ND. Static were applied to each formulation, and the deflection was measured at intervals for a total test time of 1000 hrs. (Figure D-3). The test is currently ongoing, and the final results will not be obtained until the test is complete.

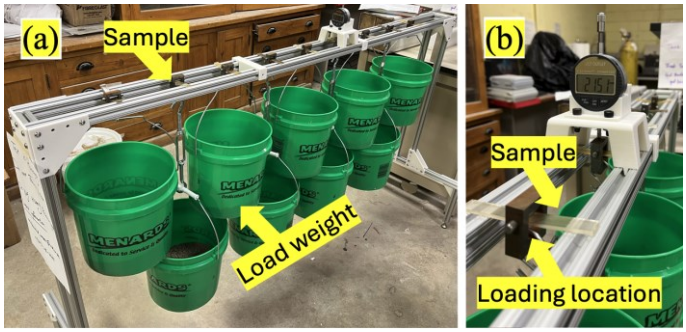


Figure D-3. The (a) long term flexural creep device and (b) the deflection of specimen being measured.

(3) Bonding Property of Self-Healing Polymer with 0.5% Nanodiamond (ND): Figure D-4 presents the results from the single-lap-shear test of the self-healing polymer with ND. The addition of 0.5% ND significantly increased the stress, strain, and toughness of the material. While the neat specimens did not exhibit plastic deformation, the specimens reinforced with 0.5% ND did.

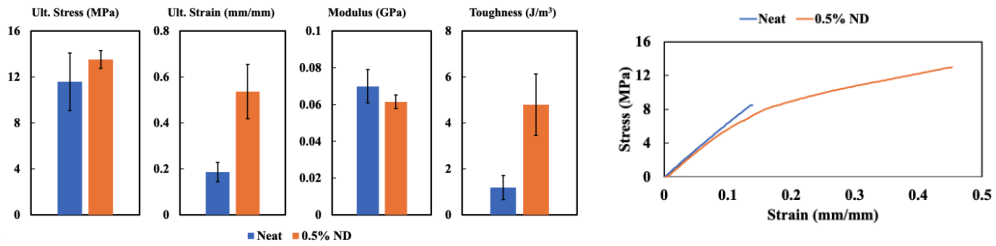


Figure D-4. Shear property of self-healing polymer with 0.5% ND.

**Task 3.3.** Reducing the Permeability and Investigating the Interfacial Bonding Chemical Analysis (70%): Previously, the research team (Dr. Liangliang Huang, Qiuhao Chang, Ph. D. student from University of Oklahoma) continued investigating the hydrogen diffusion process using developed nanopore models, with a focus on interfacial tension dynamics.; simultaneously, the development of vitrimer models is ongoing:

(1) Interfacial Tension Dynamics: Figure D-5(Left) illustrates the relationship between IFT and $H_2S$ concentration for binary systems of ($H_2S$+$H_2$)/$H_2O$ and ($H_2S$+$CH_4$)/$H_2O$. Our findings demonstrate a trend where IFT diminishes with escalating concentrations of $H_2S$. Results suggest that $H_2S$ exerts a more substantial influence on IFT when interacting with $H_2$ than $CH_4$ in an aqueous environment. It is also worth noting that the diminution of IFT becomes more pronounced as $H_2S$ concentration increases beyond the 10% threshold, indicative of a significant influence of $H_2S$ on the gas-water IFT across both binary systems studied. Yet, it is important to note that such an effect plateaus when the $H_2S$ concentration surpasses 80%, beyond which any further increase in $H_2S$ concentration yields minimal additional impact on IFT.

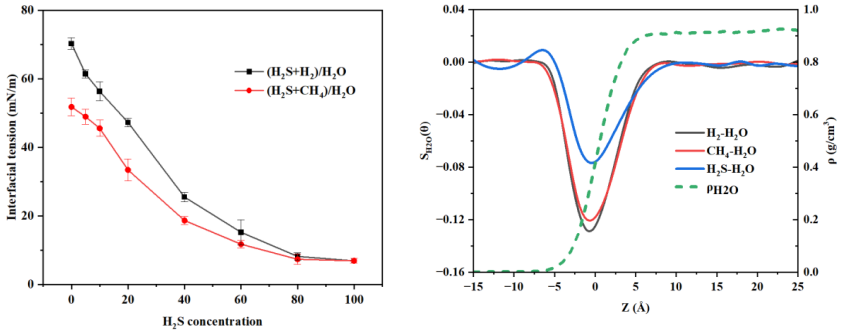


Figure D-5. (Left) IFTs at 14.5 MPa and 343 K as a function of $H_2S$ concentration for $(H_2S+H_2)/H_2O$ and $(H_2S+CH_4)/H_2O$ systems; (Right) Orientation profiles of $H_2O$ molecules along the Z direction in three binary gas-water systems.

(2) Reactive Vitrimer Model: As illustrated in Figure D-6, a reactive vitrimer model can be developed by enabling curing reactions, not based on force-field reaction modeling, but as a bonding procedure for atoms that mimics chemical reactions. This model considers the dynamic S-S bond exchange process of AFD. The dynamic exchange of disulfide bonds was modeled as a two-step reaction, with pre- and post-reaction templates constructed along with a reaction map. This approach effectively describes the dynamic nature of the covalent networks in the vitrimer model.

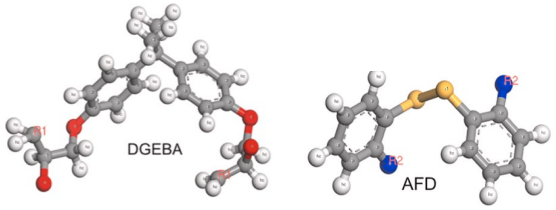


Figure D-6. Reactive sites of DGEBA and AFD monomers for a reactive vitimite model.

*Note: Bond exchange reactions were enabled when sulfur atoms from different chains came within a cutoff distance of 4.12 Å, with the reaction probability modeled as a function of temperature.*

**Task 3.4** Finite Element Numerical Analysis to Guide the Design of the Developed High-performance Healable CIPP Structural Liner (80%): During this reporting period, the research team (Dr. Chengcheng Tao, Junyi Duan, Ph.D. student from Purdue University) conducted finite element analysis (FEA) on pipelines with CIPP liners to investigate the interfacial relative displacement and stress fields between layers, assessing the bonding performance of the pipe-liner system. Additionally, studied the effects of nano-reinforcement in the epoxy system. The results are summarized below:

(1) Structural Buckling Analysis of CIPP Liner: The structural buckling was significantly affected by interfacial debonding between liner and pipe. In this study, we investigated the interfacial relative displacement and stress fields between the layers to analyze the bonding performance of the pipe-liner system. A three-dimensional (3D) finite element model is developed for the three-layer pipe-liner system, consisting of damaged host pipe, adhesive layer, and CIPP liner. There are two interfacial contact pairs in this study, the – adhesive layer interface and the adhesive layer–CIPP liner interface. Figure 7(a)(b) shows the radial displacement and interfacial shear stress fields, demonstrating the bonding performance between the pipe and adhesive layer. While the adhesive layer and CIPP liner deform integrally, high shear stress is detected around the corrosion hole area between the pipe and

adhesive layer. We generated a dataset by exporting the nodal stress and displacement results of three layers at the hole area, shown in Figure D-7(c). The dataset will be used to train the machine learning algorithms for risk assessment in Task 5.1.

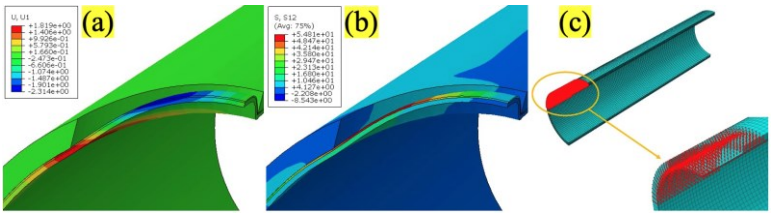


Figure D-7. Radial displacement (a) and shear stress (b) results on pipe-liner system. (c)The locations of nodes exporting stress and displacement field results.

- 

(2) Developed RVE Model of Nano-reinforced Epoxy System: We also created Representative Volume Element (RVE) model in finite element analysis (FEA) for nano-reinforced epoxy system. The RVE analyses of nanofiber-reinforced epoxy are conducted from 0% to 2% weight fraction respectively. The model of the RVE with aligned and oriented GNPs is illustrated in Figure D-8. This model showcases the arrangement and distribution of GNPs within the matrix.

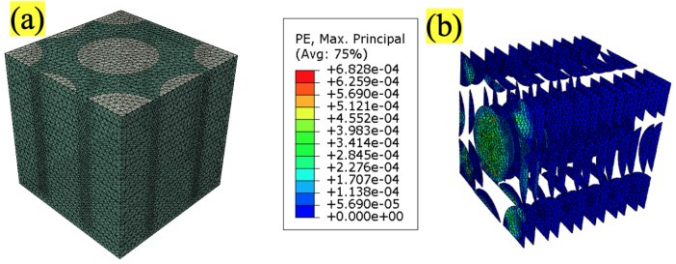


Figure D-8. A representative example of an RVE with aligned 2.0% GNPs. (a) the RVE with the meshing geometry, and (b) distribution of GNPs.

*Note: There are three types of nanoparticles in this study: 1) 0D nanodiamonds (ND), 2) 1D multiwall carbon nanotubes (MWNT), and 3) 2D graphene nanoplatelets (GNP).*

(3) Mechanical Properties of Nano-reinforced Epoxy System: The stress-strain results from various RVE models are analyzed to understand the impact of different weight fractions of additives on the ultimate stress of composites, as shown in Figure D-9. For the ND additive in Figure D-9(a), varying weight fractions from 0.5% to 2.0% showed minimal impact on the plastic region and ultimate strength, with a slight increase at 2.0% ND. A similar trend in Figure D-9(b) is observed in the 90° orientation for MWNT composites, where varying weight percentages (0.5%, 1%, and 2%) indicate that the material's strength remains unchanged in the 0° loading direction, demonstrating non-isostrain conditions. For GNP composites, under axial loading, the stress remains consistent with increasing GNP weight fractions, while radial simulations show enhanced ultimate stress with increasing weight

fractions, illustrated in Figure D-9(c). Further analysis of ultimate strength outcomes for each type of nanoparticle in Figure D-9(d) to (f). These findings highlight the significant impact of nanoparticle geometry and orientation on the mechanical properties of composite materials.

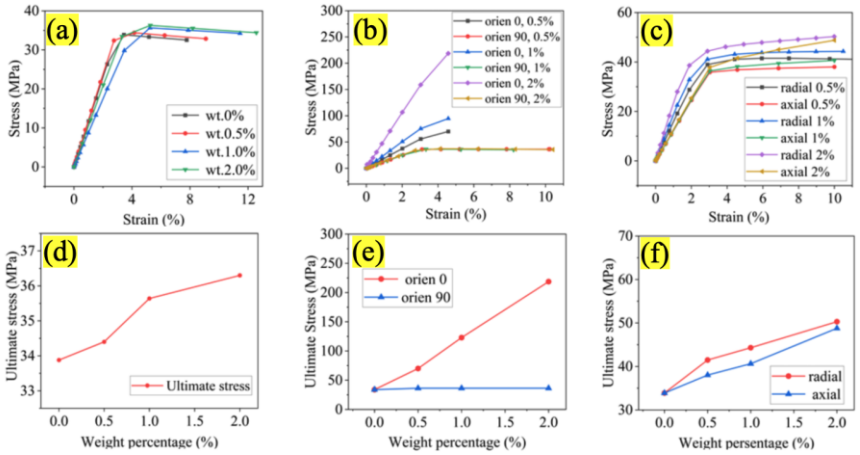


Figure D-9. The stress-strain curve predicted by the simulations under uniaxial tensile loading (a) ND (b) CNT, and (c) GNP. The ultimate strength of composite with different weight fractions, composite reinforced by (d) ND (e) CNT, and (f) GNP.

**Task 4.1** Development of Embedded Distributed Fiber Optic Sensors for Self-sensing Structural Liner (75%), and **Task 4.2** Investigating the Load Transfer between Layers of the CIPP Liner and the Cast-iron Substrate (60%): During this reporting period, the research team (Dr. Ying Huang and Dr. Xingyu Wang) continued the study on the smart-liner system, focusing on identifying internal damages and vulnerable areas during buckling deformation. The key findings are summarized below:

(1) Localization of Internal Damages: A novel aspect of this research is using sharp peak strain distributions in sensor signals to track damage within the specimen. Figure D-10 (a) presents results from sensor path-10 as a representative case, displaying strain signals collected under varying mechanical deformations. The peaks along the strain distribution curve pinpoint the locations of potential defects within the liner. The increasing magnitude of these peaks as deformation intensifies indicates defects were progressively worsening. This correlation suggests that the impact of deformation becomes more pronounced at higher strain levels, with the expanding defect areas. To confirm that the areas showing sharp peak strain correspond to defects in the liner system, micro-CT images were taken following the experiment. Figure D-11 provides a cross-sectional view of the liner system, illustrating the interface between the liner surface and the adhesive layer.

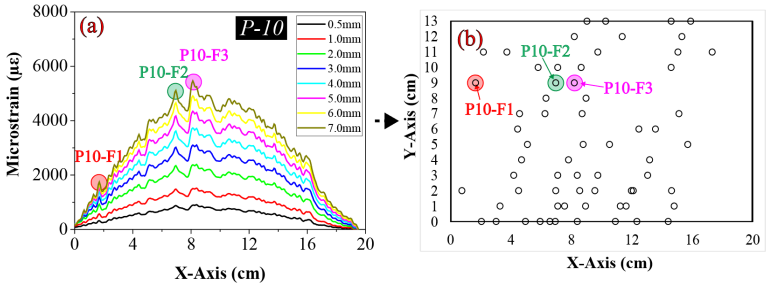


Figure D-10. (a) Strain distributions measured from path 10 (P-10), and (b) Map of failures in specimen.

*Note: The peaks are categorized by a unique identifier, in the path 10, they are denoted as P10-F1, P10-F2, and P10-F3.*

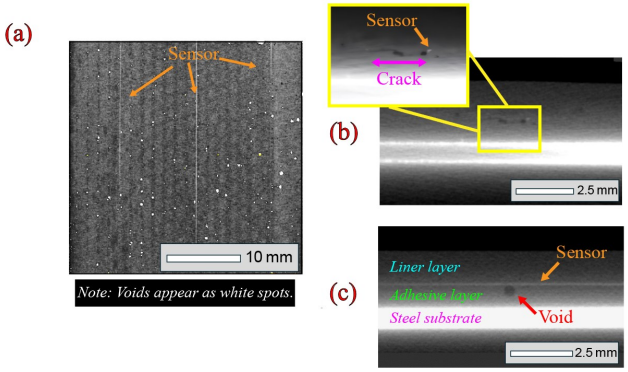


Figure D-11. Micro-CT cross-sectional images of the (a) topography of the liner system, location of (b) crack, and (c) voids detected by distributed sensor.

*Note: The white lines are the deployed distributed sensors. In Figure 11 (b), a developed crack was found; and it was detected by the sensor with a sharp peak in the strain signals.*

(2) Identifying High-Risk Areas for Damage Formation: Curing-induced strain serves as an indicator for regions within liner systems that are at an increased risk of crack formation, debonding, and delamination-related failures. Figure D-12 illustrates the relationship between curing-induced strain and the location of defects. It is evident that areas showing negative strain after curing are directly linked to defect formation. These zones, marked by concentrated curing-induced internal stresses—reflected by sharp peaks in the strain signals—exhibit weakened mechanical properties.

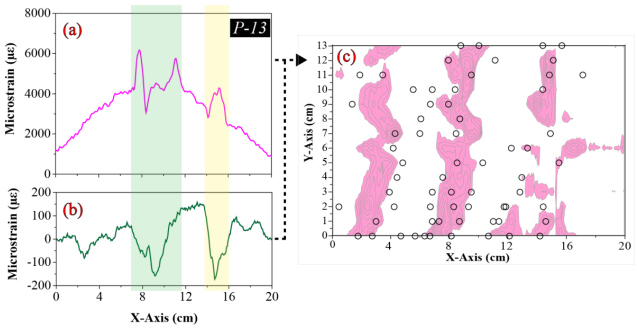


Figure D-12. Sensor signals in path 13 are highlighted in (a) the defected area after deformation, and (b) the corresponding curing strain. (c) 2-D plots indicating high-risk areas for damage formation.

*Note: the circles are the indentfied interal damages and pink area are areas exhibiting negative strain after the curing process.*

**Task 5.1** Development of CIPP Liner Risk Index for the Pipeline Integrity Management Enhanced by AI Algorithms (60%): During this period, the research team (Dr. Chengcheng Tao, Huaixiao

Yan, Ph.D. student from Purdue University) have conducted the risk assessment using dataset generated from finite element analysis for pipeline integrity management, with the results outlined below:

(1) Bonding Risk and Material Failure Risk Assessment: To predict the risk level for the CIPP liner in a damaged pipe. We consider two potential risks for a pipe-line system: debonding risk and material failure risk. For the debonding risk, we compare the shear stress with the adhesion strength. For material failure, we compare the maximum principal stress with the tensile strength. The basic idea for measuring the risk level is to compare the predicted stress with the corresponding strength and normalize their differences into 0 and 1. We train a machine learning-based risk model with the FEA data using the material properties from the experiment. Random forest algorithms are used for stress prediction. Table D-2 summarizes the results from FEA and ML; it indicates that the potential risks are debonding and failure of the adhesive layer.

Table D-2. Comparison between stress and material strength.

| Potential risks | Maximum stress (MPa) | | Strength (MPa) |
|---|---|---|---|
| | FEA simulation (MPa) | ML prediction (MPa) | |
| Debonding | 17.24 | 17.10 | 8.32 |
| Failure in adhesive layer | 49.91 | 49.62 | 34.15 |
| Failure of the liner | 25.16 | 25.78 | 99.68 |

(2) Risk Map Predicted by Machine Learning Algorithms: Figures D-13(a) and (b) demonstrate the risk map predicted by machine learning algorithms using the stress data on the bonding surface and adhesive layer material. For the stress risk map, we define the risk criteria by choosing the adhesion strength between epoxy and cast iron as 8.32 MPa.

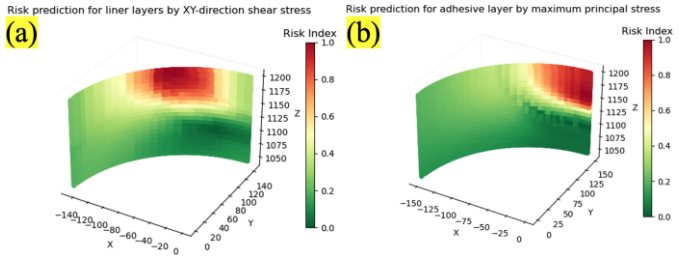


Figure D-13. (a) Debonding risk prediction; (b) Material failure risk prediction for the adhesive layer.

*Note: Green area indicates the safe area, the yellow area indicates the critical area, and the red area indicates the high-risk area.*

- The corrosion hole is at the upper right corner of the liner, while the risk area is at the edge of the hole based on the stress distribution information. Figure D-13(b) shows the material failure risk map. The yellow color represents 34.15 MPa which is the threshold for defining the risk of the adhesive layer material. Highest risk area occurs at the upper right of the adhesive layer, which aligns with the location of the corrosion hole.

**Project Financial Activities Incurred during the Reporting Period:**

The cost breakdown during the reporting period according to the budget proposal is shown in Table D-3.

Table 3. Cost breakdown

| Category | Amount spent during Q8 |
|---|---|
| **Personnel** | |
| Faculty | $0 |
| Postdoc | $25,286.71 |
| Students (RA and UR) | $18,100.56 |
| Benefits | $9,816.07 |
| **Operating Expenses** | |
| Travel | $0 |
| Materials and Supplies | $4,883.69 |
| Recharge Center Fee | $3,533.50 |
| Consultant Fee | $5,935.28 |
| **Subcontracts** | $20,289.95 |
| **Indirect Costs** | $30,400.14 |

**Project Activities with Cost Share Partners:**

The Match fund from NDSU for this project is coming from the tuition of the associated graduate students during their work on this project. During the reporting period (Q8), Zahoor Hussain (100%), Muhammad Imran Khan (100%), Austin Knight (100%), and Tofatun Jannet (100%) were hired on the project. The tuition for the four students during Q6 was estimated to be $12,520 at a rate of $463.73 per credit.

**Project Activities with External Partners:**

During this reporting period, George Ragula, our industry consultant, attended all the bi-weekly meetings with the research team.

**Potential Project Risks:**

No potential risks were noticed during this reporting period.

**Future Project Work:**

The research team will continue working on Tasks 2.1, 2.2, 3.1, 3.2, 3.3, 3.4, 4.1, 4.2 and 5.1.

**Potential Impacts on Pipeline Safety:**

The self-healing epoxy (DFMA: RDMA) reinforced with nanodiamonds (ND) demonstrated significant improvements in mechanical properties, corrosion resistance, welding capabilities, and abrasion resistance. Molecular dynamics simulations were used to analyze interfacial tension dynamics between residual water and gas, as well as to create a self-healing polymer model. Finite element analysis (FEA) provided insights into failure mechanisms within the liner system and was integrated with machine learning-based risk analysis. The smart-liner system is highly effective at identifying damage formation and predicting potential defect zones. All the findings provide valuable insights that help enhance performance and prevent failures during the design and manufacturing phases of CIPP liner systems.

# Section B: Detailed Technical Results in the Report Period

## 1. Background and Objectives in the 2nd Annual Report Period

### 1.1. Background

The following sections provide the background of each task, summarizing the accomplishments from the previous annual report. The current study builds upon these findings and advances the research accordingly:

(Task 2) Development of Self-Healing Polymer Resin:

For the adhesive layer in CIPP liners, UV-curable vitrimers and methacrylic reactive diluent (MRD) were selected for further study. The mechanical properties of the resin with varying diluent and catalyst content will be investigated to refine the self-healing resin formulation. This report will also quantify self-healing tests to enable comparison between formulations.

(Task 3) Nanoparticle Reinforcement in the Adhesive Layer:

Researchers explored different nanoparticles, including zero-dimensional (C60), one-dimensional (CNT), and two-dimensional (GNP) materials, with varying concentrations in commercially available epoxy. Comprehensive characterization and performance evaluation were conducted to identify the most suitable nanoparticles for future incorporation into the self-healing polymer.

(Task 3) Finite Element Numerical Simulation:

The research team developed a model for pipelines with liner systems, simulating subgrade loading to evaluate the effects of buried depth, CIPP liner thickness, and internal in-pipe pressure on cast-iron pipe performance. The results offer valuable insights into the effectiveness of CFRP liner rehabilitation for aged pipelines, examining the influence of in-pipe pressure, liner thickness, and stress concentrations.

(Task 3) Molecular Dynamic Simulation:

Last year's report focused on evaluating hydrogen models and their performance in molecular dynamics simulations. The study assessed various hydrogen models to understand hydrogen behavior in polymer materials, particularly self-healing epoxy resin. Hydrogen diffusion in nanopores (kaolinite and graphene) was also investigated, revealing faster diffusion in graphene pores due to surface roughness.

(Task 4) Smart Liner with Distributed Sensors:

Distributed fiber optic sensors were successfully embedded into the CIPP liner to monitor internal strain during the curing process. These sensors provided real-time data acquisition, capturing dynamic strain changes and offering valuable insights into the curing behavior of the liner system.

(Task 5) Risk Analysis:

Several machine learning models were tested to identify the most effective for CIPP liner systems. Eight factors were considered, including facility, leak detection, age, pipe

diameter, and land use. The results indicated that MVLR, GPR, and SVM are reliable algorithms for pipeline risk evaluation.

The tasks in this project are closely interconnected, with each contributing to the overall research objectives. For example, the development of self-healing polymers (Task 2.1) is incorporated with molecular dynamics simulations (Task 3.4), which provide insights into material behavior at the molecular level. Nanoparticle reinforcement (Task 3.1 and 3.2) studies are also conducted in conjunction with the self-healing polymer (Task 2.2), allowing for a comprehensive evaluation of the material's enhanced properties. In addition, molecular dynamics simulations are employed to model the interaction of gases with liner materials, offering a deeper understanding of the materials' performance in real-world conditions. Furthermore, finite element analysis (Task 3.4) plays a critical role in generating data that is subsequently utilized in machine learning models for risk analysis (Task 5.1), providing a robust framework for predicting and mitigating potential failures in the system. This multidisciplinary approach ensures a thorough investigation of the all-in-one high-performance liner system in pipelines.

### 1.2. Objectives in the 2nd Annual Report Period

The overall task is to integrate all findings from the various tasks to develop an all-in-one CIPP liner with self-healing and self-monitoring capabilities, enhanced mechanical strength, and improved durability. Additionally, simulations combined with AI-driven risk analysis will provide guidelines for CIPP liner performance in service. As the tasks run in parallel, the objectives for each area are summarized below.

Self-Healing Polymer Resin Development: The goal of this task is to develop an optimal self-healing polymer formulation for use as an adhesive layer in the CIPP liner. The formulation should demonstrate superior performance, high curing rates under UV light, compatibility with nanoparticles, and the ability to achieve self-healing after damage.

Nanoparticle Reinforcement in the Adhesive Layer: This task works closely with the development of self-healing polymers in Task 2. The focus is on incorporating nanoparticles into the adhesive layer to enhance performance. The selection of nanoparticles will be adjusted to align with the capabilities of next-generation self-healing polymers, ensuring improved mechanical and self-healing properties.

Molecular Dynamics Simulation: This task aims to simulate hydrogen behavior in various systems and materials, with a focus on vitrimer polymerization dynamics. Both non-reactive and reactive vitrimer models are being explored to understand polymerization reactions and hydrogen adsorption, providing critical insights into how these materials function under different conditions.

Finite Element Analysis (FEA): This task involves computationally analyzing the performance of epoxy and liner materials under different loading conditions. Case studies include rehabilitated cast-iron pipes with varying liner thicknesses, burial depths, and internal pressures. The parametric study results will guide the optimization of CIPP liner design and trenchless construction methods for pipeline infrastructure.

Incorporation of Distributed Sensors into CIPP Liner (Smart Liner): The objective here is to integrate distributed sensors into the CIPP liner to enable real-time monitoring of strain and structural integrity, creating a smart liner capable of self-monitoring during service.

AI-Driven Risk Analysis: By gathering data from experiments and FEA simulations, the machine

learning model for risk analysis will keep developing to provide more accurate predictions for pipeline performance.

## 2. Experimental Program in the 2nd Annual Report Period

### 2.1. Experimental Design

The experimental study strategy remains consistent with the approach outlined in the previous annual report.

### 2.2. Test Procedure

- Laboratory Testing:

The characterization and performance methods discussed in last year's report, including nanoparticle dispersion procedures, sample preparation, mechanical properties testing, and long-term testing, will not be repeated in this annual report.

- Field Testing: N/A

## 3. Results and Discussions

### 3.1. Task 2: Development of Healable and Sustainable CIPP Structural Liner

#### 3.1.1. (Task 2.1) Preparation of Vitrimer Epoxy Resins, Characterization, and Optimization of the Processing and Curing Conditions

The development during this reporting period is divided into three phases. First, the synthesis of the self-healing polymer was carried out using different resin and MRD ratios (1:0, 1:0.5, 1:1, 1:3, and 0:1), and the performance of each formulation was characterized. The optimal formulation, Resin-to-MRD ratio of 1:1, was selected due to its superior performance compared to other combinations. Second, the optimal formulation, 1:1, was combined with 0.5% nanodiamond, which was determined to provide the best reinforcement in the polymer, and its overall performance was evaluated. In parallel, the research team worked on reducing the temperature required for the resin to heal by modifying the 1:1 formulation.

It is worth noting that the development of the self-healing polymer, in conjunction with nanoparticle incorporation, involves extensive performance evaluations, and some studies in this section are also part of Task 3.

*3.1.1.1. Synthesis and Curing Characteristics (Resin-to-MRD ratios of 1:0, 1:0.5, 1:1, 1:3, and 0:1):*

In the previous study, the self-healing UV-curable resin is first synthesized in a synthesis step after which it can be cured using UV light. The non-functional catalyst (NFC) used in the last quarter was successful enough in preventing the gelling of the resin that the synthesis time was increased from 20 minutes to 5 hours at 90°C to ensure the complete conversion. During preliminary tensile testing, the longer synthesis time led to a decrease in the tensile properties. This was due to the sharp increase in viscosity with higher conversions inhibiting polymerization during the UV-curing step. A reactive diluent to prevent the high viscosity-induced polymerization inhibition is then necessary.

*a) Tensile Properties of Self-Healing UV-curable Adhesive:*

Therefore, a reactive diluent to prevent the high viscosity-induced polymerization inhibition was

added; formulations of the synthesized resin and MRD with ratios 1:0, 1:0.5, 1:1, 1:3, and 0:1 were prepared, and the tensile properties were tested. Further tensile testing was done with varying amounts of methacrylate reactive diluent (MRD) to determine the concentration that led to the most desirable properties. As shown in Figure 1, the 1:1 formulation showed the best tensile properties, workability, and dimensional stability. The properties of the synthesized resin increased with increasing reactive diluent content; however, the 1:3 and 0:1 formulations had extreme warpage and shrinkage, respectively.

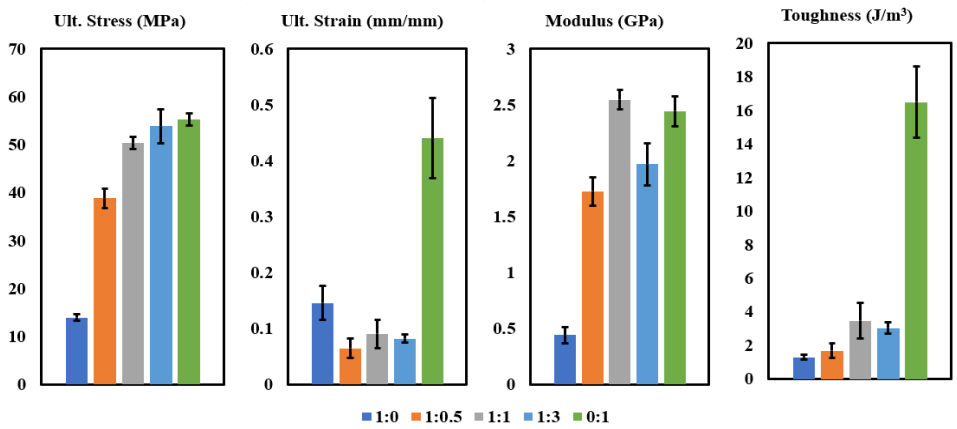


Figure 1. A summary of the tensile properties of synthesized formulations with various resin and reactive diluent ratio.

*b) Self-Healing of UV-Curable Adhesive:*

Formulations were applied to steel substrates with an 80-mil wire wound applicator rod to ensure even thickness between formulations and cut with a fresh razor blade through the entire thickness of the coating to ensure uniform cut profile. The cut profile and depth were measured using a KEYENCE microscope before and after healing by heating the coatings using a hot press for 10 minutes at 120°C and 50 lbs. The 1:0 and 0:1 formulations could not be cured into thin films on the substrate. The 1:0 formulation was too viscous and the 0:1 formulation was not viscous enough and spread too thin to cure so only the 1:0.5, 1:1, and 1:3 formulations were investigated.

The repair ratio of each formulation was calculated by measuring the depth of the cut before and after healing (Figure 2). As expected, the formulation with a greater amount of reactive diluent showed better self-healing performance. Profile images of the cuts before and after healing were taken to confirm the depth values measured (Figures 3, 4, & 5). The 1:1 formulation remains the best formulation as the 1:3 formulation has warping issues when UV-curing.

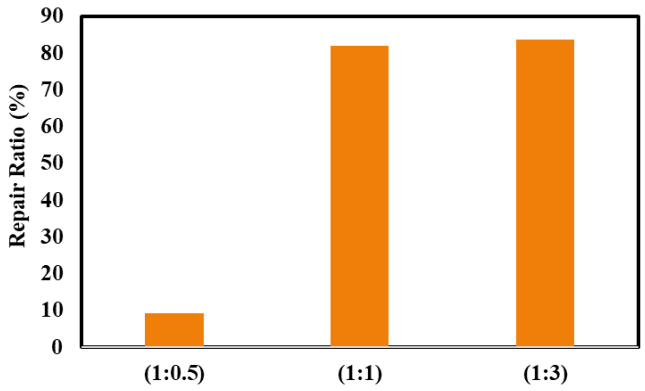


Figure 2. Repair ratios of the self-healing coatings.

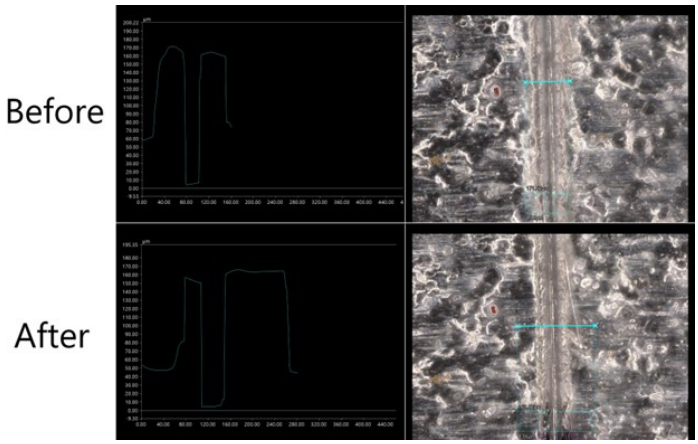


Figure 3. Profile images of before and after healing the 0:0.5 formulation.

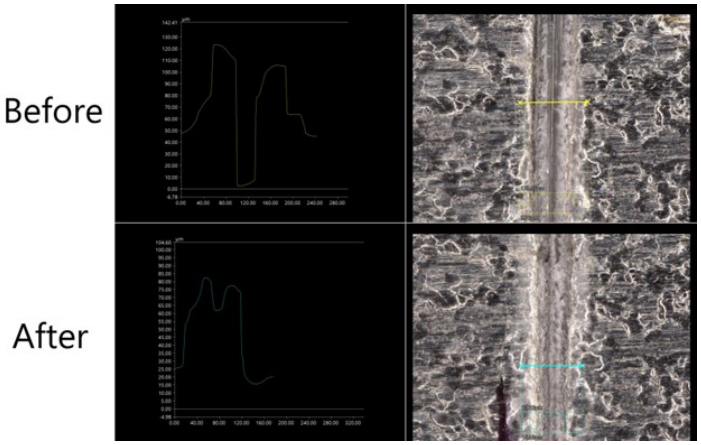


Figure 4. Profile images of before and after healing the 0:0.5 formulation.

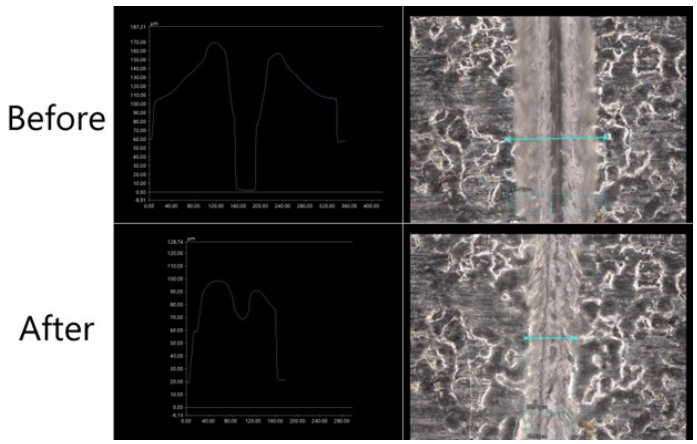


Figure 5. Profile images of before and after healing the 0:0.5 formulation.

*3.1.1.2. Formulation Selection for Follow-Up Study (Resin-to-MRD ratios of 1:1):*

The 1:1 formulation of the self-healing resin demonstrated the best overall properties in preliminary testing and was therefore selected by the research team for further, more detailed investigation. The follow-up study on this polymer is structured into three main phases. The first phase focused on evaluating the rate of UV curing through a commercial liner, which is critical for ensuring efficient and effective polymerization in practical applications. The second phase explored the introduction of a new photoinitiator to optimize the curing process, aiming to enhance the polymer's performance under various conditions. Finally, the third phase investigated the integration of nanoparticles into the self-healing polymer, aiming to improve its mechanical properties, durability, and self-healing capabilities. The key findings from these comprehensive studies are outlined below.

*a) Influence of Liner on UV Curing Process (Resin-to-MRD ratios of 1:1):*

The curing rate of the optimal formulation, 1:1, was determined with and without the presence of the cure-in-place liner. Hardness measurements were conducted using a Shore D Durometer at various durations of UV curing. Subsequently, resin was dispensed into a silicon tensile test mold, with the cut liner placed on top. Results initially showed a slightly lower curing rate; however, hardness eventually reached levels comparable to samples without the liner (neat), suggesting that the liner minimally hinders adhesive curing once the duration exceeds 10 minutes, as shown in Figure 6 (c).

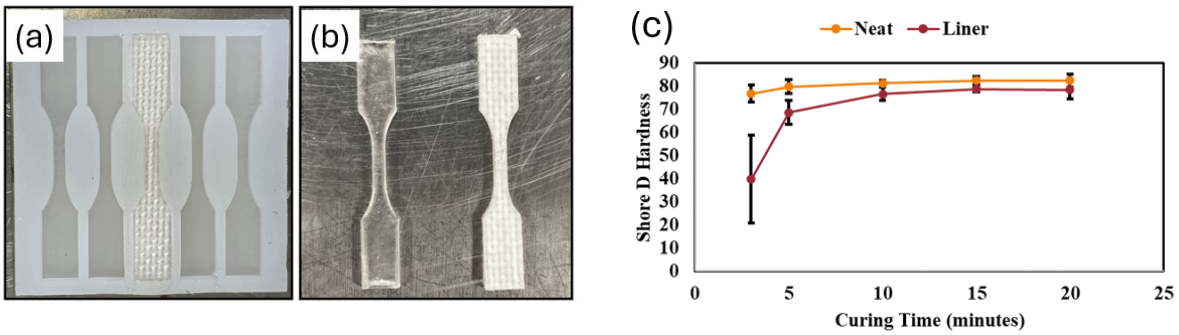

Figure 6. (a) (b) The resin in the silicon mold and the cut liner, and (c) hardness of the neat and liner covered sample after UV-curing.

*b) Nanoparticle Resin UV-Curing Rate Through Liner (Resin-to-MRD ratios of 1:1):*

Neat UV-curable self-healing resin and resin containing 0.1% nanodiamonds (ND) was cured on its own and through the CIP liner. The hardness increased over the course of 20 minutes of curing. The presence of the liner and nanoparticles dispersed in the resin both increased the time required to fully cure the resin due to UV-absorption (Figure 7).

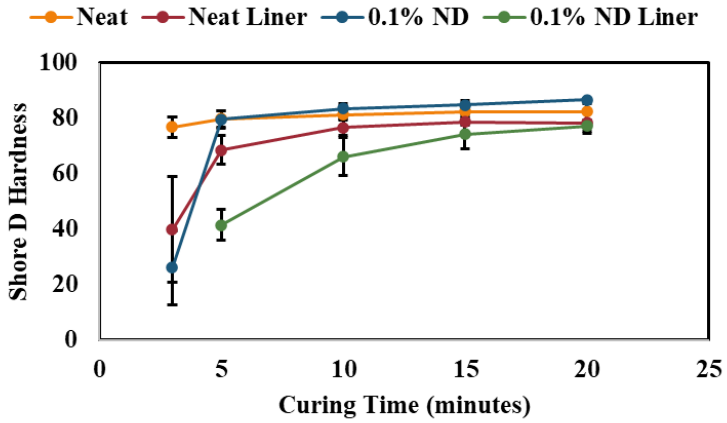


Figure 7. The Shore D Hardness of neat and 0.1% ND resin through a CIP liner.

*3.1.1.2. Increasing Curing Rate by Changing Photoinitiator in the Selected Formation (Resin-to-MRD ratios of 1:1):*

It has been observed that the addition of nanoparticles can significantly affect the curing rate, particularly when nanoparticles with a large surface area are used, as they have the potential to block more UV light. This can lead to slower curing times and reduced curing depth. To address this issue and improve both the curing rate and depth in nanoparticle-infused resins, the research team replaced the original photoinitiator (PI) with a more reactive one that decomposes at a higher UV-light wavelength. The new PI demonstrated remarkable improvements, curing the neat resin in less than 10 seconds and achieving a higher hardness than the old PI, which took 15 minutes to reach a lower hardness.

The curing depth of the resin is a critical factor that determines the maximum thickness of adhesive that can be effectively cured in a CIPP system. Achieving sufficient curing depth is essential to ensure the resin fully solidifies and maintains its mechanical properties, especially in applications where thicker adhesive layers are required. To evaluate this, resins containing different types and concentrations of nanoparticles were pipetted into an opaque mold with a depth of 4 mm, which represents the maximum curing depth achievable in these tests (Results of the healing test of these samples can be found in section 3.2.2.1.).

It was observed that the opacity of the resin, influenced by the presence of nanoparticles, directly impacted the curing depth. The more opaque the resin became, the shallower the curing depth, and a longer curing time was required to achieve full polymerization (Figure 8). This relationship is

important because nanoparticle-infused resins while enhancing mechanical properties, may require adjustments in curing methods or photoinitiator selection to overcome these limitations and achieve optimal performance.

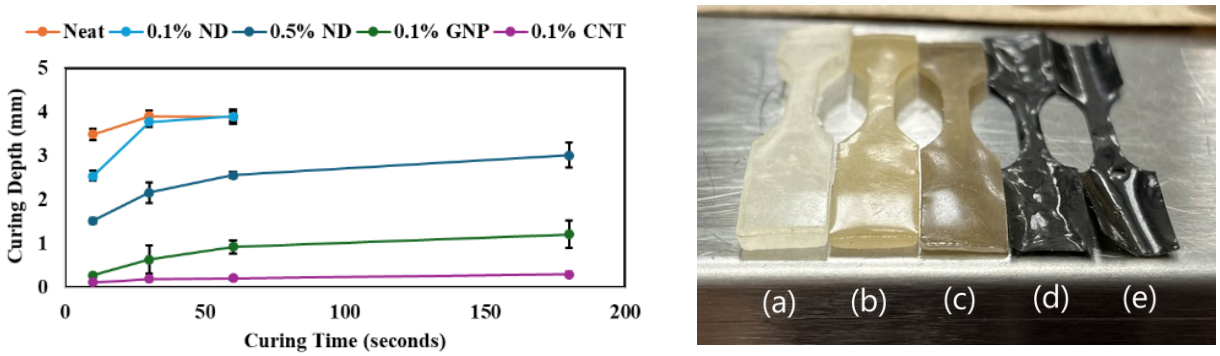


Figure 8. The (left) curing thickness of various formulations and (right) the (a) neat, (b) 0.1% ND, (c) 0.5% ND, (d) 0.1% GNP, and (e) 0.1% CNT formulations after being UV-cured for 10 seconds.

Therefore, from the curing rate part, the 0.5% ND showed minimal influence; furthermore, the new PI significantly improved the curing performance in ND-containing resins. For instance, the 0.5% nanodiamond (ND) resin cured within 30 seconds using the new PI, whereas the old PI required 15 minutes and only resulted in a partial cure with a depth of 1.5–2 mm (as shown in Figure 9). This advancement is crucial for ensuring that resins with nanoparticles achieve the necessary mechanical and structural properties in a shorter time frame, which enhances their practical applicability. The detailed results are presented below. Therefore, the majority of the work in Task 3 is focused on this new formulation, both with and without the addition of 0.5% nanodiamonds (ND).

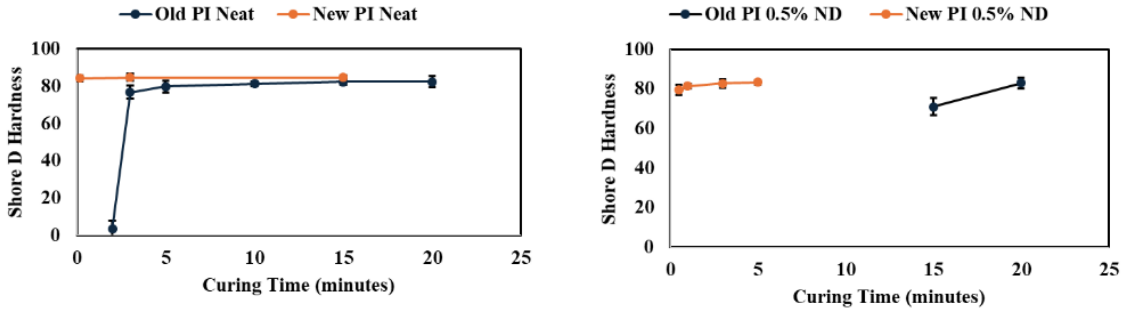


Figure 9. The curing rate of (left) the neat and (right) the 0.5% ND formulations.

*3.1.1.3. Approach to Lowering the Healing Temperature of the Resin:*

In trimer system two important temperatures to consider are the glass transition temperature (Tg) and the topology freezing temperature (Tv). The polymer must be heated above both of these temperatures for considerable healing behavior to occur. The next step in improving the healing properties of the trimer resin is to lower the Tg by incorporating different monomers into the base

formulation.

investigated the self-healing polymer with various formulations to lower the required temperature for the resin to heal, which is glass transition temperatures.

*a) DMA Dilatometry of Self-Healing Formulations:*

To determine the important transition temperatures of the formulations developed last quarter and to confirm the new formulations had lower glass transition temperatures ($T_g$s), dilatometry tests were done using a TA Q800 DMA. Specimens of dimensions 3 by 6 by 0.5 mm were prepared and then subject to a constant stress of 100 kPa under a temperature ramp from 35 to 250°C at 3°C/min while monitoring the strain. Formulations containing the difunctional acrylate (DFA) and reactive diluent acrylate (RDA) had lower observed transition temperatures than their methacrylate alternatives (difunctional methacrylate (DFMA) and reactive diluent methacrylate (RDMA) (Figure 10). Formulations containing the DFA and RDA had lower transition temperatures than DFMA and RDMA. This is expected because of the lack of methyl substitute in the acrylates resulting in a more flexible polymer backbone. This transition temperature is most likely the Tg and aligns with results for similar materials found in literature. The self-healing transition temperature, the topology freezing temperature (Tv), is visible as an increase in the strain rate above the Tg in the formulations with lower Tgs but is not very pronounced.To increase the visibility of the Tv and increase the self-healing properties of the polymer, a catalyst will be added. Dynamic dual cantilever tests will also be done using the DMA to confirm that the lower transition temperature is the $T_g$.

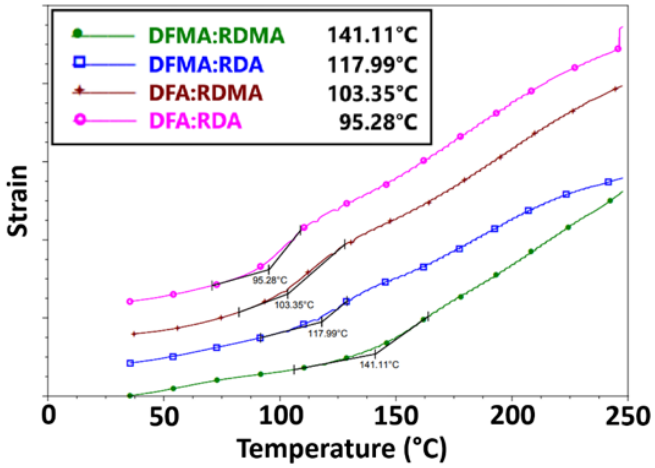


Figure 10. Dilatometry results from the various self-healing polymer formulations.

*b) Homopolymer Mechanical Properties:*

Four monomers were UV-cured into homopolymers and mechanically tested to get a baseline of their mechanical properties. These four are the difunctional methacrylate (DFMA), difunctional acrylate (DFA), reactive diluent methacrylate (RDMA), and reactive diluent acrylate (RDA). RDMA was very brittle compared to RDA which polymerized into a soft elastomer that was not tensile tested. Both DFMA and DFA had extremely high viscosities at room temperature. The better properties of DFA over DFMA is thought to be because the more reactive acrylate groups led to a higher conversion leading to a higher crosslinked polymer (Figure 11).

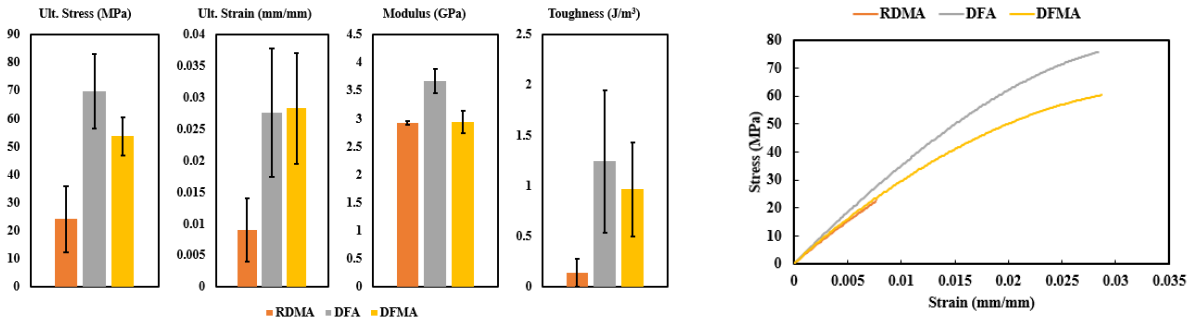


Figure 11. (left) The tensile properties of DFMA, DFA, and RDMA and (right) the representative tensile curves for each formulation.

*c) Copolymer Mechanical Properties:*

The two difunctional monomers (DF) and two reactive diluents (RD) were mixed at a 1:1 acrylate/methacrylate functional group ratio to create four formulations that each contained one DF and one RD. The formulation used in previous results is the DFMA: RDMA formulation. As predicted by the homopolymer tensile properties, formulations containing RDA had a higher ultimate strain, lower modulus, and higher toughness than formulation with RDMA. A similar trend is seen when comparing DFMA and DFA. Surprisingly, the ultimate strengths of all formulations were very similar to each other (Figure 12). ANOVA analysis confirms that the average ultimate strengths are not different enough from each other to reject the null hypothesis.

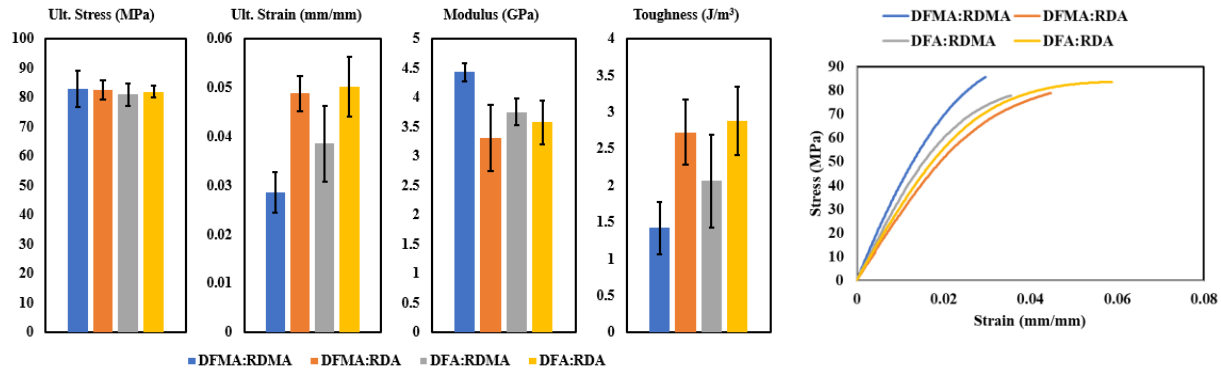


Figure 12. (left) The tensile properties of DFMA: RDMA, DFMA: RDA, DFA: RDMA, and DFA: RDA and (right) the representative tensile curves for each formulation.

### 3.2.2. (Task 2.2) Investigating Self-Healing and Mechanical Properties of Vitrimer Epoxy Resins

investigated the self-healing and mechanical performances of the self-healing polymer in subtask 2.1, the tensile and self-healing properties were evaluated, and the results are presented below:

*3.2.2.1. Self-Healing in UV-Cured Resin with Nanoparticle (selected Resin-to-MRD ratios of 1:1 formulation):*

*a) Self-Healing Testing with Varied Nanoparticles:*

To work with the samples in Section 3.1.1.2, adhesive layers with uniform thickness were incised through their entire thickness using a razor blade to ensure consistent cut profiles across samples. The dimensions of each cut, including depth and profile, were assessed with a KEYENCE microscope both prior to and subsequent to the healing process. Healing was achieved by subjecting the coatings to a hot press at 180°C and 500 lbs. pressure for a duration of 10 minutes. To calculate the average repair efficacy and its standard deviation, multiple incisions were made in each sample, with measurements taken before and after the healing process (Figure 13). The groups showing successful curing included those with 0.1 and 0.5 ND, and 0.1 GNP, with all formulations exhibiting an average repair ratio between 93.5-94.5%, excluding the 0.1% ND formulation, which demonstrated a repair ratio of 72%. The lower repair ratio in the 0.1% ND sample is attributed to an inconsistent coating thickness, which led to uneven heating; only the thickest regions at the top and bottom of the substrate made effective contact with the hot plates, resulting in more significant healing in those areas. Figure 14 presents profile images of the cuts both before and after the healing process, corroborating the measured depth values. Concentrations of 0.1 to 1.0 wt.% for CNT, GNP, and ND were tested. All CNT samples and GNP samples at 0.5% and 1.0% concentrations impeded the UV-curing process, likely due to nanoparticles blocking UV light, preventing full curing. Successful curing was achieved with 0.1 and 0.5 ND, and 0.1 GNP samples

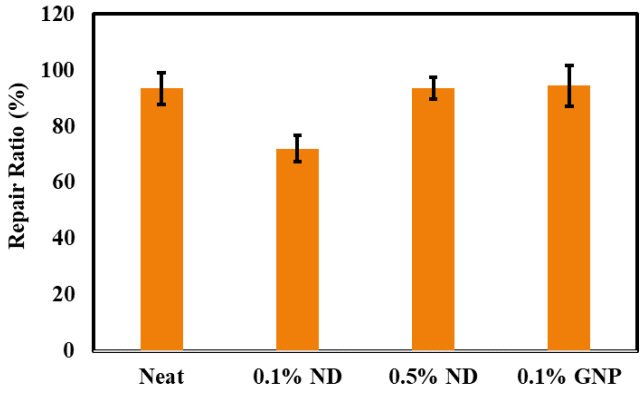


Figure 13. Repair ratio based on change in depth of the cut for the neat, 0.1% ND, 0.5% ND, and 0.1% GNP formulation.

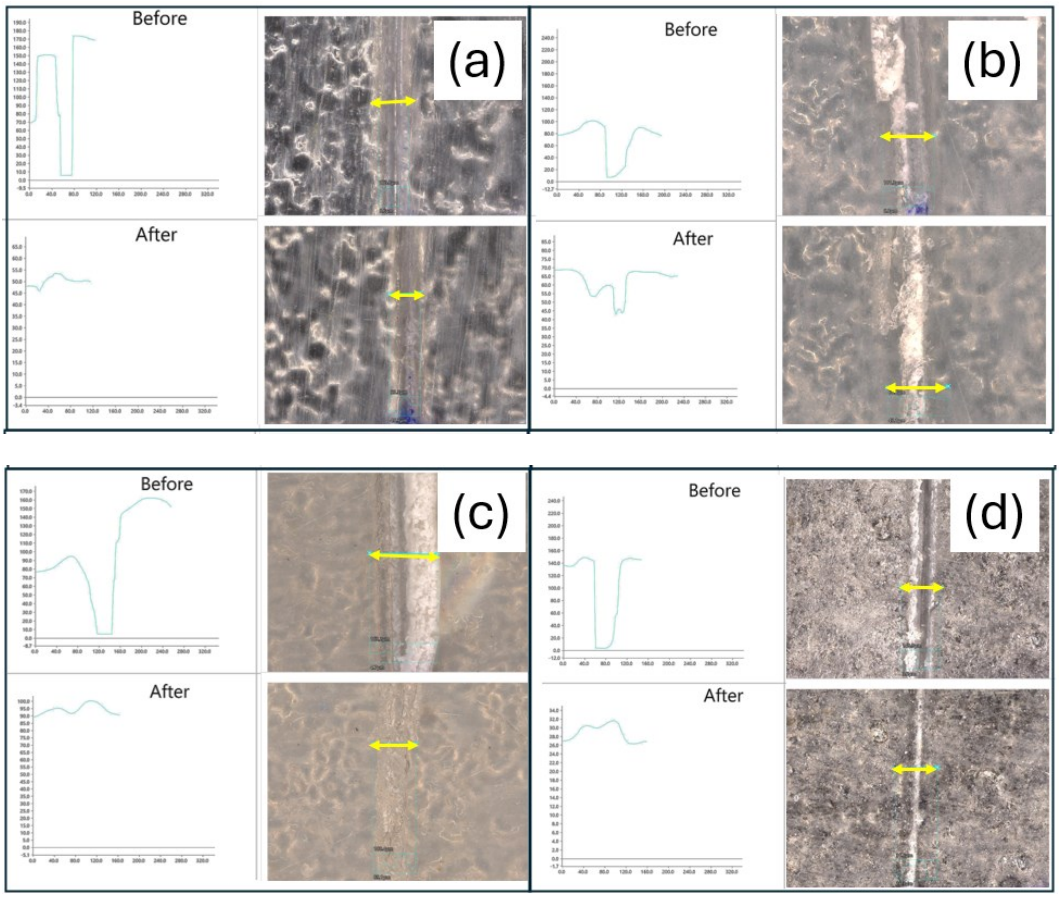


Figure 14. Profile images of before and after healing the (a) neat 1:1 formulation, and 1:1 formulation with (b) 0.1% ND. (c) 0.5% ND, and (d) 0.5% GNP.

*b) Corrosion Resistance of Self-Healing Polymer (selected Resin-to-MRD ratios of 1:1 formulation) with 0.5% Nanodiamond:*

Samples of the neat self-healing polymer, both with and without 0.5% nanodiamond coatings (approximately 200 µm thick), were subjected to 500 hours of exposure in the B117 salt spray chamber. Throughout this period, no visible signs of corrosion were observed in any of the samples (as shown in Figure 15 (c)). These findings were supported by electrochemical impedance spectroscopy (EIS) results, which demonstrated strong alignment with the visual observations (Figures 15 (a) and (b)).

Notably, the 0.5% nanodiamond (ND) reinforced samples exhibited superior performance compared to the neat polymer. The EIS data revealed slightly higher Zmod values for the ND-reinforced specimen, indicating improved corrosion resistance. The impedance value at the lowest test frequency is commonly used to assess corrosion resistance. As a result, we can observe that the addition of 0.5% nanodiamonds (ND) generally leads to higher impedance values, indicating improved corrosion resistance. The testing will continue until significant differences are observed. However, the obtained results already suggest that the incorporation of nanodiamonds not only enhances mechanical properties but also offers additional protective benefits against corrosion, making it a promising candidate for advanced protective coatings.

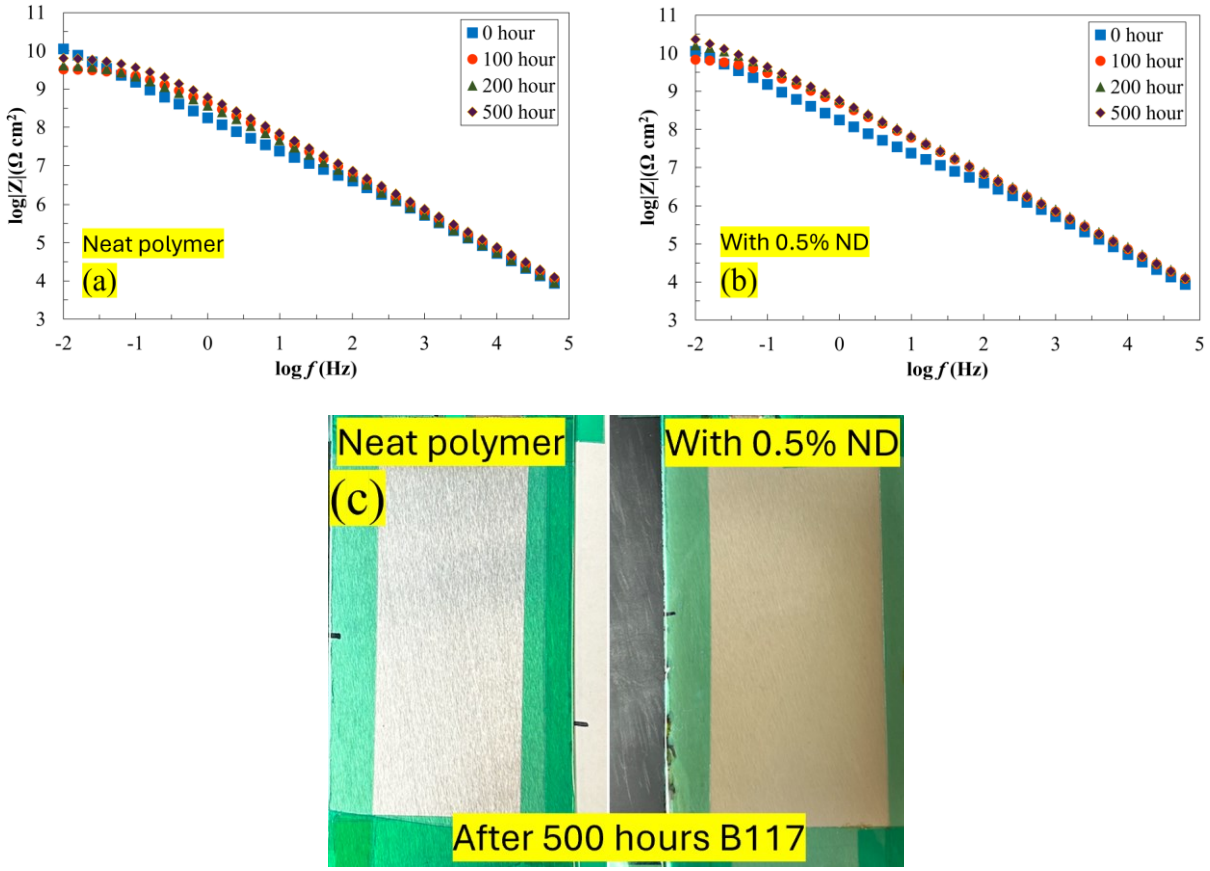


Figure 15. (a)(b) EIS curved of neat self-healing polymer and 0.5% specimen after 500 hours salt spray. (c) Picture of a typical specimen after 500 hours salt spray.

### 3.2. (Task 3) Enhancing Mechanical and Boning Performances and Reducing Permeability of the Healable CIPP Structural Lining Through Nanofiller

This section works closely with Task 2 in developing the formulation of self-healing polymers. As a result, the majority of the work related to self-healing polymers in Task 3 focuses on this new formulation in Section 3.1.1.2., both with and without the addition of 0.5% nanodiamonds (ND).

#### 3.2.1. (Task 3.1) High Mechanical Performance

Based on our previous study, the addition of 0.5% nanodiamonds (ND) resulted in significant improvements in several key properties relevant to this project, including dispersion, mechanical strength, bonding performance, and corrosion resistance. The selection of the self-healing polymer is based on the results from Task 2, where the developed self-healing polymer formulation (DFMA: RDMA 1:1) in Section 3.1.1.2. was chosen for further investigation with the incorporation of 0.5% ND.

The previous findings in nanoparticle reinforcement study demonstrated that 0.5% ND provides excellent overall mechanical properties in commercially available epoxy polymers, while also having no significant negative impact on the curing rate of the self-healing polymer under UV

light. The spherical geometry of the ND particles plays a crucial role in this improvement, as it enhances the uniform dispersion of the composite material, leading to notable performance gains. Additionally, the spherical shape of the ND particles prevents them from obstructing UV light during the curing process, ensuring efficient polymerization of the self-healing polymer.

*a) Flexural Properties of Self-Healing Polymer with 0.5% Nanodiamond:*

As presented in Figure 16, nanoparticle reinforcement with 0.5% nanodiamonds (ND) was selected for further evaluation to assess its reinforcing effect when added to the developed self-healing polymer. The following section presents the flexural properties of the self-healing polymer reinforced with 0.5% ND. It was observed that the addition of 0.5% ND resulted in a significant improvement in the mechanical properties, with a 10% increase in flexural strength compared to the polymer without reinforcement. This improvement in flexural strength indicates that the nanodiamonds contribute to enhancing the polymer's ability to resist deformation under stress, which is crucial for applications where the material is subjected to bending forces. The uniform dispersion of the ND particles within the polymer matrix likely plays a key role in this enhancement, helping to distribute stress more evenly and prevent localized failure.

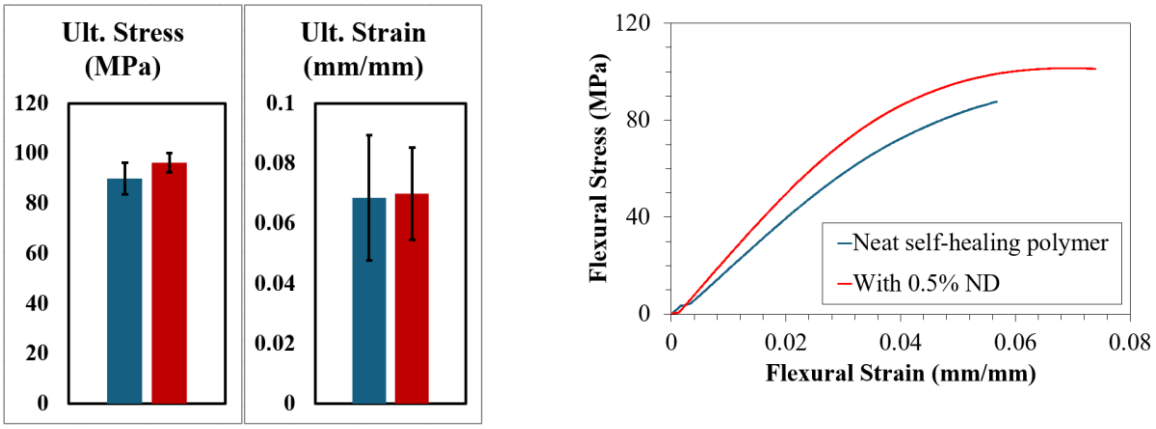


Figure 16. (left) The flexural properties of development self-healing polymer with 0.5% of ND and (right) the representative stress vs. strain curves.

*b) Abrasion Resistance of Self-Healing Polymer with 0.5% Nanodiamond:*

The abrasion resistance of the self-healing polymer was notably improved by the addition of 0.5% nanodiamonds (ND). This enhancement is evident from the reduced mass loss after the abrasion test, as shown in Table 1. The neat self-healing polymer exhibited a mass loss of 0.0245 g, whereas the polymer reinforced with 0.5% ND experienced a lower mass loss of 0.0207 g, indicating better resistance to wear. In addition to improved abrasion resistance, the surface roughness of the polymer after abrasion was also reduced with the inclusion of ND. The neat self-healing polymer showed a surface roughness of 1.258 µm post-abrasion, while the ND-reinforced sample demonstrated a lower roughness value of 1.183 µm. This reduction in surface roughness further supports the conclusion that the nanodiamonds not only enhance mechanical durability but also contribute to a smoother surface after wear.

These results suggest that the incorporation of ND into the self-healing polymer significantly improves its overall wear resistance, making it more durable and suitable for applications where surface wear is a concern. The ability to maintain lower mass loss and smoother surface finish

under abrasive conditions is a crucial advantage in industries where materials are exposed to constant friction and wear.

Table 2 Abrasion resistance of self-healing polymer with 0.5% ND

| Sample | Mass Loss (g) | Roughness after Abrasion (µm) |
|---|---|---|
| Neat self-healing polymer | 0.0245 | 1.258 |
| Self-healing polymer with 0.5% ND | 0.0207 | 1.183 |

*c) Long-Term Flexural Creep of Self-Healing Polymer with 0.5% Nanodiamond:*

A long-term flexural creep test was started for the self-healing polymer with nanoparticles (nanodiamonds). Static loads of 12, 24, and 36% of the load at failure were applied to each formulation, and the deflection was measured at intervals for a total test time of 1000 hrs. (Figure 17). The test is currently ongoing, and the final results will not be obtained until the test is complete.

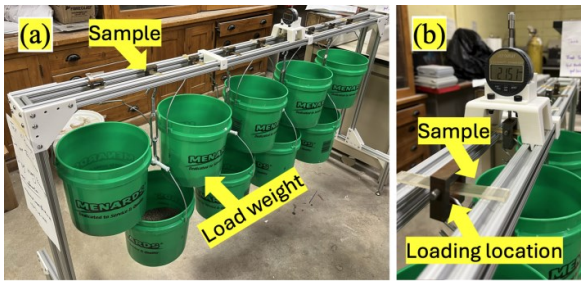


Figure 17. The (a) long term flexural creep device with 9 specimens being tested simultaniously and (b) the deflection of one of the specimen being measured using a digital dial indicator.

### 3.2.2. (Task 3.2) Enhanced Bonding Performance

*a) Bonding Property of Self-Healing Polymer with 0.5% Nanodiamond:*

Figure 18 illustrates the mechanical performance of neat and nanodiamond (ND)-reinforced self-healing polymers, highlighting the significant enhancements in ultimate stress, strain, modulus, and toughness with the addition of 0.5% ND. The ND-reinforced samples demonstrated a clear improvement in ultimate stress, increasing from approximately 9 MPa in the neat polymer to around 13 MPa. This indicates that the ND-reinforced polymer can withstand greater loads before failure, a crucial property for structural applications where strength is essential. Moreover, the substantial improvement in ultimate strain suggests enhanced flexibility, enabling the material to endure more deformation under mechanical loads.

Toughness, which represents the material's ability to absorb energy before failure, exhibited the most notable improvement. The ND-reinforced samples displayed a significant increase in toughness. This substantial improvement in toughness, combined with the observed plastic deformation in the ND-reinforced specimens, indicates that nanodiamonds enhance not only the material's strength but also its ductility and resilience. The ability of the ND-reinforced polymer to undergo plastic deformation suggests a greater tolerance for stress and a reduced likelihood of brittle failure. These combined improvements make the ND-reinforced self-healing polymer a promising material for use in environments where durability, flexibility, and energy absorption are

paramount.

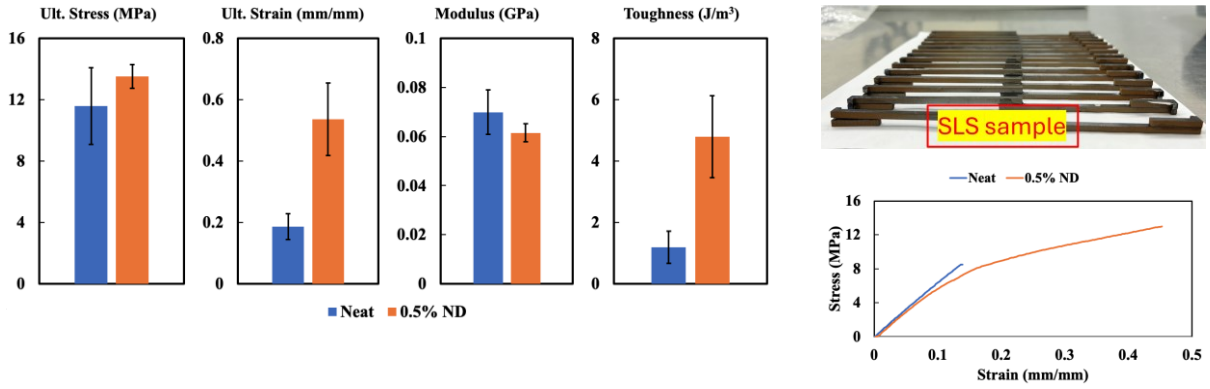


Figure 18. Shear property of self-healing polymer with 0.5% ND

### *3.2.3. Additional to Task 3.1 New Developed Nanoparticle Dispersion Method Based on Carboxymethyl Cellulose (CMC) Functionalization:*

In addition to the mechanical dispersion method previously used in this project, the research team conducted an experimental study on nanoparticle reinforcement by developing a new nanoparticle dispersion technique. This new method was applied to an experimental study focusing on nanoparticle reinforcement in neat epoxy.

The team introduced a novel functionalization technique using carboxymethyl cellulose (CMC) to improve nanofiller dispersion. This method eliminates the need for ultrasonication and high-speed dispersion, resulting in lower energy consumption and reduced dispersion time. All three nanofillers were functionalized using the same surface treatment process. The weight concentrations of CMC and nanofillers (0.5%, 1.0%, 1.5%, and 2.0%) were consistent with those used in the previous dispersion method.

Surface characterization of the CMC-modified nanoparticles and the mechanical properties of the resulting nanocomposites were evaluated, with the results presented in Figure 19. This approach offers a more efficient and energy-saving solution for nanoparticle dispersion while maintaining consistency in nanofiller concentration and improving material properties.

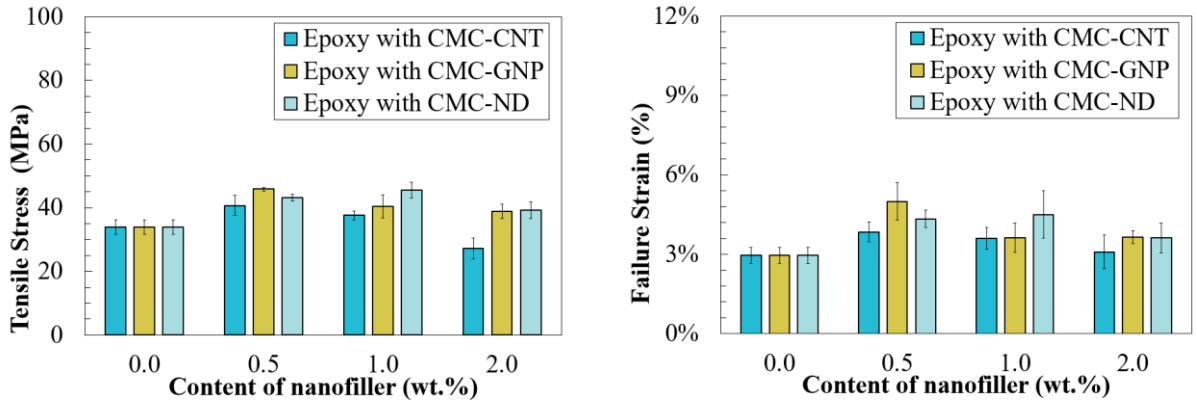


(a) (b)

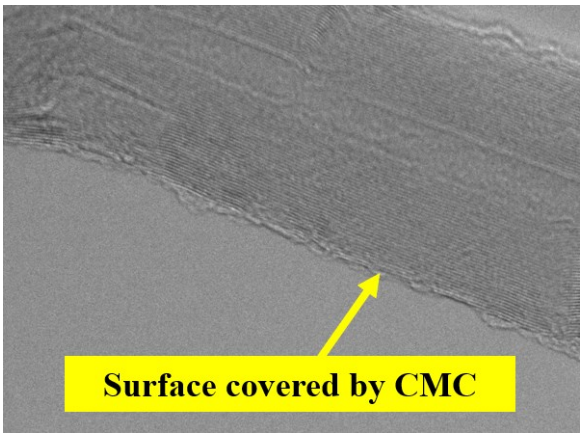


(c)

Figure 19. (a) TEM image of CMC modified CNT. (b) Tensile strength and (c) failure strain of samples reinforced by CMC modified CNT, GNP, and ND.

This investigation was further extended to include evaluations of abrasion resistance and adhesion properties, as illustrated in Figure 20. The results clearly demonstrate significant improvements in both abrasion resistance and substrate adhesion for all nanoparticles functionalized with CMC. Notably, the nanodiamonds (ND) showed the most substantial overall enhancement in performance.

The incorporation of CMC-functionalized ND into the epoxy matrix led to a marked increase in abrasion resistance, evidenced by reduced mass loss and smoother surface profiles after abrasion tests. These improvements suggest that the enhanced dispersion of ND particles, facilitated by the CMC functionalization, provides superior protection against surface wear, making the material more durable under mechanical stress. In terms of adhesion properties, the CMC-functionalized nanoparticles also exhibited enhanced bonding to the substrate. This improvement is critical for applications requiring strong interfacial adhesion, as it ensures that the nanocomposite remains intact under stress and prevents delamination. The superior performance of ND in both abrasion and adhesion metrics highlights its potential as an effective reinforcement material for advanced epoxy composites, particularly when processed using the CMC dispersion method.

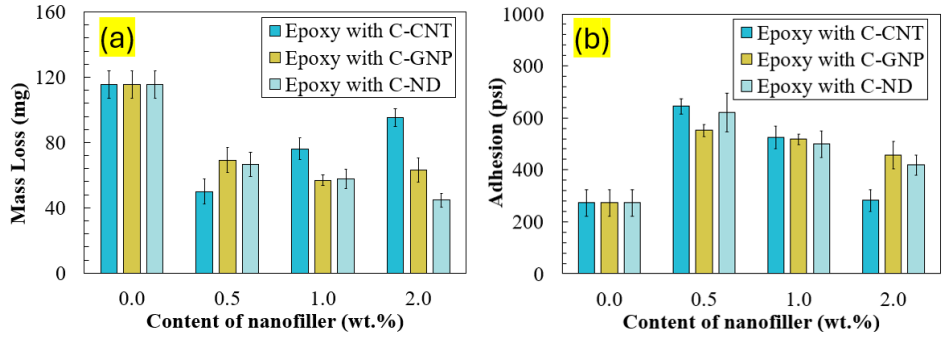


Figure 20. (a) Abrasion resistance and (c) adhesion/bonding to substrate of samples reinforced by CMC modified CNT, GNP, and ND.

### 3.2.4. (Task 3.3) Reducing the Permeability and Investigating the Interfacial Bonding Chemical Analysis

Highlights from Task 3.3 include (1) Nanopore Dynamics and Hydrogen Interaction Studies: (a) Model Construction and Simulation: Initial efforts involved constructing nanopore models (kaolinite, graphene) and evaluating hydrogen interaction dynamics using MD simulations. (b) Surface Interaction Analysis: Comparisons between nanopore surfaces revealed how hydrogen adsorption and transport are influenced by molecular structure. (c) Pressure and Confinement Effects: Studies on varying pressures and confinement showed their impact on hydrogen diffusion and transport. (2) Vitrimer Polymerization Dynamics: (a) Model Development: Both non-reactive and reactive vitrimer models were explored to understand polymerization and hydrogen adsorption. (b) Environmental Influence: Factors such as temperature, pressure, and setup conditions were analyzed to assess their effects on polymerization dynamics.

*3.2.4.1. Developing Computational Models to Simulate Hydrogen Diffusion Properties on Nanoparticle Surface:*

*a) Nanopore Surface Comparisons:*

When investigating hydrogen storage, one must consider the possibility of hydrogen loss by leakage through nanopores or by hydrogen adsorption and reactions at surfaces. Figure 21 illustrates hydrogen density profiles and self-diffusion coefficients in kaolinite pores with inward-facing surfaces of $AlO_4(OH)_2$ and $SiO_4$. The results in Figure 21 display insignificant changes in hydrogen properties from one kaolinite surface to the other. Consequently, it is concluded that the kaolinite surface compositions do not influence $H_2$ transport due to weak interactions with both surfaces in general. Therefore, for this work, further results for $H_2$ in kaolinite pores will only be presented from simulations utilizing inward-facing $AlO_4(OH)_2$ surfaces.

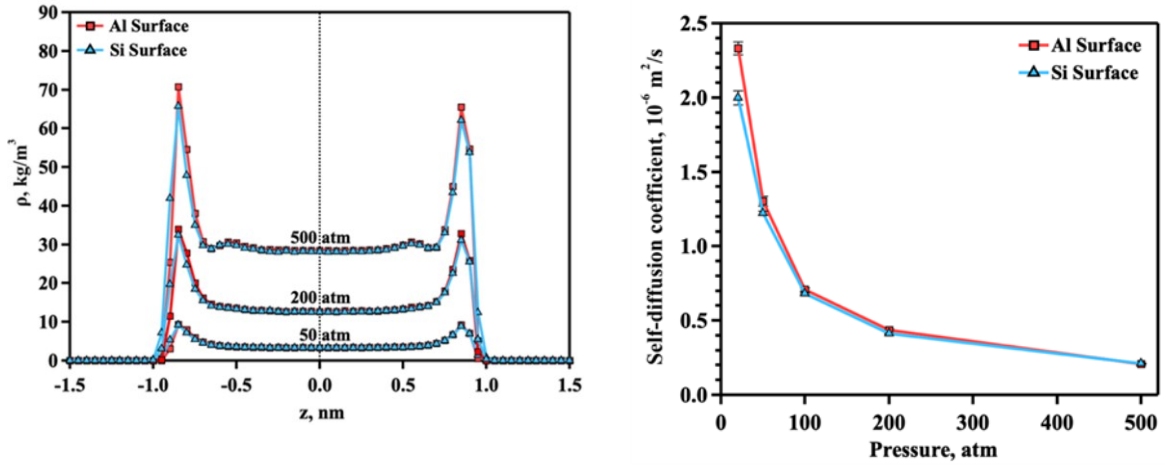


(a) (b)

Figure 21. $H_2$ in 2 nm kaolinite pores with inward-facing surfaces of $AlO_4(OH)_2$ and $SiO_4$. (a) Density profiles along the z-direction (lower pore surface to upper pore surface) and (b) total self-diffusion coefficients

*b) Interaction of Hydrogen in Kaolinite and Graphene Nanopores:*

Figure 22(a) shows negative values for interaction energies between hydrogen and both pore types, indicating an affinity of $H_2$ molecules for the wall surfaces. However, the results reveal that attractive intermolecular interactions between $H_2$ molecules and graphene are more than double those between $H_2$ molecules and kaolinite. $H_2$ molecules lining the graphene pore surfaces at a density ~35% higher than the kaolinite pore surfaces at pressures of 100 and 500 atm, indicating $H_2$ clearly prefers interacting with graphene. Strong attraction to and adsorption of gas molecules at pore surfaces can also be evidenced by increasing trends in self-diffusion coefficients with increasing pressure.

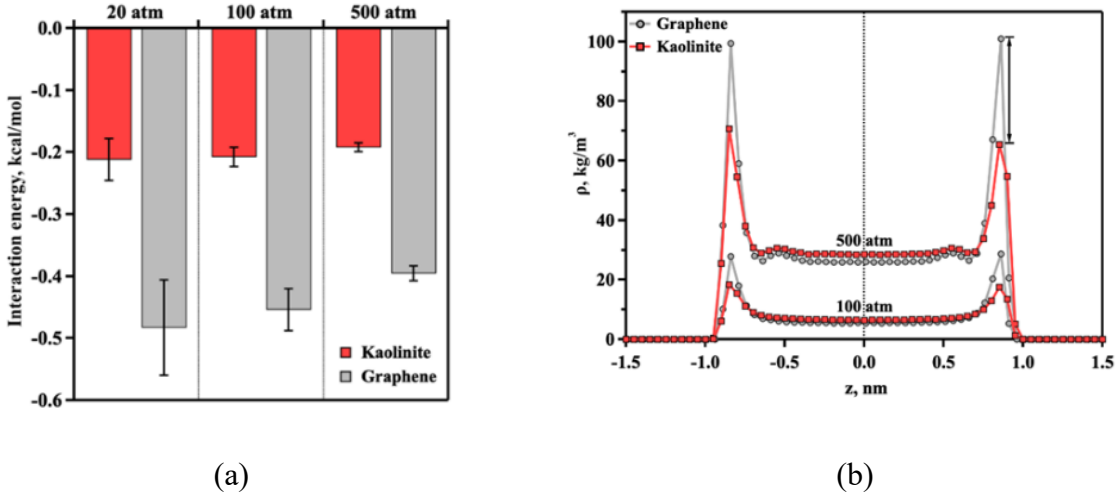


(a) (b)

Figure 22. Interaction of $H_2$ in 2 nm kaolinite (Al surface) and graphene pores. (a) Normalized gas-solid interaction energies, and (b) z-direction density profiles under 20-500 atm.

*c) Pressure and Confinement Effects on Diffusion Process of $H_2$:*

Figure 23 shows that at 20 atm, self-diffusion coefficients range from ~$3.5 \times 10^{-6}$ $m^2/s$ to ~$6.5 \times 10^{-6}$ $m^2/s$ in kaolinite pores and from ~$5.5 \times 10^{-6}$ $m^2/s$ to ~$7.0 \times 10^{-6}$ $m^2/s$ in graphene pores of 2 nm to 20 nm, respectively. The values agree with experimental data for $H_2$ transport on graphite surfaces, on the order of $10^{-7}$-$10^{-6}$ $m^2/s$. As pore size increases, self-diffusion coefficients begin to approach that of bulk $H_2$. In the case of kaolinite, the increase in self-diffusion coefficient from the 2 nm pore to bulk $H_2$ follows a somewhat linear trend. However, for graphene, this coefficient exhibits negligible changes once the pore size exceeds 10 nm.

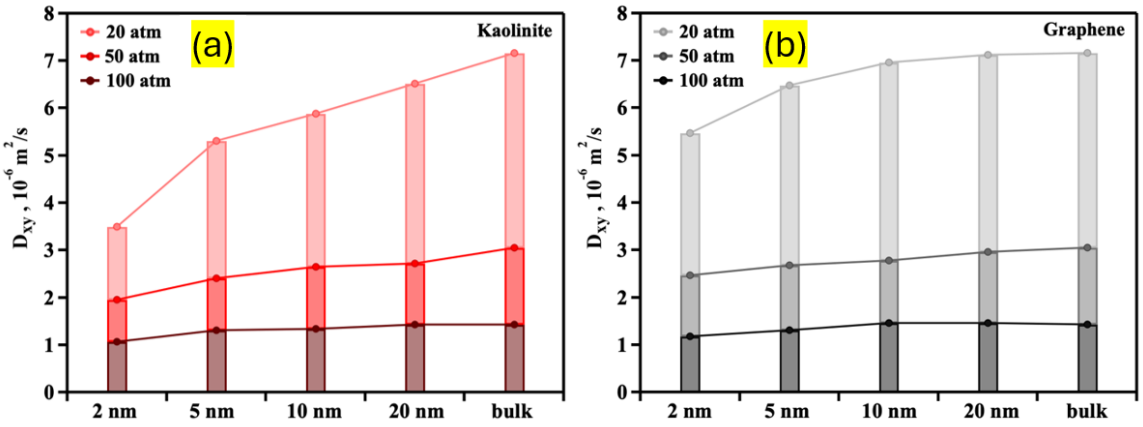


Figure 23. Lateral self-diffusion coefficients for $H_2$ in 2-20 nm (a) kaolinite (Al surface) and (b) graphene pores compared to those for bulk $H_2$ at pressures of 20, 50, and 100 atm.

*d) Quantitative Analysis of Hydrogen Sulfide's ($H_2S$) Impact on Gas-Water Interfacial Tension:*

We leverage molecular dynamics simulations to elucidate the dynamics of interfacial tension between residual water and gas mixtures comprising hydrogen ($H_2$), methane ($CH_4$), and H2S within the porous media. The findings significantly advance our understanding of in-pore storage and transport mechanisms by demonstrating that even a minimal concentration of $H_2S$ leads to a considerable reduction in interfacial tension (IFT), a factor critical for optimizing pipeline hydrogen transport operations. As shown in Figure 24, the interfacial properties such as adsorption, absorption, and orientation affect the gas-water interfacial properties. The density profiles we observed in Figure 24 show notable variations among the different gases at the interface. $H_2$ exhibited a pronounced reduction in density near the interface, suggesting minimal presence of $H_2$ molecules within this region. In contrast, the density of $CH_4$ peaked at the interface, indicative of $CH_4$ adsorption at the interface, highlighting the affinity of $CH_4$ molecules for this boundary and echoing the observations of several prior studies. The $H_2S$ profile was particularly distinct, revealing a significant concentration of $H_2S$ molecules within the interface region. This can be interpreted as a result of $H_2S$ absorption into the water phase, which is in line with the insights provided by previous research.

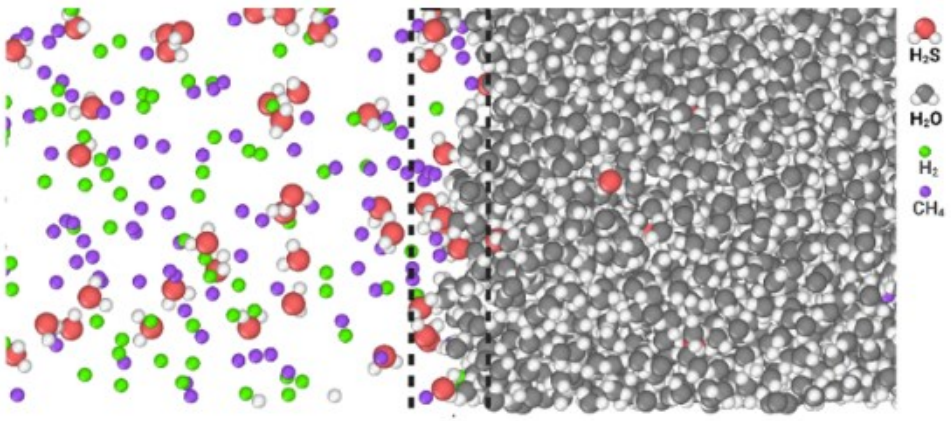

(a)

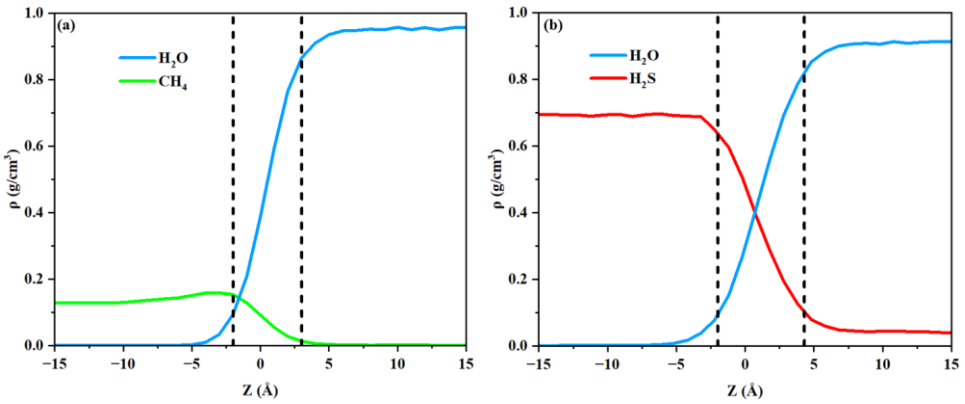


(b)

Figure 24. (a) The schematic illustration of the gas-water interface, Density profiles at 343 K and 14.5 MPa: (b) $CH_4$-$H_2O$; (c) $H_2S$-$H_2O$.

*e) Interfacial Tension Dynamics:*

We also examined the impact of hydrogen sulfide ($H_2S$) on gas-water interfacial tension and permeability. Figure 25(Left) illustrates the relationship between IFT and $H_2S$ concentration for binary systems of ($H_2S$+$H_2$)/$H_2O$ and ($H_2S$+$CH_4$)/$H_2O$ at 343 K and 14.5 MPa. Our findings demonstrate a trend where IFT diminishes with escalating concentrations of $H_2S$. Notably, at a minimal $H_2S$ concentration of 5%, the IFT reduction is pronounced, registering at approximately 12% for the ($H_2S$+$H_2$)/$H_2O$ system. In stark contrast, the ($H_2S$+$CH_4$)/$H_2O$ system exhibits only a 6% reduction in IFT under the same concentration. This comparative analysis suggests that $H_2S$ exerts a more substantial influence on IFT when interacting with $H_2$ than $CH_4$ in an aqueous environment. It is also worth noting that the diminution of IFT becomes more pronounced as $H_2S$ concentration increases beyond the 10% threshold, indicative of a significant influence of $H_2S$ on the gas-water IFT across both binary systems studied. Yet, it is important to note that such an effect plateaus when the $H_2S$ concentration surpasses 80%, beyond which any further increase in $H_2S$ concentration yields minimal additional impact on IFT.

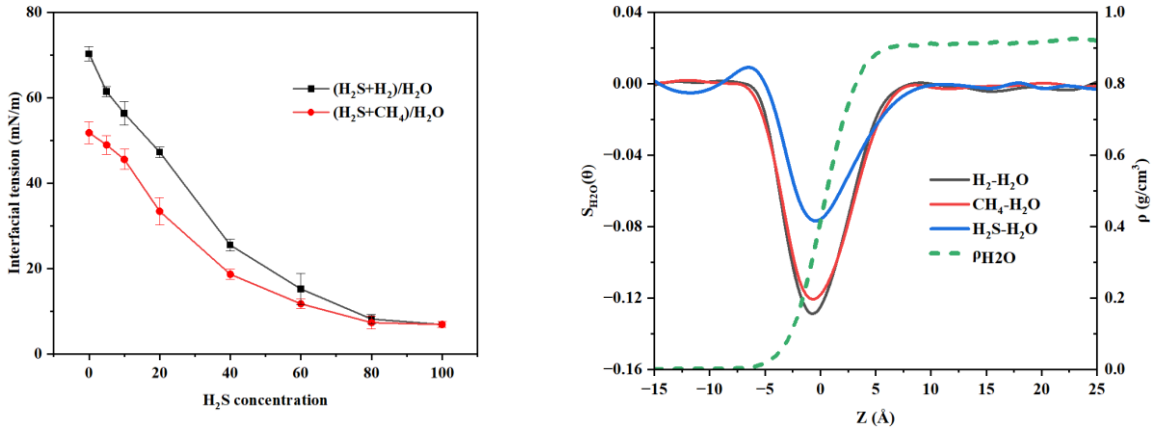

Figure 25. (Left) IFTs at 14.5 MPa and 343 K as a function of $H_2S$ concentration for ($H_2S$+$H_2$)/$H_2O$ and ($H_2S$+$CH_4$)/$H_2O$ systems; (Right) Orientation profiles of $H_2O$ molecules along the Z direction in three binary gas-water systems. The water density profile is used to locate the gas-water interface region.

Figure 25(Right) shows the molecular orientation profiles for water in $H_2$-$H_2O$, $CH_4$-$H_2O$, and $H_2S$-$H_2O$ systems, illustrating the spatial orientation of water molecules across the Z direction. These profiles leverage the local density profile of $H_2O$ to demarcate the gas-water interface. In the bulk water phase, the orientation order parameter (S) values approximate zero, reflecting a lack of preferential orientation and a random distribution of molecular dipoles. Conversely, negative S values within the interface region reveal a distinct trend in which water molecules prefer to align parallel to the interface. Notably, the S values for water in the $H_2$-$H_2O$ and $CH_4$-$H_2O$ systems are more negative than those in the $H_2S$-$H_2O$ systems. This suggests that in the absence of $H_2S$, water molecules at the interface exhibit a stronger preferential parallel orientation. The incorporation of $H_2S$ into the water matrix attenuates the sharpness of the phase boundary, potentially transitioning the interface from a distinctly immiscible to a more partially miscible state. This interaction may explain the more randomized orientation of water molecules observed at the $H_2S$-enriched interface, indicative of the modulating effect of $H_2S$ on the structural characteristics of the interfacial region.

*3.2.4.2. Development of Vitrimer Models*

*a) Development of Non-reactive Vitrimer Model:*

During this reporting period, we initiated the development of vitrimer models, starting with a non-reactive vitrimer model. We continued studying hydrogen adsorption within the non-reactive vitrimer model and began developing a reactive vitrimer model. Additionally, chemical analysis was performed to assess surface bonding and permeability, focusing on the impact of hydrogen sulfide ($H_2S$) on gas-water interfacial tension.

As shown in Figure 26, the non-reactive vitrimer model does not express dynamic polymerization reactions between the two monomers, namely, bisphenol a diglycidyl ether (DGBEA) and 2-aminophenyl disulfide (AFD). The vitrimer model was generated by randomly mixing 296 DGEBA and 148 AFD monomers in a simulation box with an initial density of 0.3 g/cm$^3$. Five MD simulations were performed with the NPT ensemble, where the temperature and pressure were maintained at 300 K and 1 atm, respectively. Each of those five simulations had a trajectory of 5 ns at the timestep of 1 fs. The inter- and intra-interactions were treated by the Polymer Consistent Force Field (PCFF), a Class II force field, using partial charges from the literature. The equilibrium vitrimer model has a density of 1.06 g/cm$^3$, agreeing well with the 1.12 g/cm$^3$ literature report.

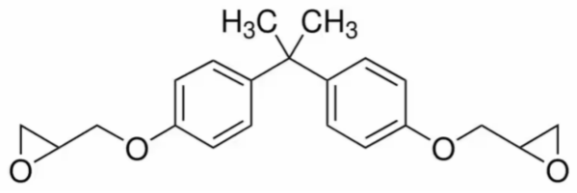


Bisphenol A diglycidyl ether (DGBEA)

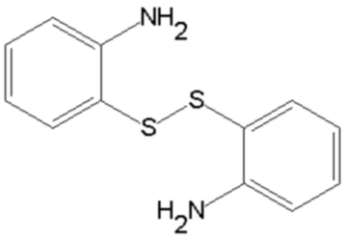


2-Aminophenyl disulfide (AFD)

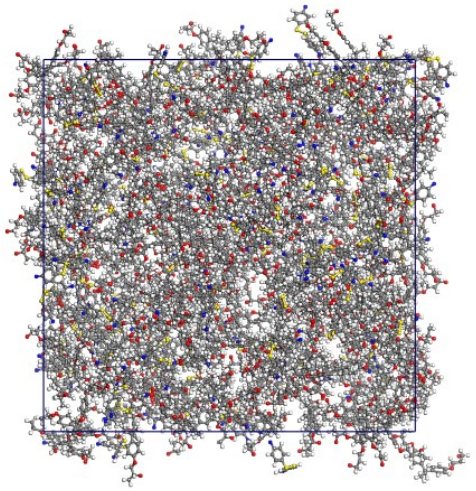

Figure 26. A non-reactive vitrimer model: **(Top)** Molecular structures of the two monomers, DGBEA and AFD; **(Bottom)** The final equilibrium structure of the vitrimer model, composed of 296 DGEBA and 148 AFD molecules, with a density of 1.06 g/cm$^3$ at 300 K and 1 atm

*b) Hydrogen Adsorption in the Developed Non-reactive Vitrimer Model:*

Adsorption calculation of hydrogen in the non-reactive vitrimer model was performed at 300 K and 1 atm. To explore the maximum loading of hydrogen in the non-reactive vitrimer model, we calculated $10^5$ MC runs with the Metropolis method to equilibrate the system, followed by $10^8$ production steps, and the results were presented in Figure 27. Three movements, namely, exchange, rotate, and translate, were randomly sampled in the ratio of 20:1:20. The average loading of hydrogen was reported to be 6.833 $H_2$ molecule/cell, with the isosteric heats of 1.063 kcal/mol. It is worth noting that the vitrimer has a chemical formula of C7992H8288N296O1184S296. Therefore, the loading of 6.833 $H_2$ molecule/cell suggests that there is negligible hydrogen adsorption in the vitrimer.

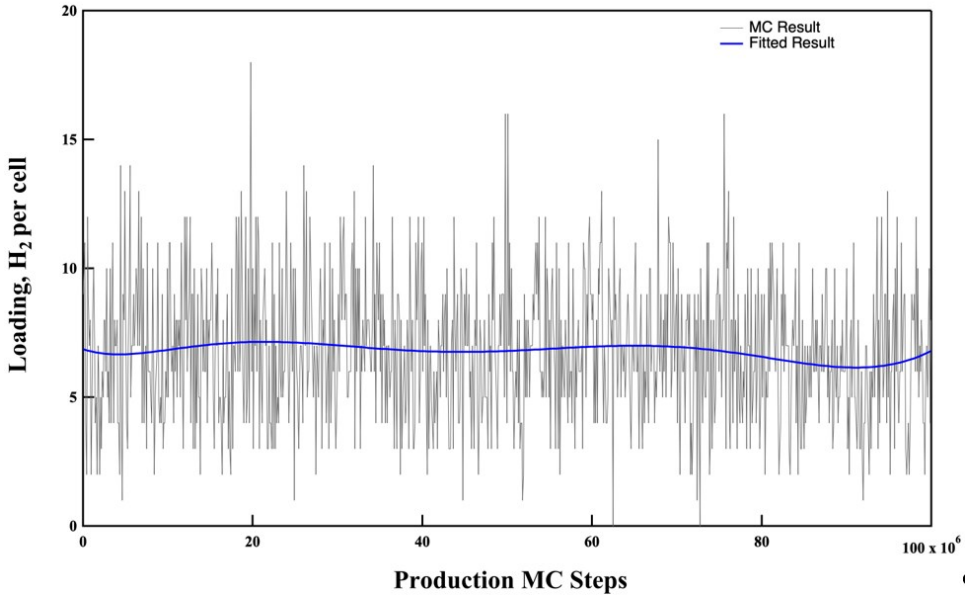


Figure 27. Hydrogen loading in the non-reactive vitrimer model at 300 K and 1 atm.

*c) Reactive Vitrimer Model:*

As illustrated in Figure 28, a reactive vitrimer model could be developed by enabling curing reactions not based on force-field reaction modeling but as a bonding procedure for atoms mimicking chemical reactions. A vitrimer model can be developed by considering the dynamic S-S bond exchange process of AFD, as illustrated in Figure 28. The dynamic exchange of disulfide bonds was modeled as a two-step reaction, with pre- and post-reaction templates constructed along with a reaction map. Bond exchange reactions were enabled when sulfur atoms from different chains came within a cutoff distance of 4.12 Å, with the reaction probability modeled as a function of temperature. We consider such an approach can effectively describe the dynamic nature of the covalent networks of the vitrimer model.

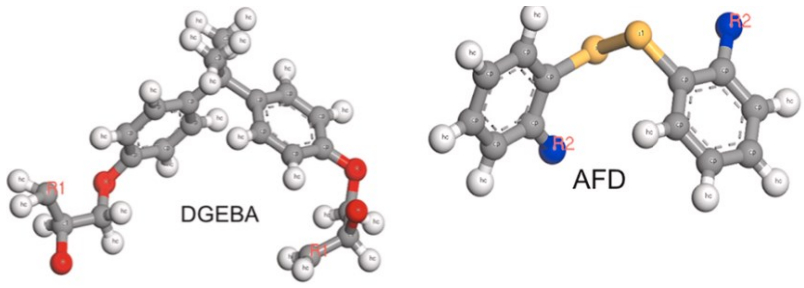


Figure 28. Reactive sites of DGEBA and AFD monomers for a reactive vitimite model.

### 3.2.5. (Task 3.4) Finite Element Numerical Analysis to Guide the Design of the Developed High-Performance Healable CIPP Structural Liner

This task is to computationally analyze the performance of epoxy and liner materials for pipelines under various loading conditions. The investigation includes cast-iron pipes rehabilitated with liners of different thicknesses, varying burial depths, and internal pipe pressures. Additionally, damaged pipes reinforced with CFRP liners and flexural tests for epoxy samples are simulated using finite element analysis (FEA) (Section 3.2.5.1. to 3.2.5.3.). The results of this parametric study will help optimize CIPP liner design and guide trenchless construction and maintenance procedures for pipeline infrastructures. The results in Section 3.2.5.4 are intended to validate the strain signals from the smart liner study conducted in Task 4. Furthermore, we have conducted computational studies on the flexural properties of epoxy samples with different nanoparticle reinforcements to understand the mechanisms of reinforcement (Section 3.2.5.5.).

*3.2.5.1. Finite Element Analysis on Effect of Parameters on the Straight Pipe Integrity*

*a) The Effect of Adhesive Layer Thickness*

The mechanical performance of the straight pipe system with respect to adhesive layer thickness is exhibited in Figure 29. It can be seen that, with the presence of the adhesive layer, the maximum stress on the liner experiences a significant reduction for all three cases. However, the reduction in maximum stress on the pipe is only identified when the hole size is small (25 mm), which is close to the threshold discussed in the validation section. The maximum principal stresses of the pipe become stabilized as the hole size is greater than 50 mm. This phenomenon occurs because the liner can withstand in-pipe pressure when the hole is small, and the pipe remains stable and provides structural support to the system when the hole surpasses a size compensable by the liner. The results also indicate that the stress on the liner is always overestimated in numerical analysis

without consideration of the adhesive layer. For example, when rehabilitating the cast-iron with a 50 mm hole, the maximum principal stress of the CIPP liner is 101.7 MPa, which is beyond its ultimate strength if not include the adhesive layer into consideration. This can result in liner failure and functional loss in the construction field. The solutions are either employing a stronger liner or increasing the liner thickness, which is inevitably increasing budget. However, if the neglect of the adhesive layer can be voided, the maximum principal stress of CIPP liner drops within safe working conditions, and the aforementioned solutions are of no need. Moreover, as for pipes with a relatively smaller corrosion hole, defined as partially deteriorated, 25-mm-radius in our study, the stress is also overestimated; while, pipes identified as fully deteriorated exhibit an overall accurate estimation, as their structural integrity is stable despite the significant effects of corrosion. The addition of the adhesive layer cannot alleviate these effects. The findings of the stress on the adhesive layer are much higher than that in the other two components, which are well aligned with the literature [1].

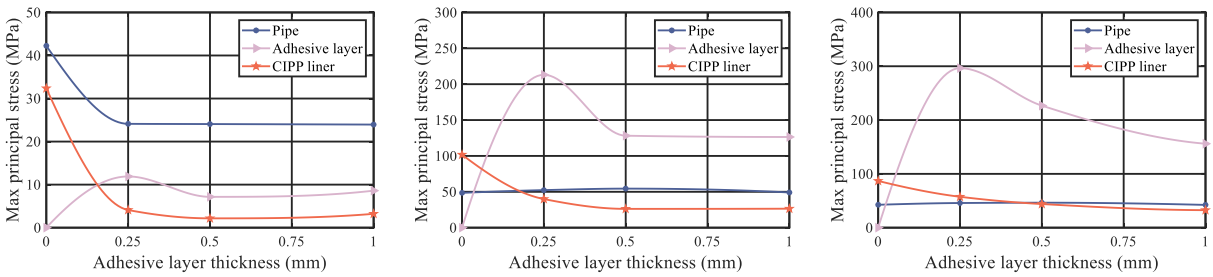


Figure 29. The mechanical performance of damaged straight pipe system with respect of adhesive layer thickness. (a) 25-mm-radius hole, (b) 50-mm-radius hole, (c) 100-mm-radius hole.

*b) The Effect of Interfacial Bonding Condition*

The bonding conditions within the system are further examined through numerical analysis, exploring the adhesion between the pipe and adhesive layer, as well as between the adhesive layer and liner. The bonding condition is simulated using the contact analysis in finite element analysis (FEA), with four friction coefficients ranging from 0 to 1, representing conditions from debonding to complete adhesion. Four numerical models are employed, with two adhesive layer thicknesses (0.25 and 1 mm) and two hole sizes (25 and 100 mm). As illustrated in Figure 30 (a) and (b), it is concluded that the impact of bonding minimally influences pipe performance when the hole size is relatively small (25 mm). However, as the hole size increases, the maximum stress on the pipe exhibits a negative correlation with the bonding condition. Additionally, as the adhesive layer thickness increases, the maximum stress on the pipe decreases, although this effect is discernible when the hole is small, as depicted in Figure 30 (c) and (d). The maximum principal stress of the pipe decreases from 60.05 MPa to 40.74 MPa, as the two interfacial bonding conditions increase from no-bond to full-bond. This result can be explained by energy conservation, as the frictional and strain energy in the system is equal to the internal pressure impact. A better interfacial bonding results in higher frictional energy and lower strain energy in the straight pipe system, leading to lower maximum stress in the pipe. Overall, the findings suggest the bonding between the pipe and adhesive layer has a greater influence on maximum principal stress in the pipe compared to

between the adhesive layer and liner. A stronger interfacial bonding can contribute to a better rehabilitation performance of CIPP liners.

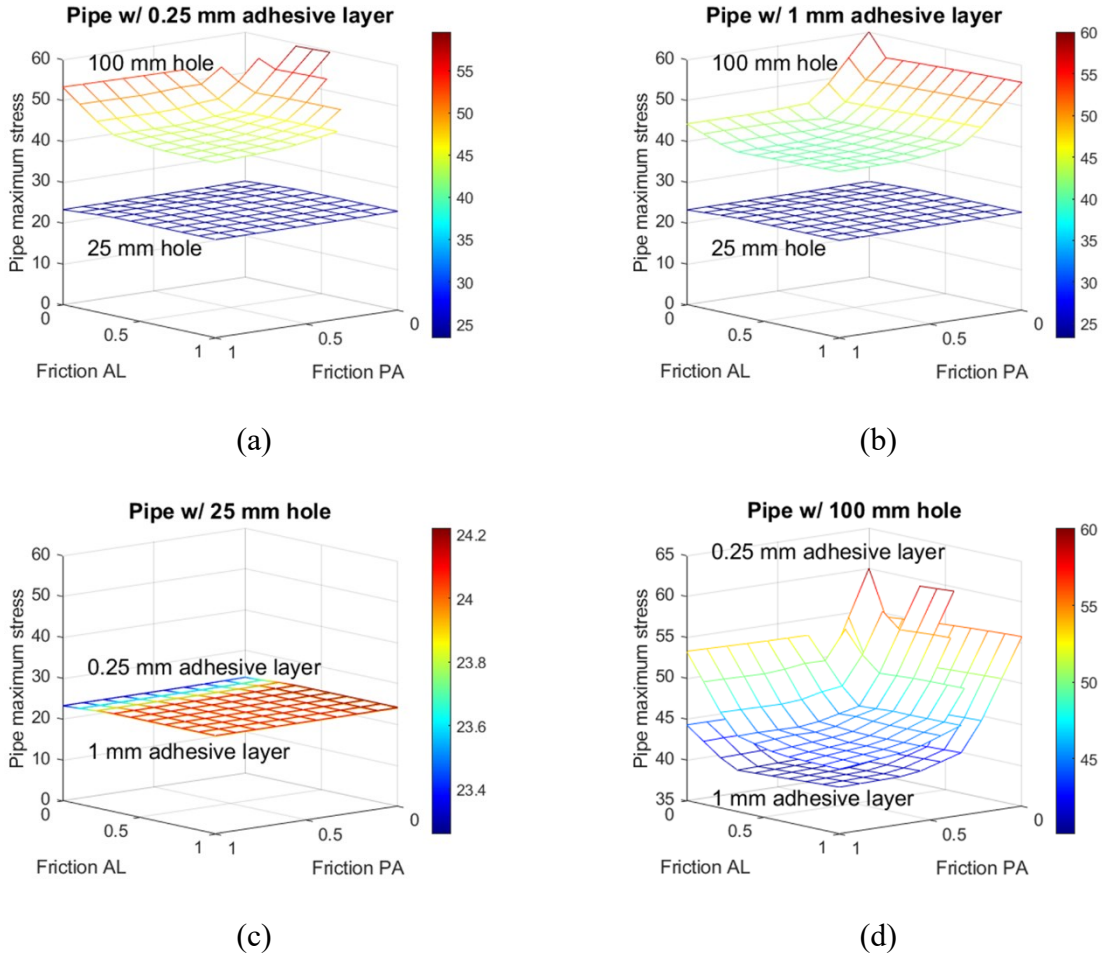


Figure 30. The effect of bonding condition between interfacial layers on pipe maximum principal stress. (Friction PA represents the friction coefficient between pipe and adhesive layer, and Friction AL represents the friction coefficient between adhesive layer and liner.)

*c) The Effect of Corrosion Hole Size*

This section discusses the effect of corrosion hole size on the straight pipe system. The shape of the corrosion hole is a circle, whose center coincides with the central top of the pipe. Figure 31 illustrates the maximum principal stress of the straight pipe system with respect to the corrosion hole size. The maximum principal stress on the pipe increases initially with the growing hole until it reaches 50 mm, approximately one-third of the pipe size. Afterward, it exhibits a slight decrease but remains higher than the stress in the intact pipe. With the consideration of the adhesive layer, the maximum principal stress in the pipe is lower than that without the adhesive layer when the hole radius is less than 40 mm. As the hole size increases, the stress approaches that of the pipe without consideration of the adhesive layer, which is consistent with the previously discussed trends. The thickness of the adhesive layer has a marginal effect on stress in the pipe, which decreases with increasing adhesive layer thickness. In detail, the 1-mm thick adhesive layer exerts no additional stress on the pipe, as depicted in Figure 31(a).

Furthermore, the corrosion hole size has a similar effect on maximum principal stress on liners, as shown in Figure 31(b). The stress increases before the hole reaches 50 mm, beyond which it slightly decreases. However, even though the maximum stress in the liner decreases significantly compared to the one without the adhesive layer, it continues to increase as the hole propagates. Only the liner with a 1-mm thick adhesive layer reveals a plateau in the growth.

In terms of the mechanical response of the adhesive layer, it can be observed in Figure 31(c) that, minor stress increases before the hole radius increases to 25 mm while becoming more significant until 50 mm. The 0.25-mm-thick adhesive layer shows higher stress compared to the 0.5- and 1-mm thick ones, which show similar results. With the hole size continually increasing, the stresses in 0.25- and 0.5-mm thick adhesive layers increase together, but less significantly. Only the stress in 1-mm thick adhesive layer tends to plateau. Given that the strength of epoxy resin is 275 MPa [2], the 0.25-mm thick adhesive layer will be corrupted when the hole exceeds 80 mm, and the 0.5-mm thick adhesive layer has the potential to fail if the hole is not stopped increasing. Notably, the optimal adhesive layer thickness for this straight pipe system appears to be 1 mm, as it does not create extra stress on the pipe, but also the stress on the liner drops within the ultimate strength (50 MPa), and the adhesive layer itself remains stable with increasing hole size.

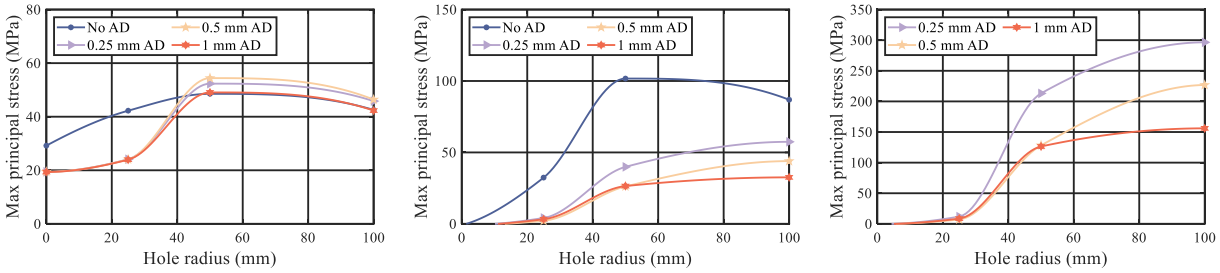


Figure 31. The maximum principal stress of straight pipe system (a) pipe, (b) liner, and (c) adhesive layer with respect to corrosion hole size. (AD = adhesive layer)

*3.2.5.2. Finite Element Analysis on Effect of Parameters on the Elbow Pipe Integrity*

*a) The Effect of Corrosion Hole Location*

The location of a corrosion hole on a cast-iron elbow pipe can vary depending on several factors including the environment, the type and extent of corrosion, and the specific conditions the pipe is exposed to. To provide a comprehensive view of the effect of corrosion hole location on an elbow pipe system, five locations around the elbow are selected, as shown in Figure 32. Five corrosion holes are located at the central midpoints of the inner and outer walls, the central midpoints at the top and bottom of the curvature, and the central top point between the straight and elbow pipe connection, respectively. Finite element analysis is carried out in analyzing a 90-degree 1.5D elbow pipe with aforementioned corrosion holes under the in-pipe pressure of 1.5 MPa. The mesh pattern and quality are important and directly determine the analytical accuracy of the elbow pipe model with perforation. The vicinity of the corrosion hole cannot be meshed with default

hexahedral elements and has to be converted to use first-order tetrahedral elements. This is suggested to be avoid in stress analysis problems, because of their poor accuracy, overly stiff behavior and slow convergence with mesh refinement [3]. Therefore, additional partition and refinement are applied in the vicinity of the hole to adopt 8-node linear hexahedral elements (C3D8R), as shown in Figure 33, which are implemented to ensure and enhance the simulation efficiency and accuracy.

The results suggest that the pipe with a corrosion hole at the central midpoint of the inner wall exhibits significantly higher tensile stress compared to others, compatible with the findings from the analysis for the intact elbow pipe system. Following this, the pipe with holes at the central top connection, central mid-top point, and central mid-bottom point of the wall show similar stress performances. The least stress concentration is observed in the pipe with corrosion at the central midpoint of the outer wall.

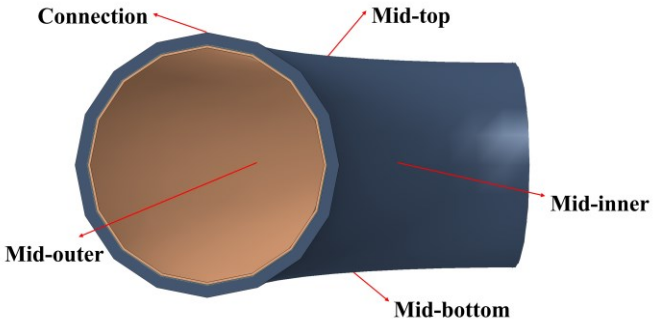


Figure 32. The locations of corrosion hole on elbow pipe.

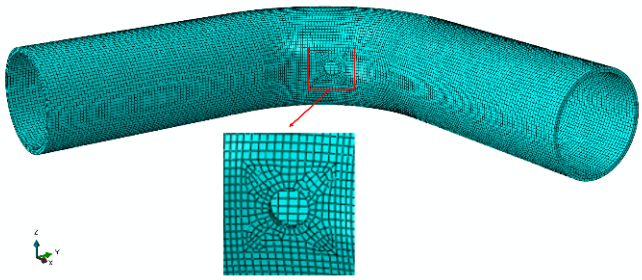

Figure 33. The finite element mesh of the elbow pipe model with corrosion hole at the inner wall.

*b) The Effect of Elbow Dimension*

To explore the effect of elbow dimension on this study, the intact elbow pipe is applied first. In this section, DN300 cast-iron elbow pipe models are created in terms of two angles of elbows (45° and 90°) and two radii of elbows (1D and 1.5D). The numerical investigation results of the stress fields in elbow pipes are shown in Figure 34. The results indicate that the elbow radius negatively affects the stress concentration on the elbow pipe, and elbow angles have negligible effects. The stress increments are 27.8% and 22.3% when decreasing the elbow radius from 1.5D to 1D in 45-degree and 90-degree elbow pipes respectively. However, the stresses remain relatively stable when switching the elbow angles. The stress concentration zone is consistently found at the inner

wall, with the stress concentration zone grows with the increasing elbow radius and angles.

In addition to assessing the effect of dimensions on the intact elbow pipe system, a 25 mm radius corrosion hole is created at the mid-inner wall, where is found to be the weakest, to explore the effect on a damaged elbow pipe system. The results, as depicted in Figure 35, present that the effect of elbow angle is not negligible anymore when the pipe is damaged and becomes negatively correlated to the maximum principal stress in the pipe. A 45-degree damaged elbow pipe exhibits higher axial tensile stress compared to a 90-degree one, and the difference increases with the elbow radius. The elbow radius is continually negatively affecting the stress concentration in the damaged pipe, with a greater effect compared to the intact pipe.

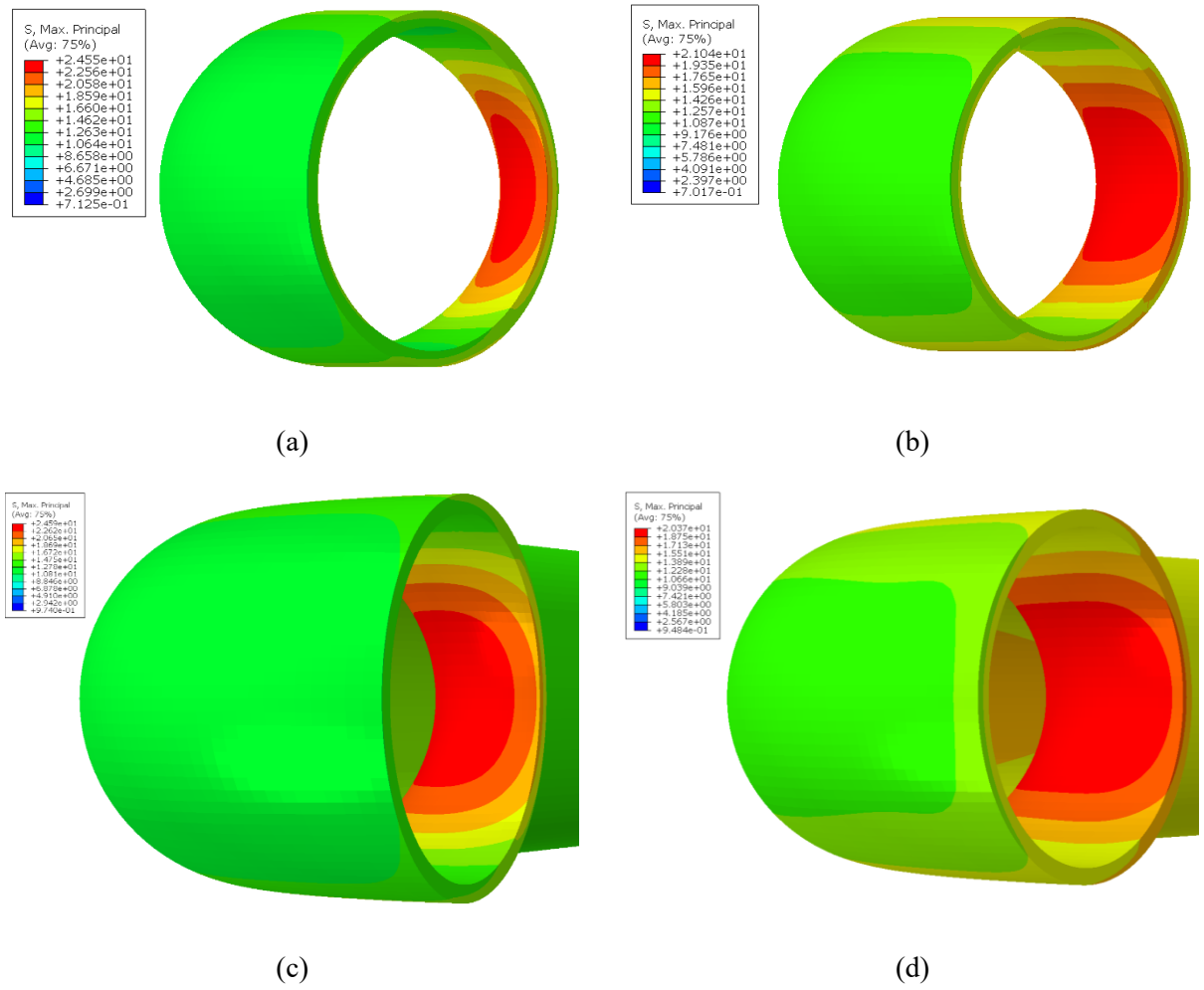


Figure 34. The distributions of maximum principal stresses on elbow pipes. (a) 45 degrees, 1D; (b) 45 degrees, 1.5D; (c) 90 degrees, 1D; (d) 90 degrees, 1.5D.

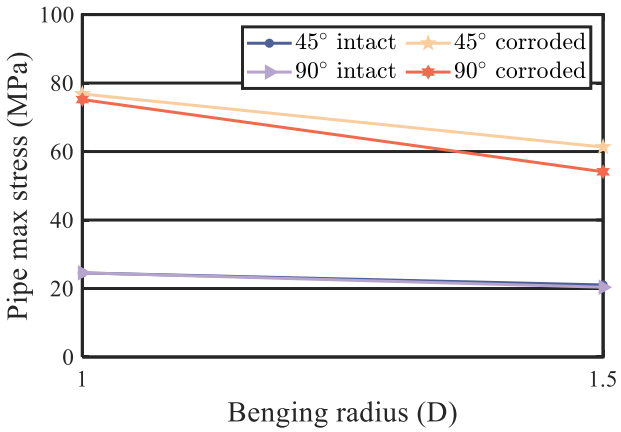


Figure 35. The effect of pipe dimensions on maximum stress of elbow pipe system.

*c) The Effect of Adhesive Layer Thickness*

The most critical location of the corrosion hole is found at the central midpoint of the inner wall, as discussed in the past section. To investigate the effect of adhesive layer thickness on the elbow pipe system, a 25-mm radius corrosion hole is selected as the imperfection on the pipe. Three layer thicknesses of 0.25, 0.5, and 1 mm are chosen, together with the reference model selected without the adhesive layer. In contrast to the maximum stress of the straight pipe with a 25 mm corrosion hole, defined as the partially deteriorated pressure pipe by ASTM F1216, which decreases with the adhesive layer thickness. The performance of the elbow pipe, as shown in Figure 36, follows a similar trend to the straight pipe with a 50 mm hole, which is identified as fully deteriorated. The maximum stress principal stresses of all three components are higher than those of straight pipes. The maximum stress of the elbow pipe is relatively stable with the consideration of the adhesive layer, and the stresses on the liner and adhesive layer pose opposite developments. The stress of the liner decreases significantly with a thicker adhesive layer at the beginning (before 0.25 mm) and tends to plateau with continuous increments. Meanwhile, the adhesive layer itself increases until 0.5 mm thick and decreases slightly when it is beyond 0.5 mm. Therefore, the optimal adhesive layer thickness is 0.5 mm in this scenario. The approach can be applied to find the optimal design of CIPP liner rehabilitation to have the best rehabilitation performance and economy.

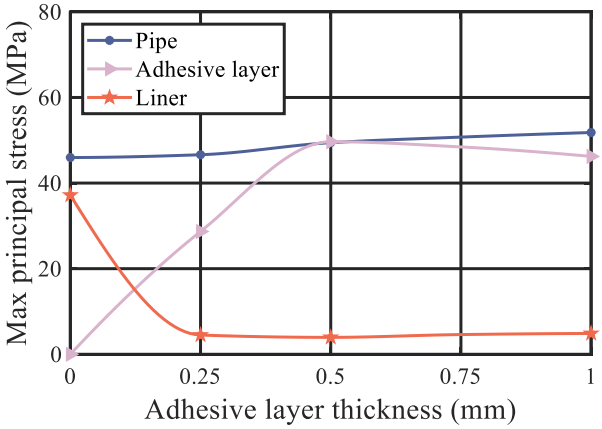


Figure 36. The mechanical performance of damaged elbow pipe system with 25-mm-radius hole with respect to adhesive layer thickness.

*3.2.5.3. Finite Element Analysis on Interfacial Debonding in Liner-Protected Pipe.*

The thermosetting resin is hardened after UV or steam curing, and serving as an adhesive layer to establish a firm bonding between host pipe and CIPP liner. The structural buckling was significantly affected by interfacial debonding between liner and pipe. Debonding is a critical phenomenon in various material systems, impacting the structural integrity and performance of composites and bonded interfaces. The process of debonding involves the separation of materials at the interface due to factors such as accumulated surface stress, interfacial friction, and relative displacements [4]. In this study, we investigate the interfacial relative displacement and stress fields between the layers to analyze the bonding performance of the pipe-liner system.

A three-dimensional (3D) finite element model is developed for the three-layer pipe-liner system in Abaqus, consisting of damaged host pipe, adhesive layer, and CIPP liner. The model is 1200 mm in length. Thicknesses of the host pipe, adhesive layer, and CIPP liner are 15 mm, 1 mm, and 3 mm respectively. The damage on the pipe is represented by a circular corrosion hole on the central top of the pipe. Hence, a semi-symmetric model is established to enhance computational efficiency. The material properties of the three components are simplified as linear elastic, as referred to in the literature [5]. There are two interfacial contact pairs in this study, the – adhesive layer interface and the adhesive layer–CIPP liner interface. The interfacial contact behaviors are governed by classical Coulomb friction law in tangential and normal directions. Penalty mode (Figure 38) is picked for tangential direction with interfacial friction coefficients from zero to one, simulating from a no bond to full bond scenarios. Normal behavior is selected as hard contact to avoid interface overlay and ensure a smooth pressure transmission through layers. Figure 37 shows the radial displacement and interfacial shear stress fields, demonstrating the bonding performance between the pipe and adhesive layer, while the adhesive layer and CIPP liner deforms integrally. High shear stress is detected around the corrosion hole area between the pipe and adhesive layer. We generate a dataset by exporting the nodal stress and displacement results of three layers at the hole area, shown in Figure 37. The dataset will be used to train the machine learning algorithms for risk assessment in Task 5.1.

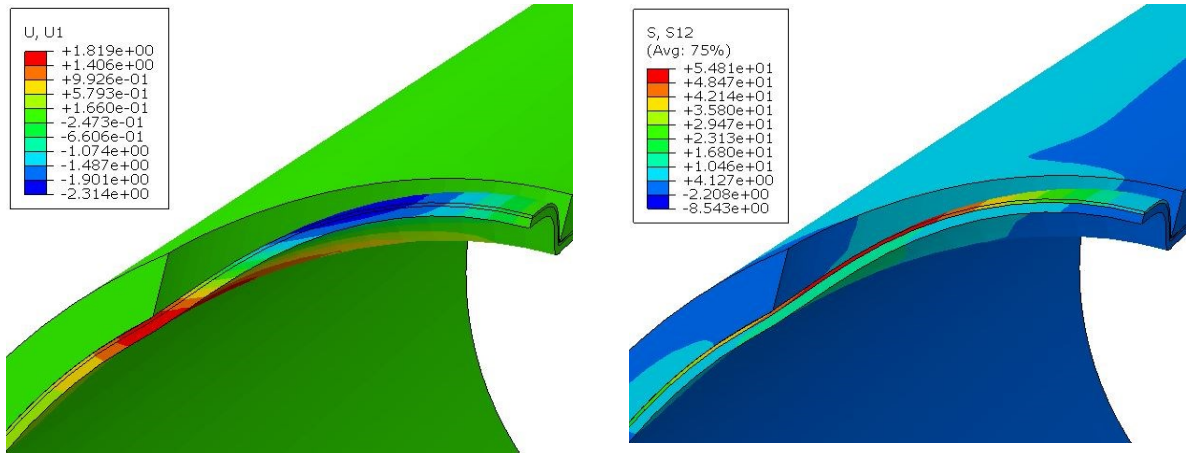


(a) (b)

Figure 37. Radial displacement (a) and shear stress (b) results on pipe-liner system.

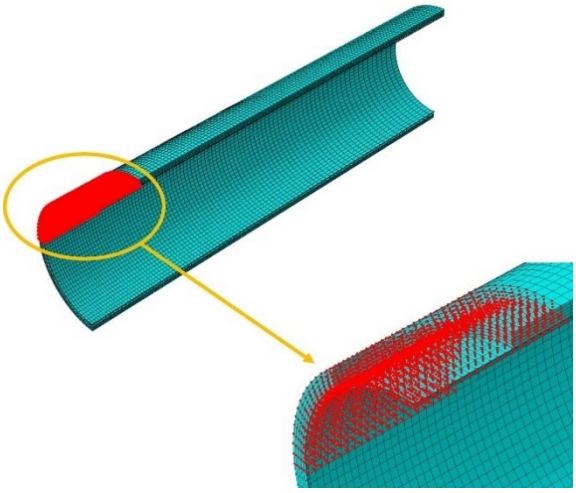

Figure 38. The locations of nodes exporting stress and displacement field results.

*3.2.5.4. Finite Element Analysis on Buckling Behavior in Liner-Protected Substrate*

The applications of computational tools present advantages in engineering areas. For example, finite element analysis in ABAQUS is recognized for its capacity to conduct large-scale simulations efficiently with minimal computational resources, allowing researchers and engineers to advanced computational resources to leverage sophisticated simulation techniques [6]. This capability is particularly beneficial in situations where intricate analyses are necessary. Furthermore, ABAQUS is renowned for its exceptional simulation capabilities in nonlinear finite element analysis (FEA) [7]. This feature is essential for accurately modeling and predicting the behavior of structures encompassing material nonlinearity and significant deformations. In this study, we utilized ABAQUS/CAE 2023 simulate the buckling behavior of a three-layer composite plate and compare the simulation results of strain distribution with the experimental results.

This section aims to simulate the buckling behavior of the three-layer composite plate along the out-of-plane direction with finite element analysis (FEA), and compare the FEA result with experimental data. An 8-node linear solid-shell element with improved surface stress visualization C3D8S, is employed to discretize the three-layer plate in ABAQUS. The C3D8S element was recommended for thin plates and has demonstrated excellent performance in buckling problems of plates with varying thicknesses and aspect ratios [8]. The material properties and dimensions of the FEA model are defined according to the experimental sample. To simplify the modeling of interfacial interactions, a single-part model is created for the composite plate and partitioned into three layers. Figure 39 shows the three-layer plate consisting of steel, adhesive layer, and liner, respectively. A uniformly global mesh size of 2.5 mm is used in the model, with finer local seeds along the out-of-plane direction to create a denser grid and enhance the numerical accuracy. Additional partitions are created on the composite plate surface, to represent two 38 × 55 mm clamped areas. The loading and boundary conditions are exactly set as the experiment. The bottom edge is clamped and the top edge is monotonically moved downwards at a constant speed of 0.2 mm/min for 7 mm displacement. The side edges are set as free-free boundary conditions.

Two-step analysis with the linear eigenvalue analysis, and nonlinear static Riks analysis is performed for buckling and post-buckling simulation. Although linear eigenvalue analysis does not take the nonlinearities into consideration, it is the fundamental approach of structural buckling analysis. This step is commonly used to extract buckling modes and generate geometric

imperfection functions [9]. In linear eigenvalue analysis, two inputs are required: the preload $P^N$ and the perturbation load pattern $Q^N$. The critical buckling load, $P^N + \lambda_i Q^N$, is typically calculated using Equation (1) [10].

$$(K_0^{NM} + \lambda_i K_\Delta^{NM})\, v_i^m = 0 \tag{1}$$

where $K_0^{NM}$ is stiffness matrix at the base state, $\lambda_i$ is eigenvalue, $K_\Delta^{NM}$ is differential initial stress and load stiffness matrix, $v_i^m$ is buckling mode shape, $NM$ are degrees of freedom $N$ and $M$ in the model, and $i$ is the buckling mode number.

In this study, $P^N$ is set to zero. Five buckling modes and buckling structural imperfections are calculated by the subspace iteration eigensolver. These imperfections are applied to simulate realistic geometric variations that may exist in actual structures in subsequent nonlinear analysis. Such analysis can leverage the results of the linear eigenvalue analysis to investigate the behavior of structures beyond the critical load, incorporating factors such as geometric nonlinearity and material behavior [11]. Buckling is one of the geometrically nonlinear problems, in which the structure releases energy to remain in equilibrium. The Riks method is selected as the nonlinear analysis approach, for its advancement in finding static equilibrium state during buckling [12]. In ABAQUS, a modified arc length control Riks method is used, which determines the equilibrium state by scaling the applied load to the load proportionality factor (LPF) using an auxiliary constraint function [13]. To compute the LPF, we defined an initial arc length increment, $\Delta l_{in}$, and estimate total arc length, $l_{period}$. Then the initial LPF, $\Delta\lambda_{in}$ , can be calculated with Equation (2) [10]. The subsequent LPF is automatically computed at each increment with respect to arc length until convergence is achieved.

$$\Delta\lambda_{in} = \frac{\Delta l_{in}}{l_{period}} \tag{2}$$

where $\Delta\lambda_{in}$ is initial LPF, $\Delta l_{in}$ is initial arc length increment, and $l_{period}$ is estimate total arc length.

We input the first three bucking modes with the combinations of imperfections into nonlinear static, Riks analysis. The magnitude of the initial imperfection of the plate is assumed to be 1% of the plate thickness as the base state. Subsequently, for the second and third buckling modes, the imperfections are reduced to half of the previous magnitudes, respectively. Following the analysis, the strain field results obtained from nonlinear analysis are processed and presented in the discussions.

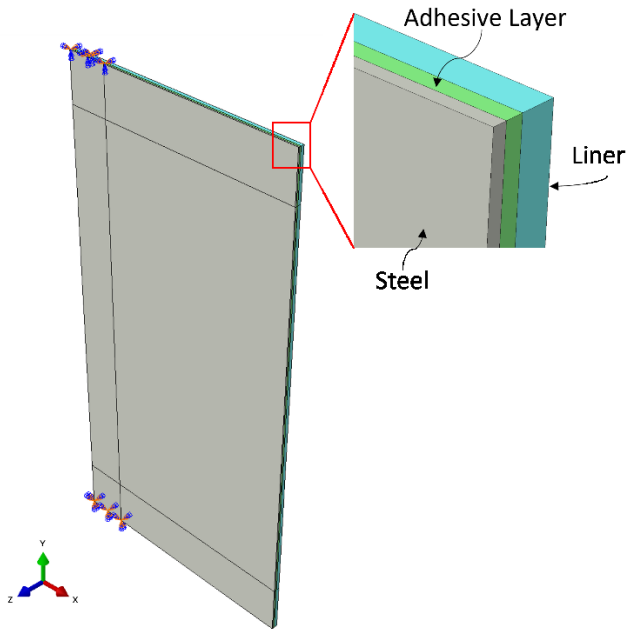


Figure 39. The finite element model of the three-layer composite plate.

The out-of-plane strain distribution contours obtained from distributed fiber optic sensors and FEA are compared at the vertical displacement of 7 mm as shown in Figure 40. Maximum strain occurs at the center of the left boundary of the plate which is about 12071.5 $\mu\varepsilon$ from FEA, compared to the 13220.6 $\mu\varepsilon$ from experiment. The difference of the maximum strain is about 8.69%. It can be observed that the strain distribution fields from FEA aligns well with the distribution generated by the distributed fiber optic sensors, indicating the accuracy of the FEA simulation. However, some discrepancies are also detected. The numerical results exhibit a symmetric pattern, whereas the experimental results are not perfectly symmetric due to variations in the experimental setup. Additionally, FEA captures less negative strain near the clamped areas and slightly larger high strain areas at the center on the left edge of the plate compared to the experimental results.

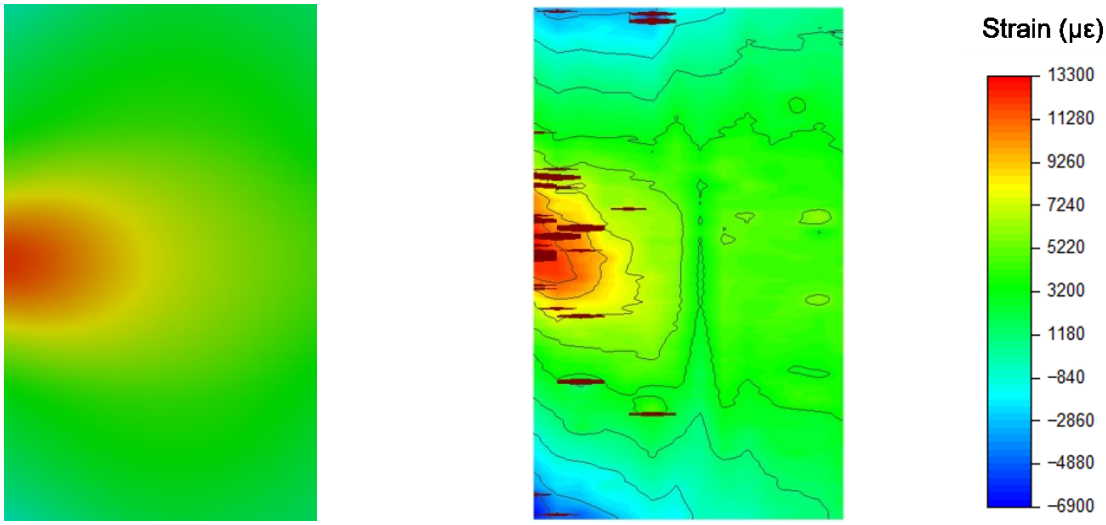


(a) (b)

Figure 40. Strain comparison of FEA and experimental results at 7 mm vertical displacement (a) FEA result, (b) experimental results.

*3.2.5.5 Micro-Scale Modeling of Nano-Reinforced Epoxy Material System*

have conducted multi-scale simulation for pipeline integrity management, this report focuses on simulating the influence of fiber parameters on the strength of the fiber-reinforced adhesive layer, with the results outlined below:

The Representative Volume Element (RVE) analysis and FEA were employed to investigate the various parameter effects on fiber omposite, including fiber orientation (0° to 90°) and fiber volume friction (fvf) (0.5% to 9.5%). The findings are presented below:

*a) Effect of Fiber Orientation:*

The fiber orientation analysis revealed that the orientation of fibers relative to the loading direction significantly influences composite strength. The FEA in Figure 41 showed anisotropic and isotropic strength differences across orientations ranging from 0° to 90°. The maximum strength was observed when fibers were aligned parallel to the loading direction. A significant drop in strength occurred at approximately 18 degrees in anisotropic material. Isotropic material demonstrates a consistent even strength distribution across different orientations.

*b) Effect of Fiber Volume Fraction (fvf):*

fvf, a crucial factor in fiber composites, was adjusted by varying the fiber radius while keeping the number of fibers constant. Results shown in Figure 41(d) and (e) offer a detailed analysis of the relationship between composite strength and fvf.

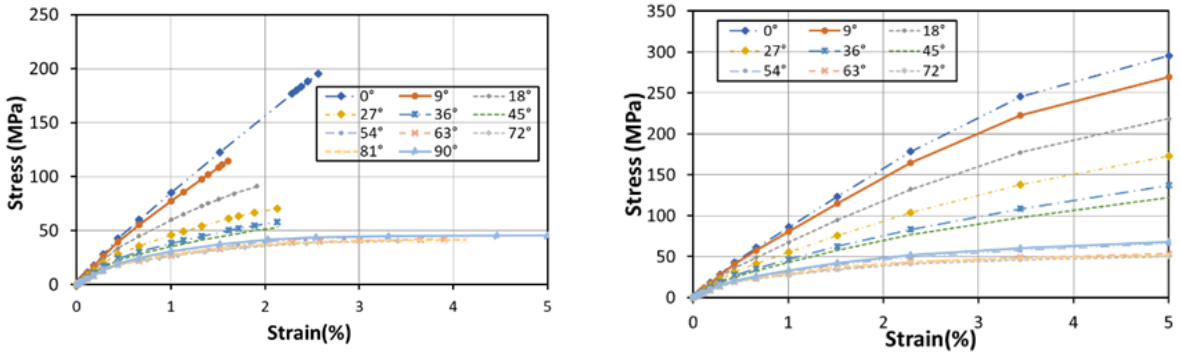


(a) (b)

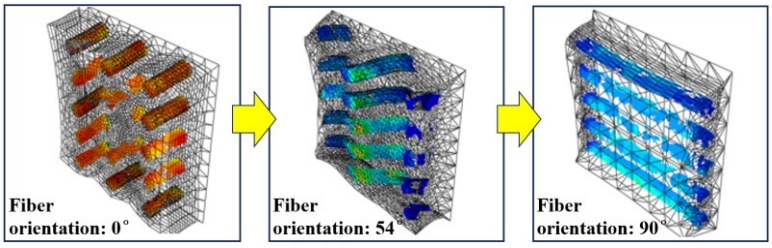


(c)

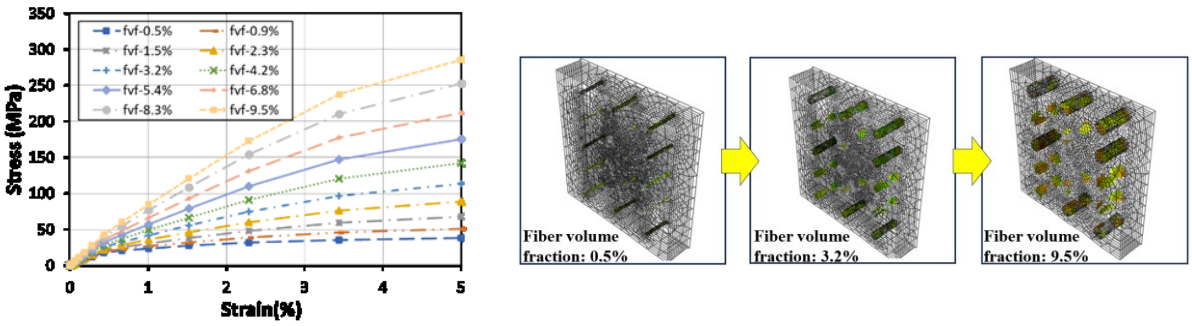


(d) (e)

Figure 41. Stress-strain curve of fiber composite with fiber orientation viable. (a) in anisotropic material; (b) in isotropic material; (c) FEA model visualization. (d) Stress-strain curve of fiber composite single parameter study with fiber volume fraction variable, and (e) FEA model visualization

We also create Representative Volume Element (RVE) model in finite element analysis (FEA) with Abaqus 3D SIMULIA for nano-reinforced epoxy system. The RVE analyses of nanofiber-reinforced epoxy are conducted from 0% to 2% weight fraction respectively.

There are three types of nanofibers in the composite materials FEA: 1) 0D nanodiamonds (ND), 2) 1D multiwall carbon nanotubes (MWNT), and 3) 2D graphene nanoplatelets (GNP). The material properties for NDs, MWNTs, and GNPs are obtained from references and materials providers, and these properties are implemented in the simulation. The ND RVE model, shown in Figure 42, illustrates a comparison between the global and local scales in square and hexagonal arrays. Figure 43 illustrates the RVE model of unidirectional CNT, highlighting the FEA model fiber arrangement. The model of the RVE with aligned and oriented GNPs is illustrated in Figure 44. This model showcases the arrangement and distribution of GNPs within the matrix.

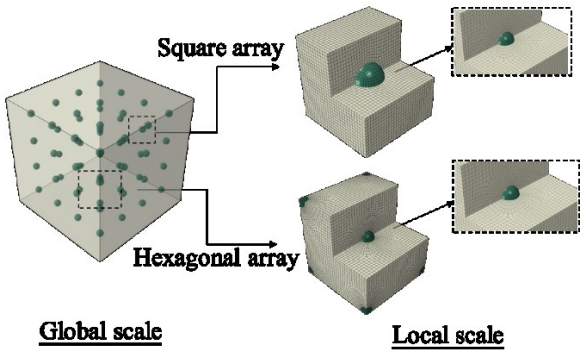


Figure 42. Visual illustration of RVE of square or hexagonal array packing from nanodiamond multicell fiber composite.

(a) (b)

Figure 43: A representative example of a unit cell model with aligned CNT for a 2.0% weight fraction. (a) the front view, (b) the isometric view.

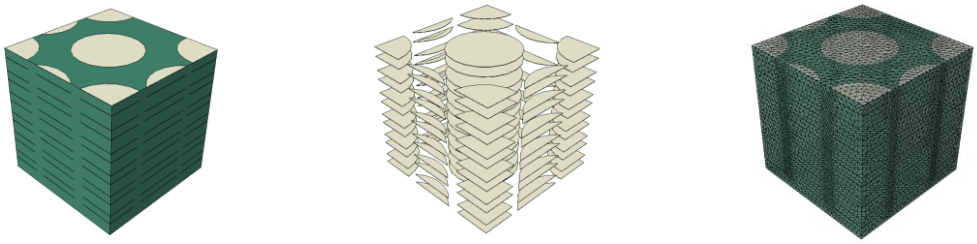

(a) (b) (c)

Figure 44: A representative example of an RVE with aligned GNPs for a 2.0% weight fraction. (a) the entire RVE, (b) the distribution of platelets, and (c) the meshing geometry.

The stress-strain results from various RVE models are analyzed to understand the impact of different weight fractions of additives on the ultimate stress of composites, as shown in Figure 45. For the ND additive in Figure 45(a), varying weight fractions from 0.5% to 2.0% showed minimal impact on the plastic region and ultimate strength, with a slight increase to around 35 MPa at 2.0% ND. A similar trend in Figure 45(b) is observed in the 90° orientation for MWNT composites, where varying weight percentages (0.5%, 1%, and 2%) indicate that the material's strength remains unchanged in the 0° loading direction, demonstrating non-isostrain conditions. For GNP composites, under axial loading, the stress remains consistent with increasing GNP weight fractions, while radial simulations show enhanced ultimate stress with increasing weight fractions, illustrated in Figure 45(c). Further analysis of ultimate strength outcomes for each type of nanoparticle in Figure 46 reveals that for ND composites, a slight increase in strength (0.3 MPa) is observed from 0% to 0.5% ND, peaking at 36 MPa with a 2% ND weight fraction. For MWNT composites, the strongest orientation is observed at 0 degrees, indicating that fiber orientation plays a crucial role. In contrast, GNP composites under radial loading show stress peaks at 41.5 MPa with 0.5% GNP, reaching 44.3 MPa at 1%, and 50.3 MPa at 2%. This trend aligns with other studies showing increased ultimate stress with higher weight fractions of aligned graphene oxide due to optimal load transfer through the shear lag mechanism [14]. These findings highlight the significant impact of nanoparticle geometry and orientation on the mechanical properties of

composite materials

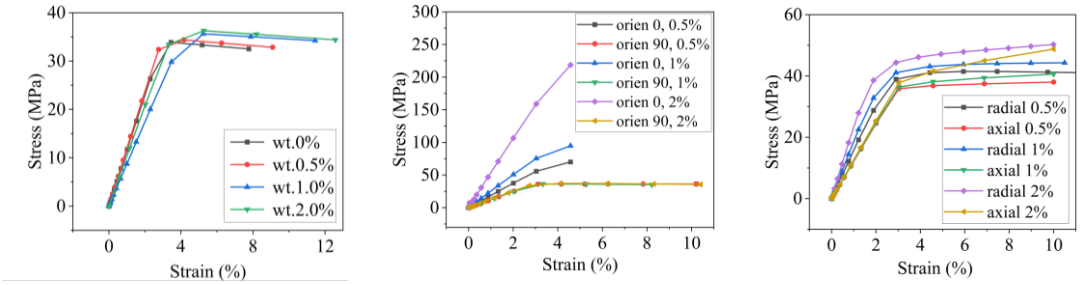


(a) (b) (c)

Figure 45. The stress-strain curve predicted by the simulations under uniaxial tensile loading (a) ND (b) CNT, and (c) GNP.

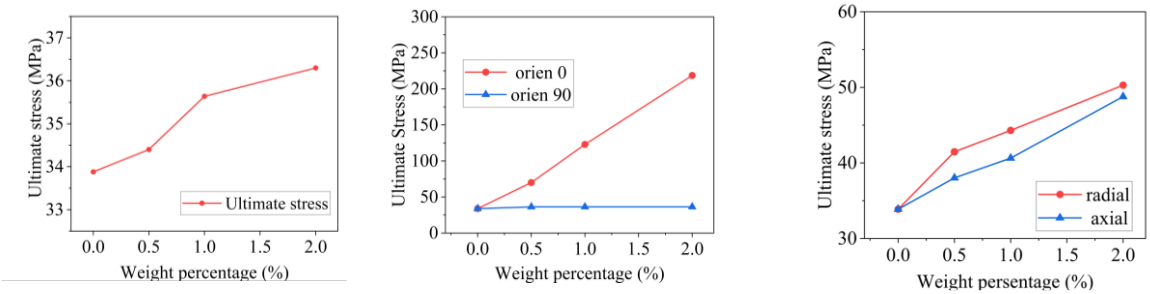


(a) (b) (c)

Figure 46. The ultimate strength of composite with different weight fractions, composite reinforced by (a) ND (b) CNT, and (c) GNP.

### 3.3. (Task 4) Enabling Self-Sensing for The Developed CIPP Structural Liner

#### 3.3.1. (Task 4.1) Development of Embedded Distributed Fiber Optic Sensors for Self-Sensing Structural Liner

This study aims to develop a smart-liner system for energy transport and storage infrastructures. The proposed liner incorporates distributed fiber optic sensors (DFOS) to monitor strain variations along its length, which are critical for assessing the liner's condition during two key phases: 1) the adhesive layer's curing phase, and 2) its operational phase when subjected to mechanical deformations and damage.

Strain data recorded during curing provide insights into the adhesive's curing dynamics and help identify potential vulnerabilities caused by residual strains. In the operational phase, strains caused by external forces can be analyzed to detect mechanical deformations. DFOS strain distribution data can also be used for reverse analysis to determine the deformed shape of the liner. Additionally, computer vision techniques generate 3D point clouds to evaluate structural deformations and validate the system's effectiveness. A novel aspect of this research is the use of sharp peak strain distributions in sensor signals to pinpoint, track, and visualize damage caused by mechanical stresses.

*a) Compatibility of the Smart Sensor-Liner System:*

To evaluate the compatibility between the sensor and liner, distributed optic fiber sensors were integrated into a commercial liner. The optic fiber sensors demonstrated strong adherence to the liner, as evidenced in Figure 47 (a), where the sensors remained firmly attached to the liner even under significant deformation. After that, the liner equipped with sensors was applied to a steel substrate using epoxy adhesive (Figure 47 (b)).

In this study, the epoxy adhesive layer of the liner system was synthesized using a commercially available epoxy resin and curing agent. The liner was constructed from seamless woven polyester yarn fabric with a polyurethane/polyethylene (PU/PE) coating. This inner liner is designed to bond to a steel substrate using epoxy as the adhesive layer. The distributed fiber optic sensor (DFOS) was first attached to the inner surface of the liner with adhesive. After allowing 24 hours for the adhesive to cure, the smart liner was ready for integration into the system. The DFOS exhibited strong adhesion to the liner, remaining securely attached even under significant mechanical deformation. The sensor-equipped liner was then adhered to a steel substrate using the epoxy adhesive, resulting in the prepared sample, as shown in Figure 48.

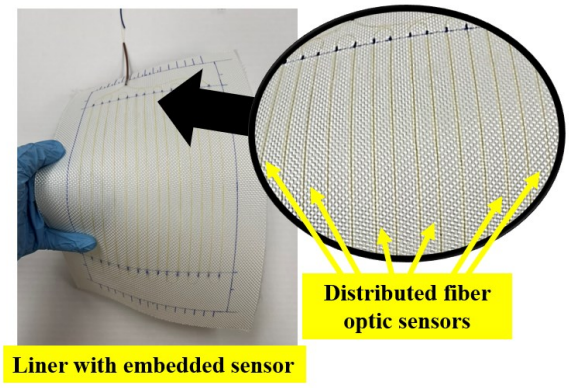


Figure 47. (a) Smart sensor-liner system. For experimental simplicity, a 6 x 12” steel panel was utilized to examine the sensor-liner system.

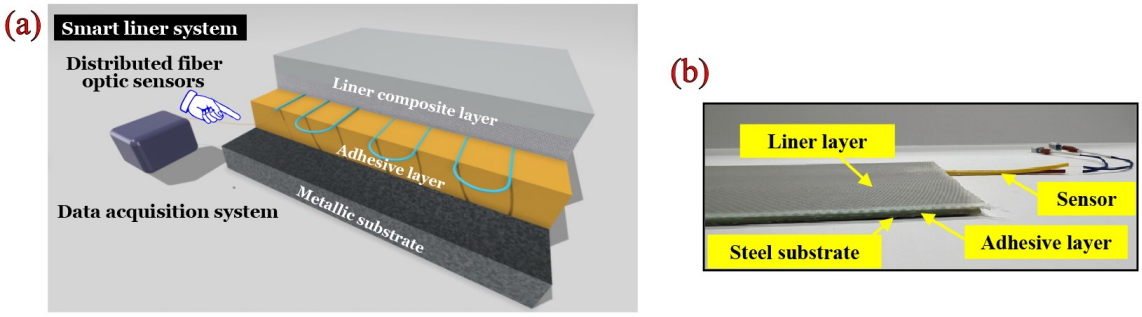


Figure 48. (a) Smart sensor-liner system, (b) sensor-liner system applied to flat steel substrate.

*b) Visualization of Strain Distribution*

Accurate mapping of strain signals to the corresponding sensing area relies on precise coordinates, as shown in Figure 49. The strain signals collected along the fiber length were organized into

distinct paths using coordinates to ensure accurate localization. The X-axis runs parallel to the sensor paths, while the Y-axis is perpendicular. To accommodate the sample's geometry, the strain data was divided into 14 distinct paths. The sensor in this study covered a measurement area of 20 cm along the X-axis and 13 cm along the Y-axis.

In distributed sensor applications, besides the length of the sensor paths, two critical parameters impact system resolution and accuracy: 1) the spacing between sensor paths, and 2) the spatial resolution. For this study, strain data was collected from 14 sensor paths with 1 cm spacing and a spatial resolution of 0.65 mm along each path, as shown in Figure 49(b). The spacing between sensor paths, indicated by blue arrows, refers to the fixed distance between adjacent paths, set during sensor installation. Spatial resolution, represented by black arrows, refers to the interval between measurement points along the sensor fiber and can be adjusted during data collection and processing.

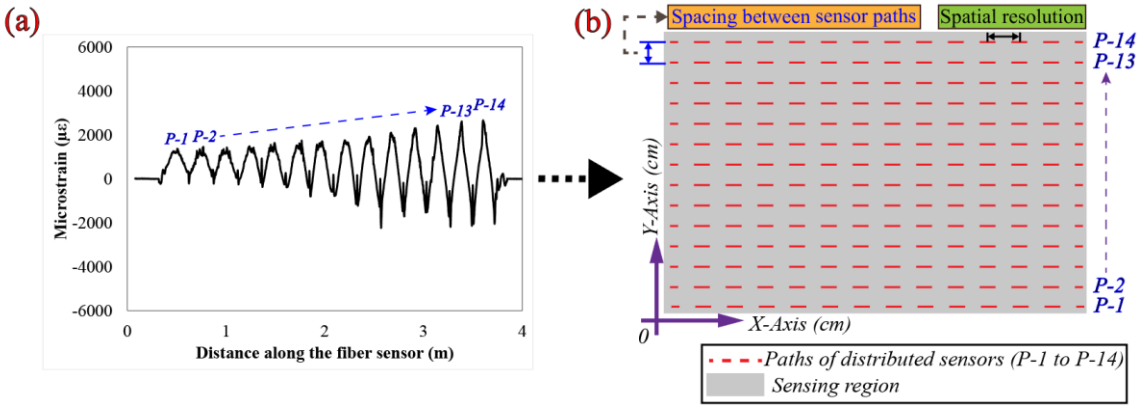


Figure 49. (a) obtained strain results along the fiber length, and (b) separation of obtained strain results into 14 paths.

*c) Investigation on Curing Process of Adhesive Layer by Using Smart Sensor-Liner System:*

The strain signals were collected over 5600 minutes, and the collected data includes every 0.65mm spot, the collected results was used to assist with understanding the curing kinetics of the adhesive layer. Additionally, both 2-D and 3-D plots visualizations were crafted for investigating the curing-induced strain effects on the liner system. Figures 50 (a) and (b) highlight the presence of non-uniform strain distribution across the liner, and the concentrated strain possibly attributed to the liner's geometry or the intrinsic material characteristics. A cross-sectional viewpoint along a single axis of the liner, at path 9, is depicted in Figure 50 (c), and Figures 50 (d) to (f) showcase the evolution of strain over the curing period at critical points identified in Figure 50 (c). Furthermore, Figure 50 (g) provides a visual depiction of the smart sensor-liner system, offering insights into the structure of the specimen under investigation.

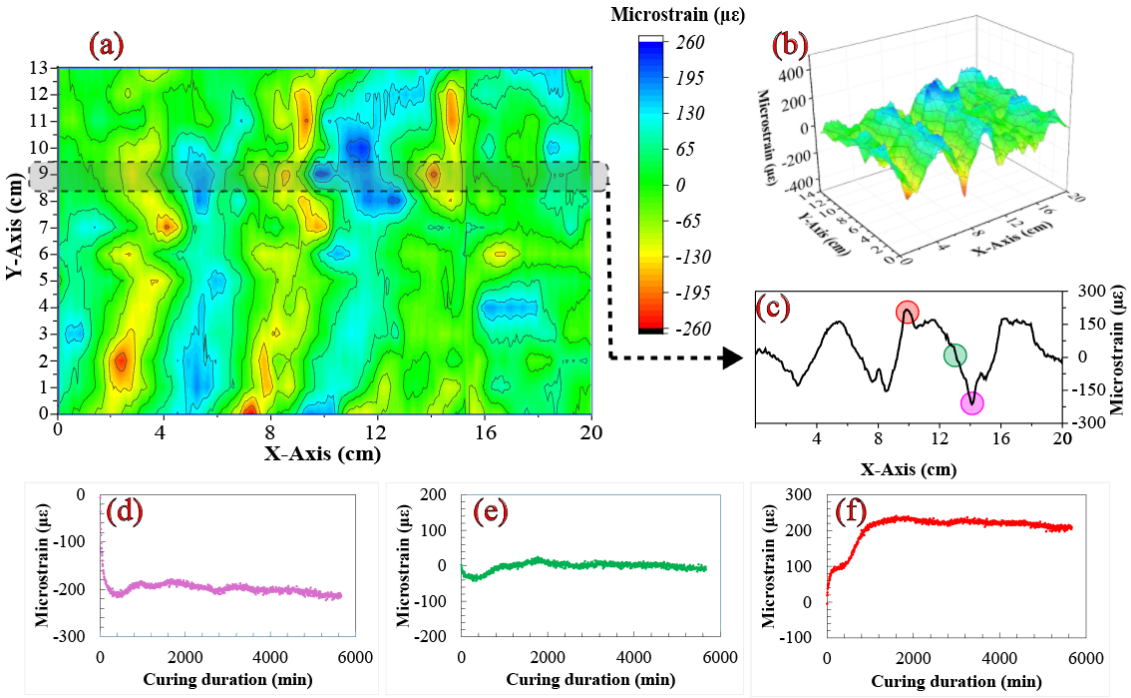


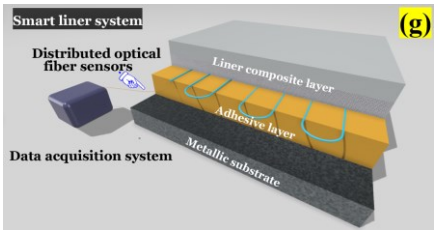


Figure 50. (a) (b) 2-D and 3-D plots of curing strain on liner surface, (c) cross-section of the curing strain at path 9, (d)-(f) curing strain along with the curing duration at selected spots, and (g) illustration of the sample with smart liner system.

*d) Curing Kinetics Investigation for Adhesive Layer:*

The detection of non-uniform strain distribution across the liner suggests intricate patterns of strain evolution during the curing of the adhesive, potentially influenced by a variety of factors related to liner's geometric or material. To gain further insight into these curing strain dynamics, a sensor layer was positioned on the steel surface, as illustrated in Figure 51. A comparison of the strain data between the liner and steel reveals a pronounced difference in behavior, with the steel exhibiting a more consistent and less variable response to the curing process. This indicates that steel, unlike the liner material, does not undergo significant deformation transformation during curing.

*e) Curing Stage Investigation for Adhesive Layer:*

Furthermore, the analysis of curing-induced strain signals within the smart liner system facilitates the monitoring of polymeric materials' curing stages. This is crucial for assessing the polymer's performance and determining when the liner is ready for service. Figure 51 (g) isolates three spots on the liner system that reflect varied final strain values after the curing process, characterized by positive (red line), negative (purple line), and near-zero (green line) strains. Additionally, a reference spot on the steel surface (black line) is selected. The curing process is segmented into three distinct phases: Phase I (liquid phase), Phase II (gelation phase), and Phase III (vitrification phase), and results showing that the smart liner system is capable of autonomously indicating when

the adhesive reaches each of these curing stages.

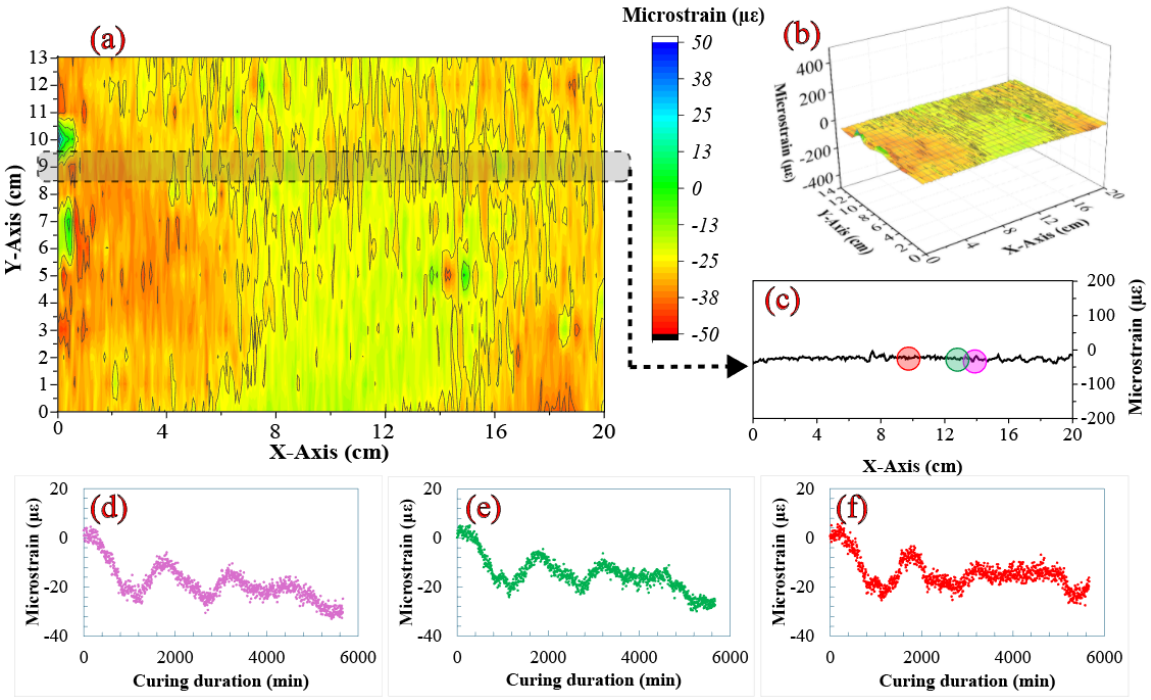


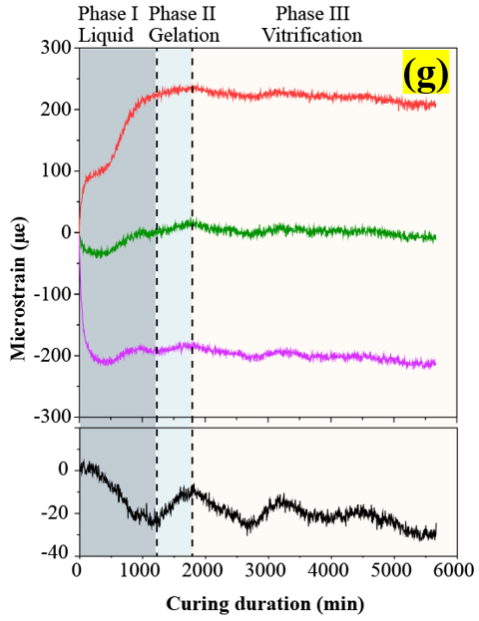


Figure 51. (a)-(f) curing strain on steel substrate, and (g) curing stage of the adhesive layer that identified by curing strain results, which obtained by smart liner system.

### 3.3.2. (Task 4.2) Investigating the load transfer between layers of the CIPP liner and the cast-iron substrate

An experimental study was conducted to integrate distributed fiber optic sensors (DFOS) into the CIPP liner system and investigate the conversion of strain signals into deflection measurements as the liner system undergoes deformation, such as buckling. Additionally, digital-twin models of the

specimen were created at various stages of the test to illustrate the progression of shape changes throughout the experiment.

*a) Specimen and Test Setup for Mechanical Deformation*

Buckling deformation was induced in the smart-liner-protected sample, which was subjected to mechanical loading within a load frame to simulate buckling conditions. As shown in Figure 52(a), eccentric compressive forces were applied to the specimen via the load frame until buckling deformation occurred. The displacement magnitude was measured and controlled by the load frame, with the tests conducted in displacement-control mode at a rate of 0.2 mm/min. Buckling deformation became visible at a total displacement of 7 mm. Additionally, a depth camera, positioned 0.8 meters from the specimen, captured shape changes during the test. Figures 52(b) and 5(c) display the front and back views of the specimen, both before and after buckling, providing a clear visual comparison of the deformation.

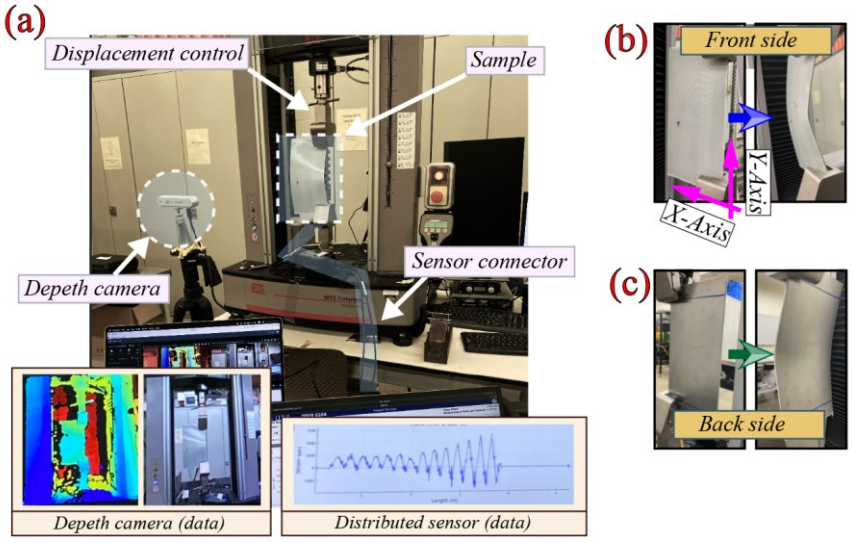


Figure 52. (a) The sample equipped with smart sensor-liner system undergoing buckling deformation. The (b) front side and (c) back side of specimen under buckling deformation.

*b) Mechanical Deformation Detection and Shape Reconstruction via Sensor-Liner System:*

The smart sensor-liner system, integrated with fiber optic sensors, is designed to detect, visualize and quantify mechanical deformations. A sample with this system was subjected to buckling load, and strain data was captured by sensors arranged in 14 lines, each 1 cm apart. The obtained data was used in a polynomial fitting mathematical model, helped visualize the deformation. Increasing the polynomial fitting surface's order (both in X and Y dimensions) effectively represented the spatial distribution and magnitude of the strain on the buckled plate. The model's accuracy in depicting strain distribution was enhanced by adjusting the polynomial fitting orders, as detailed in Figure 53(f).

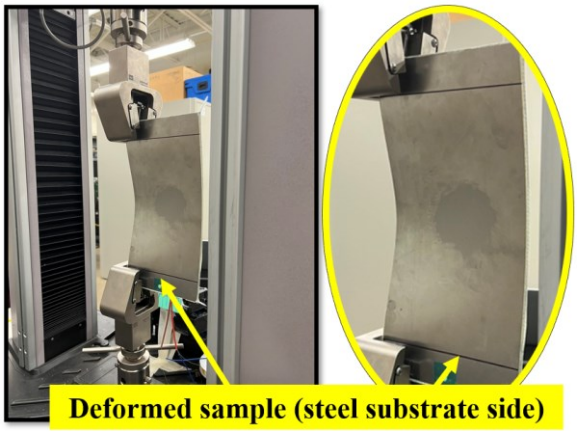


(a)

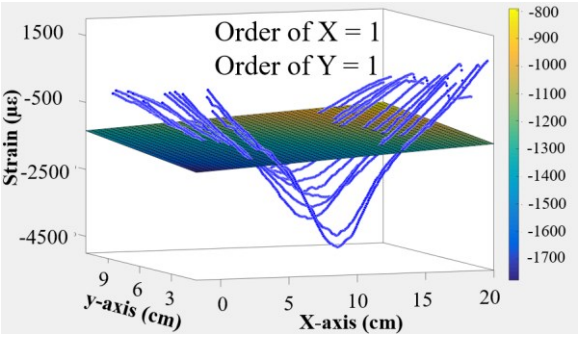


(b)

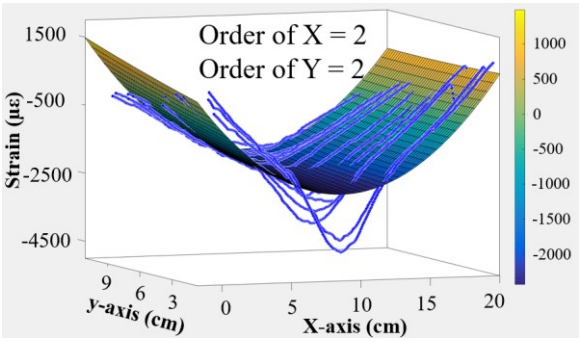


(c)

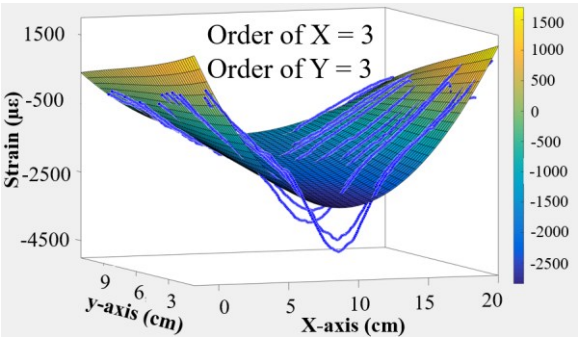


(d)

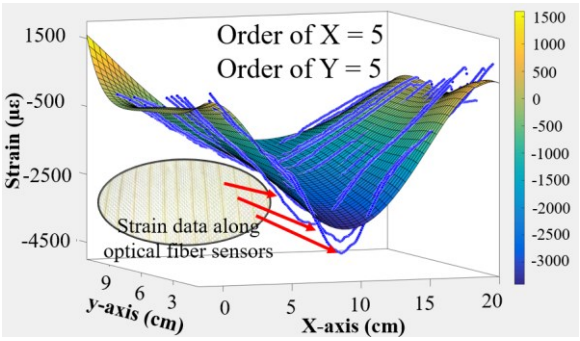


(e)

R-square of the polynomial ftting

| x \ y | 1 | 2 | 3 | 4 | 5 |
|---|---|---|---|---|---|
| 1 | 3.9% | 3.7% | 3.6% | 4.2% | 4.4% |
| 2 | 96.6% | 99.0% | 99.0% | 99.5% | 99.2% |
| 3 | 99.5% | 99.0% | 99.4% | 99.4% | 99.2% |
| 4 | 99.6% | 99.6% | 99.6% | 99.6% | 99.5% |
| 5 | 93.4% | 93.6% | 99.6% | 99.5% | 99.5% |

(f)

Figure 53. (a) A sample equipped with smart sensor-liner system undergoing buckling deformation. (b) to (e) Utilization of polynomial fitting to reconstruct the deformation, based on data from the smart sensor-liner system. (f) Sensitivity analysis of the polynomial fitting process.

*c) Strain Validation with FEA Simulations:*

The out-of-plane strain distribution contours obtained from distributed fiber optic sensors and FEA are compared in Fig. 13. The strain patterns and magnitudes recorded by the sensors are highly matched to the prediction by FEA, underscoring the optic sensors' efficacy in monitoring surface strain changes, thereby affirming the smart-liner's utility. Additionally, in Figure 54 (g), when the displacement was at 7mm, the maximum strain that occurred at the center of the left boundary of the plate was about 12071 με from FEA, yielding a similarity of about 91% compared to the experiment.

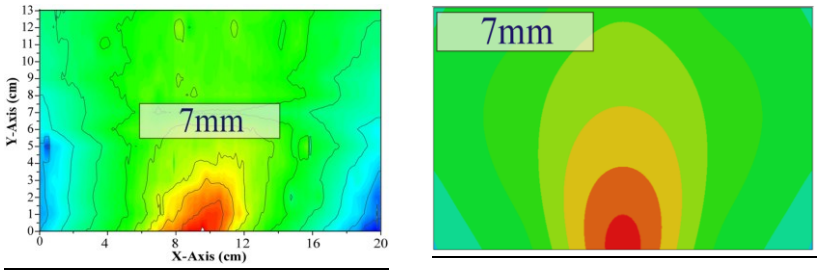


Figure 54. Strain on the smart-liner protected specimen, derived from (a) sensor data and (b) FEA model predictions.

*d) Investigation on Strain-Deformation Models and Creation of Digital Twin Models Using Smart Sensor-Liner System:*

The deformation of the smart-liner protected specimen was reconstructed using the developed analysis method. This reconstructed shape was then processed with the point cloud data generated by the computer vision system, and a selected showcase is illustrated in Figure 55. The red dots depict the shape of the buckled plate as determined by the proposed method, while the blue dots represent the point cloud data derived from computer vision. Overall, there is a commendable alignment between the reconstructed shape and the measured deformation, indicating the accuracy of the reconstruction method. The performance metrics used to quantify the accuracy of this reconstruction showed a coefficient of determination (R2) with a value of 0.995; therefore, the results demonstrated the high precision of the proposed shape reconstruction technique. After that, the deformation progress of the specimen was utilized to generate digital twin-based models, which is illustrated in Figure 56. The inclusion of displacement is crucial, as it progressively increases throughout the duration of the experiment, providing a direct correlation between the physical deformation of the smart-liner and its virtual representation. This sequence of virtual models showcases the dynamic nature of the digital twin concept, and also underscores the smart-liner system's advanced ability to track and visualize the evolution of a physical asset in real-time.

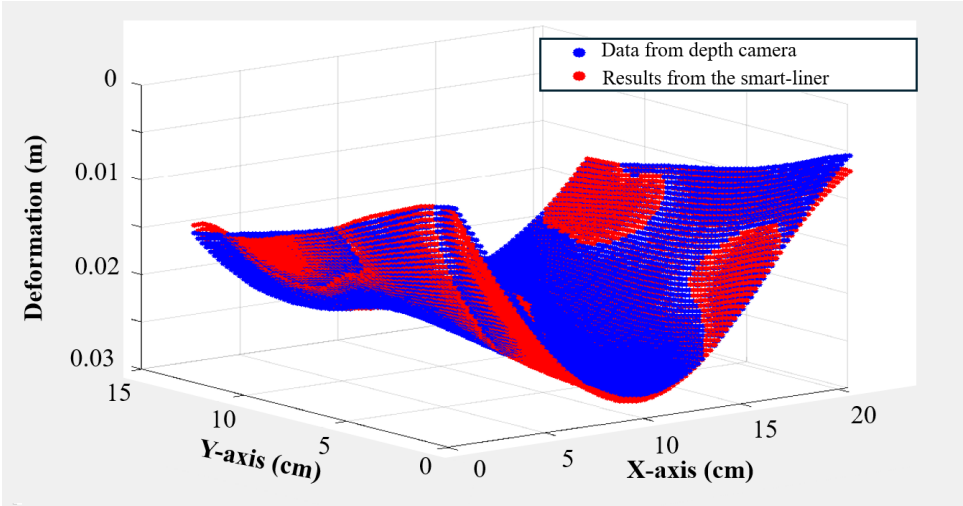


Figure 55. Deformation of the liner-protected plate specimen obtained from shape reconstruction and computer vision.

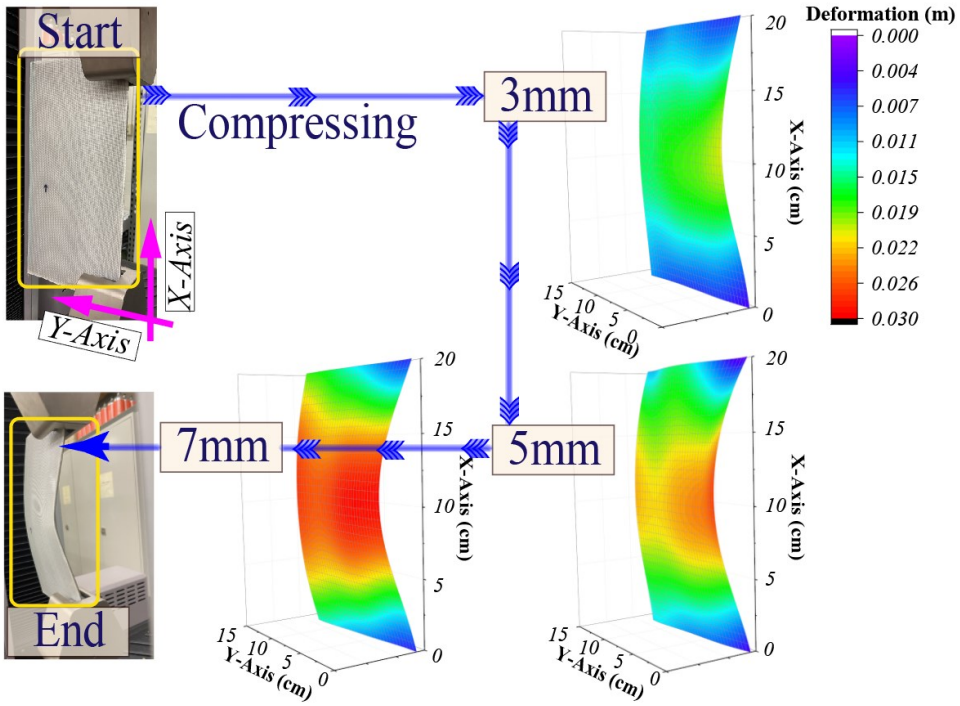


Figure 56. Creation of 3-D digital twin-based virtual models for specimen under buckling deformation as the displacement applied increased up to 7 mm.

*e) Localization of Internal Damages:*

A novel aspect of this research is the use of sharp peak strain distributions in sensor signals, which are essential for pinpointing, tracking, and visualizing damage generated when the

specimen is subjected to mechanical stress. In Figure 57(a), the results from path 10 serve as a representative case, displaying strain signals collected under varying mechanical deformations ranging from 0.5 mm to 7 mm. The appearance of peaks along the strain distribution curve identifies potential defect locations within the liner. These peaks are categorized by path number and a unique identifier for each failure location, such as P10-F1, P10-F2, and P10-F3.

At minor deformations (0.5 mm to 1 mm), the distributed fiber optic sensor (DFOS) readings showed a uniform pattern without pronounced peaks, indicating that no defects had yet occurred. However, as deformation increased, the peaks at P10-F1, P10-F2, and P10-F3 began to rise sharply, indicating the presence of defects and their progressive worsening. The increasing magnitude of these peaks correlates with the expansion of the defected areas, signifying that deformations become more pronounced at higher strains.

To confirm that areas showing sharp peak strains after mechanical deformation correspond to defects in the liner system, particularly in the adhesive layer, micro-CT images were taken post-experiment. Figure 58(a) shows a cross-sectional view of the liner system, highlighting the interface between the liner surface and adhesive layer, with distributed sensors spaced 10 mm apart. Voids were found throughout the scanned surface, particularly at the adhesive-liner interface. Figure 58(b) reveals a crack developed transversely to the sensor fiber in the sensing area, detected by a sharp peak in the strain signals. Figure 58(c) illustrates a void adjacent to the sensor, which also resulted in a sharp peak in the sensor signal.

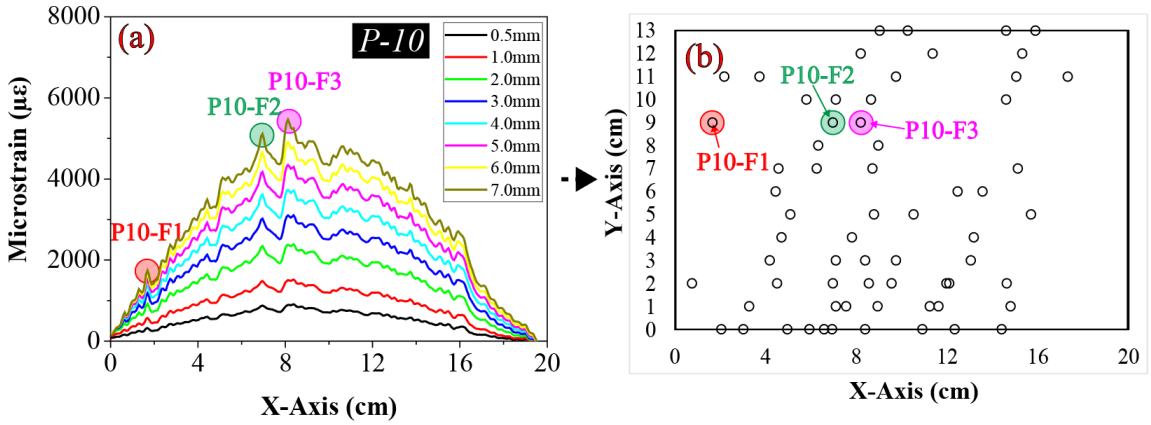


Figure 57. (a) Strain distributions measured from path 10 (P-10), and (b) 2-D digital twin of failures under mechanical deformation.

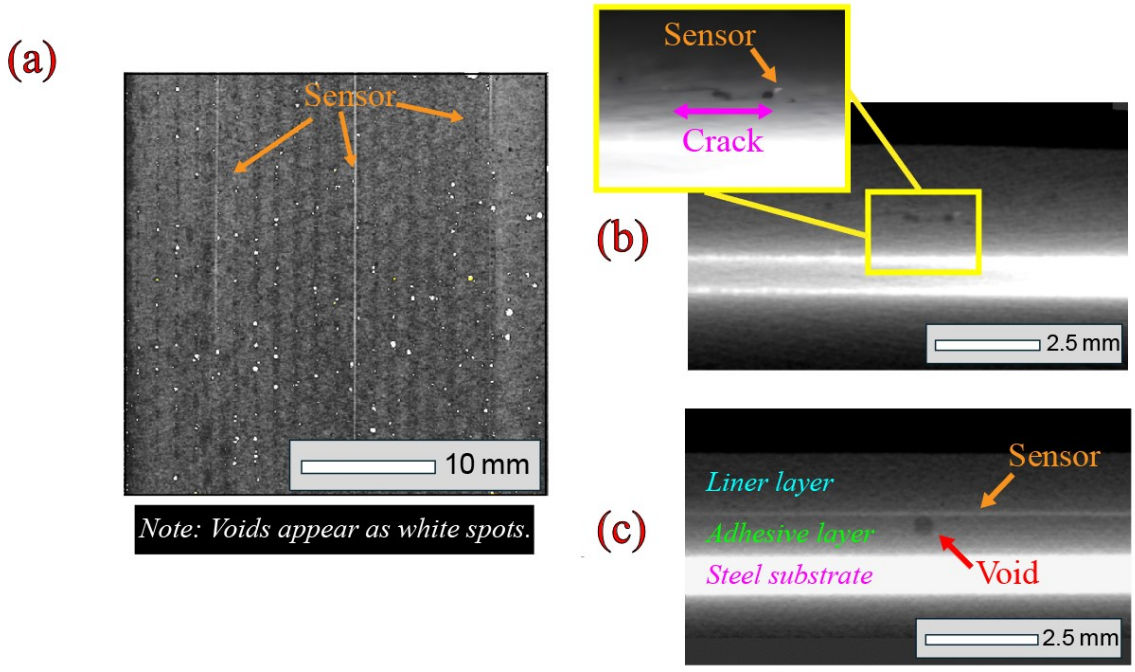


Figure 58. Micro-CT cross-sectional images of the (a) topography of the liner system, location of (b) crack, and (c) voids detected by distributed sensor.

*f) Identifying High-Risk Areas for Damage Formation:*

Areas exhibiting negative curing-induced strain, along with voids and significant deformation, are identified as particularly susceptible to cracking, debonding, and delamination failures in the liner system. Thus, curing-induced strain serves as a marker for regions at higher risk of these types of failures. Figure 59 illustrates the relationship between curing-induced strain on the liner surface and the positioning of defects. Figures 59(a) and 20(b) show the strain distribution along path 13 (P-13) under 7 mm deformation and after the curing process, respectively. It becomes clear that areas with negative strain post-curing are directly linked to defect formation. These zones, marked by concentrated internal stresses and sharp strain peaks, exhibit weakened mechanical properties. The circles represent identified internal damages, while the pink areas highlight regions exhibiting negative strain after the curing process.

In conclusion, the identification of negative curing-induced strain serves as a critical indicator of potential failure points within the liner system. These findings underscore the importance of monitoring strain distribution during both the curing process and subsequent mechanical loading to predict and mitigate structural failures. By pinpointing areas with concentrated internal stresses and strain peaks, engineers can take proactive measures to reinforce or repair vulnerable sections, thus enhancing the durability and longevity of the liner system. This approach not only improves the overall performance of the system but also provides a valuable tool for early detection and prevention of serious damage.

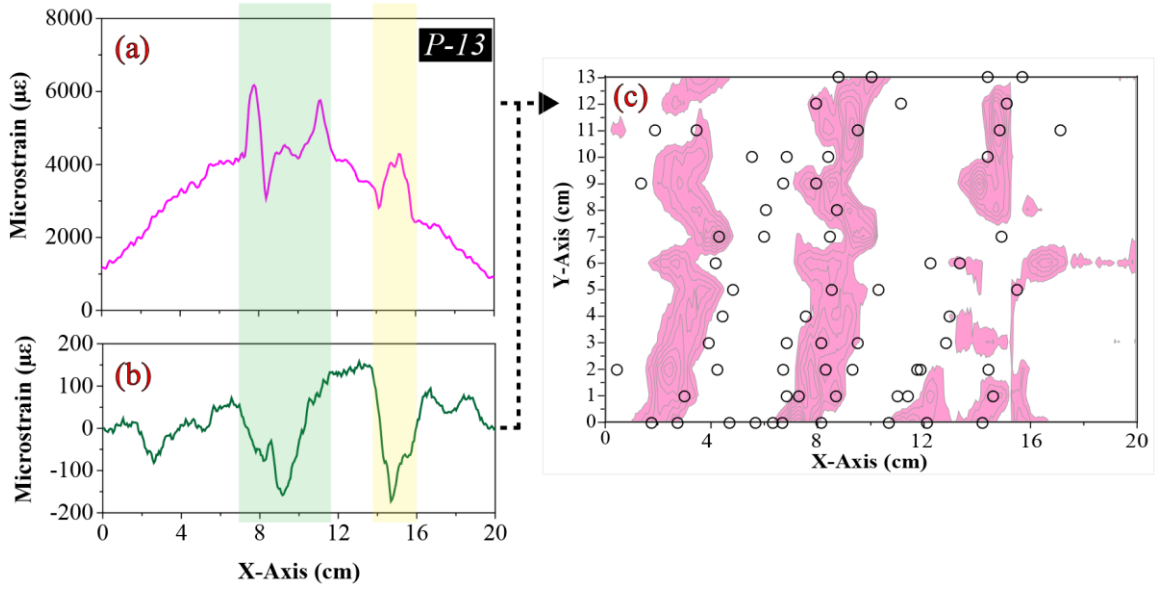


Figure 59. Sensor signals in path 13 are highlighted in (a) the defected area after deformation, and (b) the corresponding curing strain. (c) 2-D plots indicating high-risk areas for damage formation.

## 3.4. (Task 5) Integration of The Multifunction with the Pipeline Integrity Management System

### 3.4.1. (Task 5.1) Development of CIPP Liner Risk Index for The Pipeline Integrity Management Enhanced by AI Algorithms

*3.4.1.1. Displacement-based Bonding Risk Assessment:*

In this task, we create bonding risk map at the corrosion hole area in the pipe-liner system by training the displacement and stress dataset generated from finite element analysis in Task 3.4. Five machine learning algorithms are applied to train (80%) and test (20%) the dataset: 1) Random forest; 2) XGBoost; 3) LightGBM; 4) Support vector machine; and 5) Gaussian process regression. Table 3 shows the accuracy of the five algorithms through the analysis of $R^2$, mean square error, and mean absolute error.

Table 3 Prediction effect of different algorithms

| **Algorithms** | **Prediction types** | $R^2$ | $MSE$ | $MAE$ |
|---|---|---|---|---|
| Random Forest | Stress | 0.826 | 16.035 | 1.877 |
| | Displacement | 0.880 | 4.903 | 0.879 |
| XGBoost | Stress | 0.970 | 2.789 | 0.743 |
| | Displacement | 0.985 | 0.600 | 0.402 |

| | | | | |
|---|---|---|---|---|
| LightGBM | Stress | 0.710 | 26.802 | 2.991 |
| | Displacement | 0.692 | 14.665 | 2.090 |
| Support Vector Machine | Stress | 0.569 | 28.599 | 2.582 |
| | Displacement | 0.643 | 14.624 | 1.674 |
| Gaussian Process | Stress | 0.986 | 1.271 | 0.480 |
| | Displacement | 0.991 | 0.359 | 0.172 |

Figure 60(a) shows the effect of various parameters such as adhesive layer thickness, hole size, and internal pressure on stress and displacement. Internal pressure has greater impact on the stress and displacement at the corrosion hole area that other factors. As shown in Figure 60(b), random forest algorithm provides an accurate prediction on the displacement through the training of the finite element analysis dataset. Figure 60(c) and (d) demonstrate the risk map predicted by machine learning algorithms using the displacement and stress data on the bonding surface between pipe and adhesive layer. For the displacement risk map, we normalize displacement data to 0 (green) to 1 (red) to represent low risk and high bonding risk in the damaged area. For the stress risk map, we define a high-risk criteria by choosing the adhesion strength between epoxy and cast iron as 8.32 MPa [15]. According to Figure 60(d), green area indicates the safe area where bonding stress is below 8.32 MPa, yellow area indicates the critical area where the bonding stress reaches 8.32 MPa, while red area indicates the high-risk area where the bonding stress is greater than 8.32MPa.

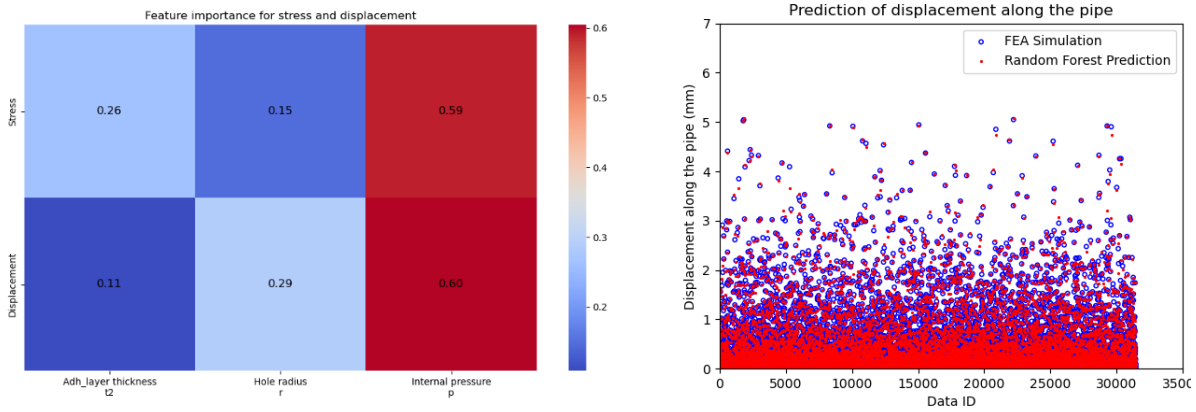


(a) (b)

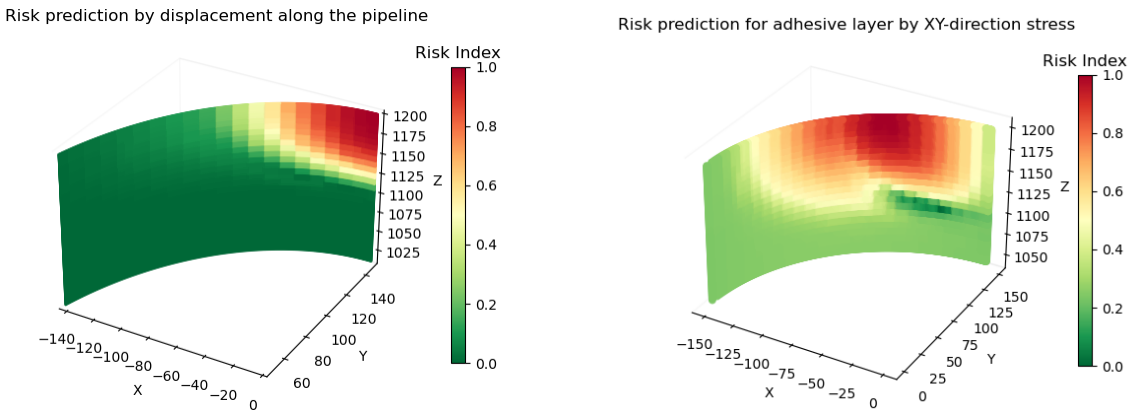


(c) (d)

Figure 60. (a) sensitivity analysis of factors; (b) comparison between machine learning prediction data and FEA data; (c) risk map at corrosion hole area using relative displacement data on the bonding surface between pipe and adhesive layer; (d) risk map at corrosion hole area using stress data on the bonding surface between pipe and adhesive layer.

*3.4.1.2. Stress-based Bonding Risk and Material Failure Risk Assessment*

In this section, our objective is to predict the risk level for the CIPP liner in a damaged pipe using stress information. We consider two potential risks for a pipe-line system: debonding risk and material failure risk. For the debonding risk, we compare the shear stress with the adhesion strength. For material failure, we compare the maximum principal stress with the tensile strength. The basic idea to measure the risk level is to compare the predicted stress with the corresponding strength and normalize their differences into 0 and 1.

We train machine learning-based risk model with the FEA data using the material properties from experiment. Random forest algorithms are used for stress prediction. Table 3 summarizes the results from FEA and ML, it indicates that the potential risks are debonding and failure of the adhesive layer.

Table 4 Comparison between stress and material strength

| **Potential risks** | **Maximum stress (MPa)** | | **Strength (MPa)** |
|---|---|---|---|
| | **FEA simulation (MPa)** | **ML prediction (MPa)** | |
| Debonding | 17.24 | 17.10 | 8.32 |
| Failure of the adhesive layer | 49.91 | 49.62 | 34.15 |
| Failure of the liner | 25.16 | 25.78 | 99.68 |

Figures 61(a) and (b) demonstrate the risk map predicted by machine learning algorithms using the stress data on the bonding surface and adhesive layer material. For the stress risk map, we define the risk criteria by choosing the adhesion strength between epoxy and cast iron as 8.32 MPa [15]. According to the bonding risk map in Figure 61(a), green area indicates the safe area where the bonding stress is below 8.32 MPa, the yellow area indicates the critical area where the bonding stress reaches 8.32 MPa, and the red area indicates the high-risk area where the bonding stress is greater than 8.32 MPa. The corrosion hole is at the upper right corner of the liner, while the risk area is at the edge of the hole based on the stress distribution information. Figure 61(b) shows the material failure risk map. The yellow color represents 34.15 MPa which is the threshold for defining the risk of the adhesive layer material. Highest risk area occurs at the upper right of the adhesive layer, which aligns with the location of the corrosion hole.

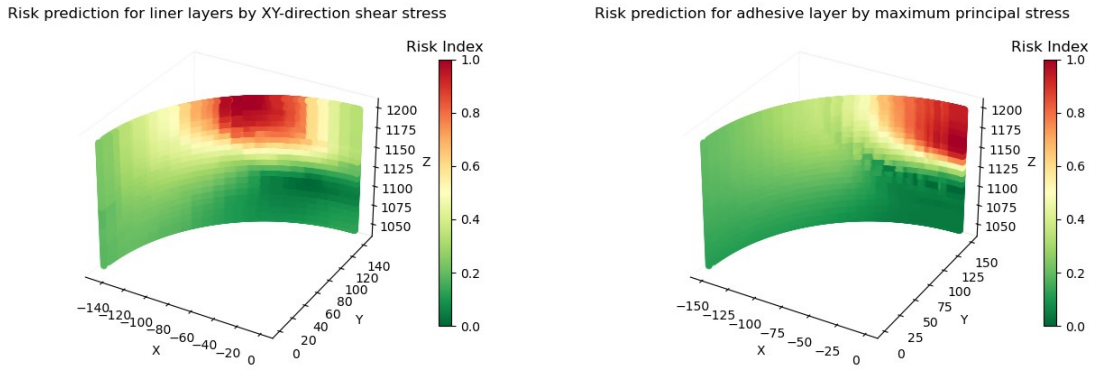


(a) (b)

Figure 61. (a) Debonding risk prediction; (b) Material failure risk prediction for the adhesive layer.

## 4. Future work

In Year 3, according to the planned schedule as shown in Table 5, the major future work as aligned includes:

For Self-Healing Polymer (Task 2):

> The research team will continue evaluating the performance of the selected self-healing polymer, while also working to further develop the formulation to reduce the temperature required for healing. Afterward, the study will focus on incorporating nanoparticle reinforcement to enhance the polymer's properties.

For Nanocomposite Development (Tasks 3.1 and 3.2):

> Nanoparticle development will be closely integrated with the self-healing polymer work, focusing on both short-term and long-term performance. The selection of nanoparticles may be adjusted to align with the capabilities of the next generation of self-healing polymers.

For Molecular Dynamic Simulation (Task 3.3):

Molecular dynamic simulations will continue to develop models for the self-healing polymer to simulate its performance under various environmental conditions. Additionally, gas and water diffusion models will be incorporated into the self-healing polymer model to explore their interactions.

For Finite Element Analysis (Task 3.4):

The FEA study will follow three directions: 1) Generate stress, strain, and failure-related data for liners in pipelines to contribute to Task 5.1. 2) Simulate nanoparticle reinforcement at the micro-scale to evaluate its effectiveness. 3) Collaborate with Task 4 to validate the strain signals collected from the smart liner system.

For Smart CIPP Liner with Distributed Fiber Optic Sensors (Task 4):

The team will continue to integrate and evaluate distributed fiber optic sensors within the CIPP liner system to improve real-time monitoring capabilities and performance assessment.

For AI-Driven Risk Analysis (Task 5.1):

By gathering data from experiments and FEA simulations, the machine learning model will iteratively improve, leading to increasingly accurate predictions for the entire pipeline or even broader pipeline systems.

Table 5 Project schedule for Yr 3

| Tasks (Milestones, Completion Date) | Year 1 | | | | Year 2 | | | | Year 3 | | | |
|---|---|---|---|---|---|---|---|---|---|---|---|---|
| | Q1 | Q2 | Q3 | Q4 | Q1 | Q2 | Q3 | Q4 | Q1 | Q2 | Q3 | Q4 |
| Task 1 (Milestone 1) (M.1: 01/10/2023) | X | | | | | | | | | | | |
| Task 2 (Milestone 2) (M.2: 10/10/2024) | X | X | X | X | X | X | X | X | | | | |
| Task 3 (Milestone 3) (M.3: 01/10/2025) | X | X | X | X | X | X | X | X | v | v | | |
| Task 4 (Milestone 4) (M.4: 04/10/2025) | | X | X | X | X | X | X | X | v | v | v | |
| Task 5 (Milestone 5) (M.5: 07/10/2025) | | | X | X | X | X | X | X | v | v | v | v |
| Task 6 (Milestone 6) (M.6: 09/30/2025) | X | X | X | X | X | X | X | X | v | v | v | v |

# References


[1] Lu H, Wu X, Ni H, Azimi M, Yan X, Niu Y. Stress analysis of urban gas pipeline repaired by inserted hose lining method. Composites Part B: Engineering 2020;183:107657.

[2] Hobbiebrunken T, Fiedler B, Hojo M, Tanaka M. Experimental determination of the true epoxy resin strength using micro-scaled specimens. Composites Part A: Applied Science and Manufacturing 2007;38:814–8.

[3] Liu GR, Nguyen-Thoi T, Lam K. A novel alpha finite element method (αFEM) for exact solution to mechanics problems using triangular and tetrahedral elements. Computer Methods in Applied Mechanics and Engineering 2008;197:3883–97.

[4] Cui Y, Chen Z. Void initiation from interfacial debonding of spherical silicon particles inside a silicon-copper nanocomposite: a molecular dynamics study. Modelling and Simulation in Materials Science and Engineering 2016;25:025007.

[5] Fu G, Shannon B, Deo R, Azoor R, Kodikara J. An equation for hole-spanning design of underground cast iron pipes lined with polymeric liners. Tunnelling and Underground Space Technology 2022;123:104435.

[6] Sarkar S, Singh IV, Mishra BK, Shedbale AS, Poh LH. Source codes and simulation data for the finite element implementation of the conventional and localizing gradient damage methods in ABAQUS. Data in Brief 2019;26:104533.

[7] Yun Z, Xu K, Yang F, Tang X. Structure design and mechanical performance test of a direct ventricular assist device pneumatic flexible actuator. The International Journal of Artificial Organs 2022;45:35–43.

[8] Hajlaoui A, Jarraya A, El Bikri K, Dammak F. Buckling analysis of functionally graded materials structures with enhanced solid-shell elements and transverse shear correction. Composite Structures 2015;132:87–97.

[9] Kolanu NR, Raju G, Ramji M. Experimental and numerical studies on the buckling and post-buckling behavior of single blade-stiffened CFRP panels. Composite Structures 2018;196:135–54.

[10] Systemes D. ABAQUS/CAE User's Manual, Version 6.14. Providence, RI: Dassault Systemes Simulia Corp 2014.

[11] Venkateswara Rao G, Anandrao KS, Gupta RK. Thermal post-buckling of slender composite and FGM columns through a simple and novel FE formulation. Sādhanā 2016;41:869–75.

[12] Nadeem M, Chakraborty T, Matsagar V. Nonlinear buckling analysis of slender piles with geometric imperfections. Journal of Geotechnical and Geoenvironmental Engineering 2015;141:06014014.

[13] Taylor M, Davidovitch B, Qiu Z, Bertoldi K. A comparative analysis of numerical approaches to the mechanics of elastic sheets. Journal of the Mechanics and Physics of Solids 2015;79:92–107.

[14] Hussein A, Ramasundaram S, Kim B. A novel method for fabricating bioinspired layered nanocomposites using aligned graphene oxide/PVDF and their micromechanical modeling. Materials Today Communications 2020;24:101050. https://doi.org/10.1016/j.mtcomm.2020.101050.

[15] Samardžija M, Kurtela M, Vuković Domanovac M, Alar V. Anticorrosion and Antibacterial Properties of Al NP–Epoxy Nanocomposite Coating on Grey Cast Iron. Coatings 2023;13:898.